PROCESS MEASUREMENTS AND KINETICS OF UNSEEDED BATCH COOLING CRYSTALLIZATION

A Thesis
Presented to
The Academic Faculty

by

Huayu Li

In Partial Fulfillment
of the Requirements for the Degree
Doctor of Philosophy in the
School of Chemical and Biomolecular Engineering

Georgia Institute of Technology
May 2015

PROCESS MEASUREMENTS AND KINETICS OF UNSEEDED BATCH COOLING CRYSTALLIZATION

Approved by:

Dr. Ronald W. Rousseau, Advisor
School of Chemical and Biomolecular
Engineering
Georgia Institute of Technology

Dr. Yoshiaki Kawajiri, co-Advisor
School of Chemical and Biomolecular
Engineering
Georgia Institute of Technology

Dr. Martha A. Grover, co-Advisor
School of Chemical and Biomolecular
Engineering
Georgia Institute of Technology

Dr. Athanasios Nenes
School of Chemical and Biomolecular
Engineering
Georgia Institute of Technology

Dr. Facundo M. Fernandez
School of Chemistry and Biochemistry
Georgia Institute of Technology

Date Approved: Jan 20, 2015

ACKNOWLEDGEMENTS

TABLE OF CONTENTS

LIST OF TABLES

LIST OF FIGURES

SUMMARY

This thesis describes the development of an empirical model of focus beam reflectance measurements (FBRM) and the application of the model to monitoring batch cooling crystallization and extracting information on crystallization kinetics.

Batch crystallization is widely used in the fine chemical and pharmaceutical industries to purify and separate solid products. The crystal size distribution (CSD) of the final product greatly influences the product characteristics, such as purity, stability, and bioavailability. It also has a great effect on downstream processing. To achieve a desired CSD of the final product, batch crystallization processes need to be monitored, understood, and controlled.

FBRM is a promising technique for *in situ* determination of the CSD. It is based on scattering of laser light and provides a chord-length distribution (CLD), which is a complex function of crystal geometry. In this thesis, an empirical correlation between CSDs and CLDs is established and applied in place of existing first-principles FBRM models. Built from experimental data, the empirical mapping of CSD and CLD is advantageous in representing some effects that are difficult to quantify by mathematical and physical expressions. The developed model enables computation of the CSD from measured CLDs, which can be followed during the evolution of the crystal population during batch cooling crystallization processes.

Paracetamol, a common drug product also known as acetaminophen, is selected as the model compound in this thesis study. The empirical model was first established and verified in a paracetamol-nonsolvent (toluene) slurry, and later applied to the paracetamol-ethanol crystallization system. Complementary to the FBRM measurements, solute concentrations in the liquid phase were determined by *in situ* infrared

spectra, and they were jointly implemented to monitor the crystallization process.

The framework of measuring the CSD and the solute concentration allows the estimation of crystallization kinetics, including those for primary nucleation, secondary nucleation, and crystal growth. These parameters were determined simultaneously by fitting the full population balance model to process measurements obtained from multiple unseeded paracetamol-ethanol crystallization runs.

The major contributions of this thesis study are (1) providing a novel methodology for using FBRM measurements to estimate CSD; (2) development of an experimental protocol that provided data sets rich in information on crystal growth and primary and secondary nucleation; (3) interpretation of kinetics so that appropriate model parameters could be extracted from fitting population balances to experimental data; (4) identification of the potential importance of secondary nucleation relative to primary nucleation. The protocol and methods developed in this study can be applied to other systems for evaluating and improving batch crystallization processes.

CHAPTER I

INTRODUCTION

Crystallization from solution is a common technique which utilizes the phase separation induced by cooling, antisolvent addition, or evaporation. From lab scale recrystallization to massive production of valuable molecules in the solid state, this technique participates in almost all the processes related with chemical development and manufacturing. The crystallization processes determine the quality of the product. For example, the crystal forms of active pharmaceutical ingredients (APIs) and their particle size distributions are vital properties in the pharmaceutical industry for the achievement of high purity, efficacy, and stability of drug products.

Batch crystallization is often used in fine chemicals and pharmaceutical industries, since only a small quantity of the valuable compound is available at one time. Batch operation is very flexible and multiple methods of crystallization, such as cooling and antisolvent addition, can be jointly used to maximize the yield. Obtaining a proper crystal size distribution (CSD) is another objective, because it not only relates with the purity and bioavailability of the drug, but also determines the ease of downstream processing. The batch process move through transient states, so a good design of the operation policy is required to achieve the desired yield and CSD.

To obtain better knowledge of batch processes, *in situ* equipment has been developed to track the evolution of the crystallization process in both liquid and solid phases. These techniques employ certain optical or spectroscopic properties of the system, so that sample removal from the system is not required. However, the disadvantage of *in situ* measurements is the implicit transformation between the variables being measured and the measurements. For example, realtime IR spectra do relate to

solute concentrations, but they are functions of both solute concentration and temperature. Although a qualitative trend can be seen from the spectra, quantifying the solute concentration is more difficult than with HPLC analysis.

A challenging problem among the online techniques for crystallization systems is to measure the CSD, which is often performed by off-line laser diffraction or sieve analysis. The procedures of off-line techniques are laborious and time-consuming, and online decisions cannot be made promptly based on the offline results.

FBRM is a promising method for CSD estimation, which employs a rapidly rotating laser to scan particles and detects the intensity of the reflected laser. This method measures the time of receiving the reflected laser from the surface of the crystals, and calculates the lengths of paths (called chords) crossing the crystal surface. FBRM can detect numerous chords within each interval. These chords are organized as a histogram, called chord length distribution (CLD) histogram, which is determined by the CSD.

The goal of this study is to investigate the relationship between CLDs and CSDs and use the relationship to establish a framework that can measure the crystallization process. With the process measurements, crystallization kinetics can be analyzed and estimated by population balance modeling. Paracetamol in an ethanolic solution is chosen as the model system, where polymorphic transformation and agglomeration are insignificant. Our aim is to use the framework to observe nucleation and growth of paracetamol crystals. The current situation, techniques, and obstacles related with our topic are reviewed in Chapter 2.

The first step in this thesis is to establish an empirical linear model of the FBRM, hypothesising that crystals from certain size ranges have their characteristic CLDs. This idea and the empirical model are explained and tested in a nonsolvent (toluene), as discussed in Chapter 3. A numerical algorithm that estimates CSDs from CLDs is described in this chapter as well.

The feasibility of the empirical model is demonstrated in a real unseeded batch cooling crystallization of paracetamol-ethanol in Chapter 4. The model obtained from Chapter 3 is adopted and combined with concentration measurement from ATR-FTIR, providing the number density of the crystal population and solute concentration at the same time. A two-stage cooling process has been tested with the *in situ* measuring framework. Advantages of the empirical model are shown by comparison between the estimated CSDs and CLDs.

With the measurement techniques, a series of unseeded experiments can be performed with controlled supersaturation at the onset of nucleation. The CSDs measured by sieving and FBRM, and the supersaturation profiles measured by ATR-FTIR are fitted by the solution of a population balance equation (PBE). Three crystallization phenomena – primary nucleation, secondary nucleation, and crystal growth – are simulated to interpret the experimental results. This work is presented in Chapter 5.

Chapter 6 summarizes the main findings in the previous chapters and concludes the thesis. Recommendation for future studies are discussed for further development of the FBRM model and evaluation of kinetic parameters.

CHAPTER II

BACKGROUND

2.1 Crystallization fundamentals

2.1.1 Thermodynamics of crystallization

Crystals are the solid substances that has a periodical arrangement of atoms or molecules, and such arrangement can be achieved by crystallization in amorphous solid, liquid, or gaseous state. A necessary condition for crystallization is supersaturation, which is the state that one component of a mixture exceeds its thermodynamic equilibrium. Such equilibrium for a liquid solution system is often called solubility.

Solubility is determined by quantifying the amount of solute in an equilibrated solution. To measure the solubility, excessive amount of solute is added to the solvent, left in a water bath or oven, and maintained at a fixed temperature. The container is sealed and kept in agitation to enhance mass transfer between the solid and the solution. Equilibrium can often be achieved in a few days, and then the liquid phase is sampled. The solute concentration, or solubility at this particular temperature, is measured by some chemical analysis methods, such as high performance liquid chromatography (HPLC), thermal gravimetric analysis (TGA), etc.

When the concentration of a compound is higher than its solubility, the solute molecules tend to crystallize out from the supersaturated solution. Supersaturation can be achieved by multiple ways, such as cooling, evaporation of solvent, addition of antisolvent, and changing pH. Supersaturation is essentially the driving force of crystallization, determining the crystal form and the rate of crystallization.

Crystal forms, or the spatial arrangements of molecules, may vary under different supersaturation and solvent compositions. Solvent molecules may also participate
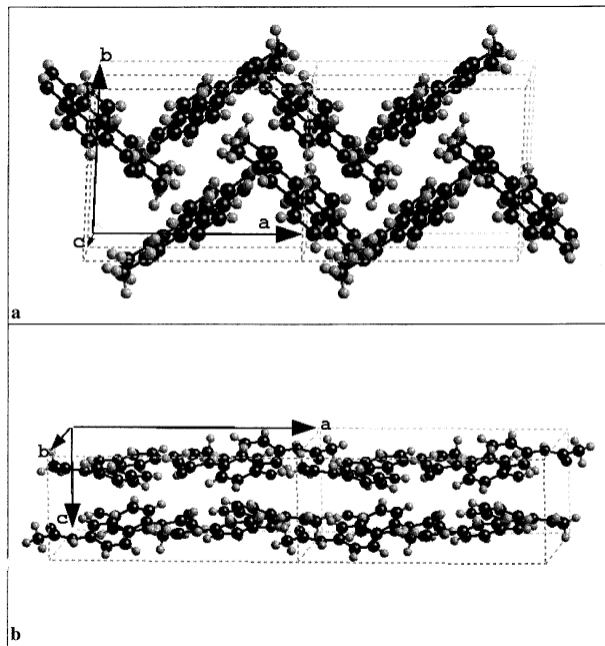
Figure 2.1: Crystal structures of paracetamol: (a) Form I (b) Form II. Reprinted with permission from [8]. Copyright 2001 American Chemistry Society.

in crystallization to form hydrates and solvates. For example, paracetamol, an API in Tylenol, has three known crystal forms [17]. Form I (monoclinic) is the thermodynamically stable form, which can be obtained at room temperature. Form II (orthorhombic) is metastable at ambient condition. Form III has the most unstable structure and it can be only obtained from melt crystallization. As shown in Figure 2.1, molecules in Form I are arranged in pleated sheets, whereas Form II has a layer-by-layer stacking structure. As a result, their mechanical properties are different: Form I is stiff and requires binders when compressed, while Form II deforms relatively easily. The crystal structure of Form III has not been reported yet.

In fact, solubility changes with crystal forms and it reflects the stability of the crystal structure [97]. The most stable form usually has the lowest solubility. According to the Ostwald's step rule, the metastable form may nucleate first, and later transform to the stable form. As illustrated in Figure 2.2, the solubility of the
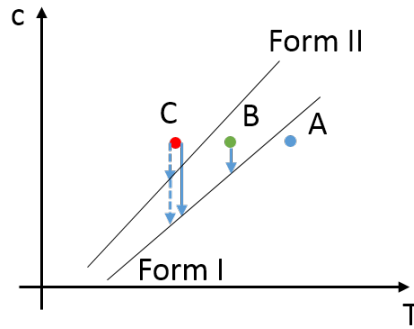
Figure 2.2: Solubility curves for two crystal forms. Form I is the stable form and Form II is the metastable form

metastable Form II is larger than the solubility of the stable Form I. Suppose a solution at a undersaturated state A is cooled to supersaturated state B. Nucleation of Form I can occur. If the cooling is rapid and the solution reaches state C, there are two possible kinetic events that can happen. One is the thermodynamically favored nucleation of Form I, and the other one is the kinetically favored nucleation of Form II. Depending on the nucleation rates of the two forms, they can happen simultaneously. If the metastable Form II crystallizes out first, there is a tendency of polymorphic transformation from Form II to the stable Form I. If the solution has a concentration at any point below the solubility line of Form II, the crystals of Form II can dissolve. Crystals in Form I will keep crystallizing. Eventually, all the crystals should be in Form I, if the solution is given enough time to reach equilibrium.

2.1.2 Kinetics of crystallization

In a clear unseeded supersaturated solution, nucleation is always the first kinetic event to occur, followed by crystal growth. Nucleation is the formation of a tiny crystal in a particular structure. Growth is the expansion of the crystal volume from the deposition of solute molecules to the crystal surface. Nucleation can occur without any other crystalline matter, or take place in the vicinity of crystals [97]. The former one is called primary nucleation, which can be divided to homogeneous and heterogeneous

mechanisms. The latter one is called secondary nucleation, which is attributable to the influence of the detachment of nuclei from the surface of pre-existing crystals.

For primary nucleation, classical nucleation theory (CNT) considered the Gibbs

Nucleation

Primary   Secondary
                 (induced by crystals)

Homogeneous   Heterogeneous
(spontaneous)   (induced by foreign particles)
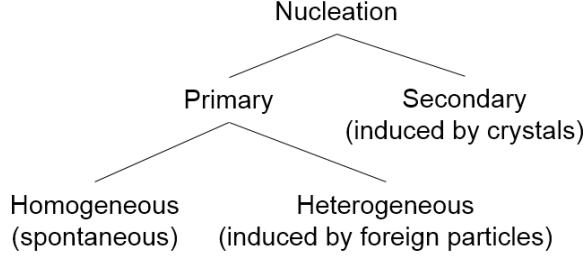
Figure 2.3: Categories of nucleation

free energy balance between the bulk and the surface of a crystal to model homogeneous nucleation, assuming the formation of the nuclei is similar to the formation of a water droplet by condensation of water vapor [28, 135, 6]. Suppose in a supersaturated solution, a round particle with radius r is formed, which results in the change of overall free energy ΔG. On one hand, the free energy change of the crystallization is proportional to the volume of the particle $4\pi r^3/3$. On the other hand, the nucleation process needs to overcome the interfacial tension because of the newly-created solid-liquid surface $4\pi r^2$. In total,

$$\Delta G = \frac{4}{3}\pi r^3 \Delta G_v + 4\pi r^2 \sigma \tag{2.1}$$

in which ΔG_v is the volumetric free energy change [J/m^3] and σ is the interfacial tension [J/m^2]. In Equation (2.1), the first term is negative, decreasing with r^3, and the second term is positive, increasing with r^2. The different signs of the two terms indicate that there exists a maximum of ΔG, as shown in Figure 2.4.

The critical radius that leads to the highest free energy change can be obtained by taking the derivative of r in Equation (2.1).

$$r_c = -2\sigma/\Delta G_v \tag{2.2}$$
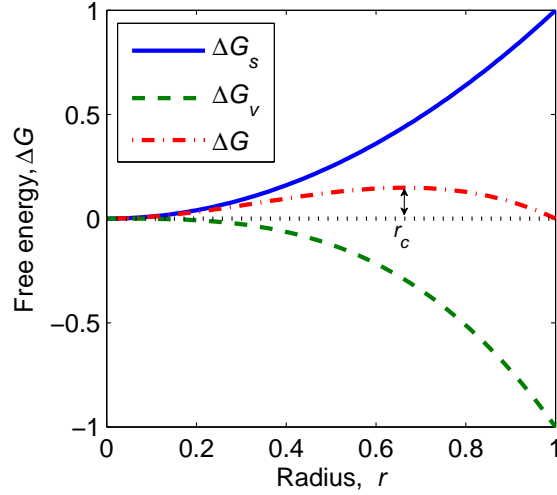
Figure 2.4: Total free energy change from solid crystal (ΔG_v) and from interface ($\Delta G_s = 4\pi r^2 \sigma$)

and the maximum of ΔG is

$$\Delta G_{crit} = \frac{16\pi\sigma^3}{3(\Delta G_v)^2} \tag{2.3}$$

If the radius of a newly created crystal is less than r_c, it tends to dissolve because the total free energy decreases if r becomes smaller. If the radius is greater than r_c, it can grow. Therefore, the physical meaning of r_c is the smallest size of nucleus that is stable in the solution and capable of growing. Using ΔG_{crit} as the activation energy of nucleation, the primary nucleation rate can be written in the Arrhenius form.

$$B_1 = k_{b1} \exp(-\Delta G_{crit}/kT) \tag{2.4}$$

in which k_{b1} is the primary nucleation constant, k is the Boltzmann constant, and T is the absolute temperature of the system. The critical free energy change can be written as [97]

$$\Delta G_{crit} = \frac{kT \ln S}{\nu} \tag{2.5}$$

in which $S = c/c_s$ is the supersaturation ratio (concentration over solubility) and ν is the volume of the solute molecule. Combining Equations (2.3), (2.4), and (2.5), one
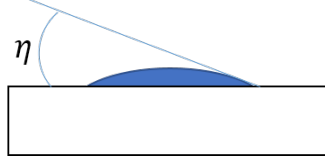
Figure 2.5: Reduction of ΔG_{crit} by nucleation on a foreign surface

can obtain the homogeneous nucleation rate

$$B_{1,hom} = k_{b1} \exp\left[-\frac{16\pi\sigma^3\nu^2}{3k^3T^3(\ln S)^2}\right] \tag{2.6}$$

Besides Equation (2.6), the primary nucleation rate can be also written empirically [98]

$$B_1 = k_{b1}(S-1)^b \tag{2.7}$$

where S is the supersaturation ratio, defined as $S = c/c_s$. If there are some foreign particles, nuclei can form on the surface of the particles, as shown in Figure 2.5, and ΔG_{crit} is lowered, because the shape of nuclei does not have to be a full sphere. The heterogeneous nucleation rate is written as [97]

$$B_{1,het} = k_{b1,het} \exp\left[-\frac{16\pi\sigma^3\nu^2}{3k^3T^3(\ln S)^2}\right] \tag{2.8}$$

We can see that only a different nucleation coefficient is used to explain the decrease of critical free energy. It is found that some engineered surface features can control the morphology of crystals and accelerate nucleation [18, 39, 109].

In the secondary nucleation mechanism, creation of nuclei depends on the pre-existing crystals. The mechanism is often referred as contact nucleation [97, 117]. Nuclei can be stripped off due to the mechanical forces applied on the crystalline surface, including fluid shear, collision with other crystals and crystallizer internals. Unlike those primary nuclei discussed above, the secondary nuclei have no ΔG_{crit} to overcome, and thus are more common in most industrial applications [119]. Due to its complex origins, an empirical model is often used:

$$B_2 = k_{b2}(S-1)^\alpha m_s^\beta \tag{2.9}$$

9

in which k_{b2} is the coefficient for secondary nucleation, m_s is the mass of crystals in the crystallizer, and α and β are the exponents for $(S-1)$ and m_s.

As shown in Equation (2.9), the secondary nucleation rate is related to supersaturation and the mass of crystals. High supersaturation often leads to a rapid growth rate, which makes the crystal surface rougher and more nuclei can detach. The mass of crystals is proportional to the momentum of solid, which is related to the force applied to the crystals. Other factors relating to mixing, such as power of mixing and types of stirrer, can be incorporated into k_{b2}, if they are unchanged.

Once the nuclei have formed, they start to grow. The growth of crystals involves two steps: (i) the transport of solute molecules from bulk phase to the vicinity of crystal surface; (ii) the integration of the solute molecules into the crystal lattice. Solvent molecules also need to diffuse away from the crystal surface. A simple empirical form for the growth rate can be written as

$$G = k_g(S-1)^\sigma \tag{2.10}$$

in which k_g is the growth constant [97, 117]. $S-1$ is sometimes replaced by $\Delta c = c - c_s$. If temperature effect is considered

$$G = k_g \exp(-E_a/RT)(S-1)^\sigma \tag{2.11}$$

in which an activation energy E_a is used to describe the temperature dependence [140, 22]. If the growth rate is size-dependent, the following equation is often used

$$G = k_g \exp(-E_a/RT)(S-1)^\sigma(1+aL)^\eta \tag{2.12}$$

in which q and η are used to explain the observation that large crystals grow faster in some cases [2, 11].

Agglomeration and breakage might also occur during crystallization, but generally less often than nucleation and growth. In some particular systems, when two crystals contact at a certain angle, a bond is formed to connect the surfaces of the crystals [126,

150]. The net effect of agglomeration is the increase of the number of large crystals at the expense of small crystals. Breakage usually occurs with needle-shaped crystals, or when some external energy is applied to solutions, such as ultrasound [37] and milling [134].

2.2 Simulation of crystallization

2.2.1 Population balance equations

The governing equation of crystallization should address the changes in both liquid and solid phases. In a well-mixed crystallizer, the liquid and the solid phases are uniform throughout the suspension. However, crystals dispersed in the solution have their individual features, such as sizes and morphologies. To distinguish such features, a population balance model is used [117].

$$\frac{\partial n}{\partial t} + \nabla \cdot (\mathbf{v_i}n) - B + D = 0 \tag{2.13}$$

in which $\mathbf{v_i}$ is called internal coordinates, n is the number density or number of crystals in the space of $\mathbf{v_i}$, B is the birth rate of crystals and D is the death rate of crystals. The internal coordinates $\mathbf{v_i}$ may have multiple dimensions, and some of them are continuous while others are discrete. For example, size of crystals is a continuous variable (subscript "c") and the morphology is discrete (subscript "d"). As a result,

$$n = n(\mathbf{v_{i,c}}, \mathbf{v_{i,d}}) \tag{2.14}$$

The integral of n over the entire space $(\mathbf{v_{i,c}}, \mathbf{v_{i,d}})$ should give the total number of crystals.

For a lab-scale batch cooling crystallizer, Equation (2.13) is usually simplified. If only one crystal form nucleates and the aspect ratio of the crystals is constant, only one internal coordinate is required, which is the size. If agglomeration and breakage can also be neglected, so birth of critical nuclei is the only factor that needs to be

considered. The population balance equation (PBE) is simplified to

$$\frac{\partial n}{\partial t} + G\frac{\partial(n)}{\partial L} = 0 \tag{2.15}$$

in which G is the size-independent growth rate and L is the size of crystals. The boundary condition is

$$n(t, L = 0) = \frac{B}{G} \tag{2.16}$$

2.2.2 Method of Moments

Solving the population balance model is computationally intensive, even for the most simple form of Equation (2.15), because the partial differential equation (PDE) requires both spatial and temporal discretization. The moment transformation of population can reduce the PDE to a system of ordinary differential equations, which is relatively simple to solve numerically. Define μ_i as the ith moments of the CSD by

$$\mu_i = \int_0^\infty nL^i \, dL \tag{2.17}$$

The PBE of Equation (2.15), if the transformation in Equation (2.17) are applied to n, can be written as

$$\frac{d\mu_i}{dt} = 0^i B + iG\mu_{i-1}, i = 0, 1, 2, ... \tag{2.18}$$

Comparing Equation (2.18) with Equation (2.15), it can be seen that the variable n ranging from 0 to ∞ turns into a set of equations with an infinite numbers of moments. The CSD is often assumed to be a normal, log-normal, or β function, so only a few moments are needed for the reconstruction of the CSD [19, 52, 114].

The mass balance of the batch crystallizer gives the concentration of solute

$$c = c_0 + m_{s,0} - k_v\rho_s\mu_3 \tag{2.19}$$

in which c_0 is the initial concentration, $m_{s,0}$ is the mass of seeds at the beginning of the batch, k_v is the volume factor for the crystals, ρ_s is the density of the crystals. In application, μ_0 to μ_3 are usually used when modeling the crystallization process.

The zeroth moment μ_0 is the total number of crystals, μ_1 is the total length of the CSD (sum of the one dimensional sizes of crystals), μ_2 is proportional to the total surface area of solid phase, and μ_3 is the total volume of crystals, proportional to the mass of crystals. However, applications of this ordinary method of moments (MOM) are limited to certain types of systems, in which the growth rate is size-independent or linearly size-dependent. In other cases, the problem is not closed, i.e. the lower moments are functions of higher moments.

Developed by McGraw [87], quadrature functions are used to approximate the CSD, so that the moments are written as a combination of quadrature functions. The quadrature methods of moments (QMOM) has been used to solve PBEs with size-dependent growth [2], and agglomeration-breakage [86]. It can also be embedded into a computational fluid package to simulate a complicate mixing situation with crystallization [85, 147].

2.2.3 Numerical methods of the full PBE

Many methods have been developed in order to directly solve the PBE and obtain the evolution of the CSD during crystallization. Considering the characteristic lines in the PDE system, methods of characteristic [47, 64, 65, 66] have been successfully applied to solve nucleation and size-dependent growth [2].

Another type of approach is to completely discretize the space-time domain and apply the mathematical relations implied by the governing equations. This type of method is discussed by LeVeque [69], including finite-difference method (FDM), finite-volume method (FVM), and finite-element method (FEM). The key is how to approximate the $\partial(Gn)/\partial L$ term.

Generally, FDM has strong numerical leaks and oscillations around shock waves. Bennett *et al.* [7] combined two FDMs (Lax-Wendroff and Crank-Nicholson) to simulate a continuous crystallizer. Muhr *et al.* [96] found that the simulation results

13

may depend on the spacing of grid points in size domain in the simulation of primary nucleation in a jet mixer, if the spacing is not fine enough. Weighted essential non-oscillatory (WENO) methods, using more neighboring points to evaluate the derivative, can enhance the accuracy near a sharp front. A few modifications of WENO methods were examined by Hermanto *et al.* [43] for seeded processes.

FVM separates the size domain into many cells and assumes a piece-wise constant solution throughout each cell. The number of crystals in each cell is solved, instead of directly solving for the number density as in FDM. Essentially, the mass is conserved so that oscillation is greatly reduced. However, FVM suffers from numerical diffusion, which smooths the steep gradients around shock waves. Developed by Sweby [127], high resolution FVM methods with flux limiter are used to solve PBE with nucleation, growth, agglomeration, and breakage [111, 112, 113]. Good performance of this method was shown by Qamar *et al.* [112], compared with first-order FVM and PARSIVAL (a commercial simulation package, using FEM).

FEM, assuming the CSD function is a linear combination of orthogonal collocation functions, can be an alternative to solve the PBE. The solution variables are replaced by the coefficients of the orthogonal functions. Wulkow *et al.* used Galerkin functions with self-adaptive grid constructions to simulate a crystallization process [142, 143], which led to the commercial package PARSIVAL. However, in a comparative study, Mesbah *et al.* showed that the FEM with Galerkin's technique was less appealing than high resolution FVM and method of characteristics (MOC) in their simulation [89].

Two recent studies [95, 112] introduced another numerical scheme called conservation element/solution element (CE/SE) method, developed by Chang [13]. It used a different approach to discretize the spatial-time domain and implement the conservation law. CE/SE method was shown to be more accurate than FVM and MOC for both batch and continuous crystallization. Details can be found in later chapters.

In summary, the simulation of PBE has been extensively studied, and models from simple ODEs to complicated numerical schemes are available. Crystallization kinetics such as nucleation, growth, agglomeration, and breakage can be simulated with a proper solution method.

2.3   Off-line measurements of crystallization processes

The off-line methods are those techniques that analyze samples taken from the process and undergone some irreversible treatments. In crystallization, the process variables of interest are solute concentration and information of crystals, such crystal forms and size distribution. The solute concentration can be determined by standard analytical chemistry methods, such as HPLC, titration, or TGA. Information about crystals can be measured by the following methods.

Sieve analysis is a simple and common method for the determination of size distribution. The sieve trays are weaved with metal wires, and the alignment of wires allows crystals less than a particular size to penetrate. The sieve trays are assembled vertically in the size-descendent order from top to bottom. The crystals are placed at the top tray and the trays are secured in a shaker. Shaking the trays allows the crystals to penetrate openings and eventually stay in the proper trays. The mass of crystals in each tray can be measured, which gives the mass or volume density of the CSD. Sieve analysis is straightforward, but it requires preprocessing such as washing and drying that may alter the CSD. The sizes of the openings correlate with the second longest dimension of crystals. When the aspect ratio is high, poor penetration through the openings is a disadvantage of sieve analysis.

A method that requires less preprocessing is laser diffraction [50]. When a laser beam passes through a dilute suspension, the diffraction pattern is affected by the particle size distribution of the suspension, as shown in Figure 2.6. According to Fraunhofer and Mie diffraction theories, large particles scatter light at small angles

relative to the laser beam and small particles scatter light at large angles, as illustrated in Figure 2.7. The diffraction pattern is then deconvoluted to estimate the particle size distribution, which is reported as a volume-equivalent sphere diameter.
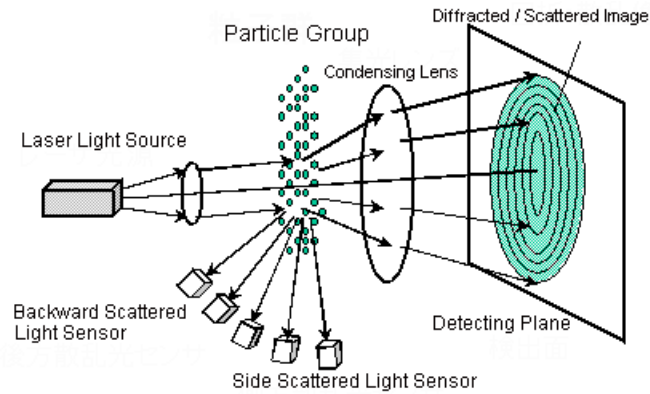
Figure 2.6: Mechanism of laser diffraction, image courtesy of shimadzu.com
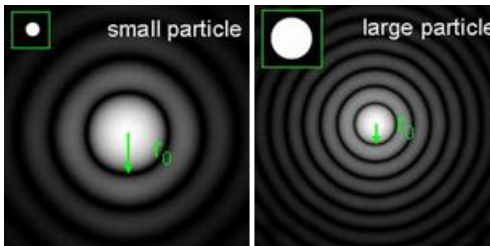
Figure 2.7: Comparison of laser diffraction patterns of large and small particles, image courtesy of sympatec.com

A more straightforward way than laser diffraction is to analyze the microscopic pictures of the crystals. The size in the microscopic images is measured, if the magnification is known. Meanwhile, the aspect ratio and the morphology of the crystals can be determined. However, to obtain accurate statistics of the crystal size, a large number of crystals should be pictured, which makes it a very time-consuming task due to manual determination of the dimension of the crystals.

Crystal form is also a critical quality. Off-line methods, such as X-ray diffraction (XRD) and differential scanning calorimetry (DSC) are usually used to determine the

crystal forms after the samples are properly prepared [36].

2.4   On-line measurements

On-line methods, on the contrary, are those techniques that can analyze the samples automatically and promptly. One type of on-line techniques is *in situ* methods, which take measurements directly inside the crystallizer (Another type is those sampling device that measures properties *ex situ*, such as automatic HPLC). The equipment uses some light rays targeting at certain properties associated with particular wavelengths. The detection ends are usually just probes put in the slurry. Therefore, the *in situ* methods demands no preprocessing and have the minimum interference to the process. Four types of methods are introduced here.

2.4.1   Focused beam reflectance measurements

Focused beam reflectance measurements (FBRM) utilize a focused laser beam cast into the liquid phase and measure the intensity of the laser that is reflected back to the detector. If the liquid is inhomogeneous, i.e. there are some particles or another liquid phase dispersed, the FBRM can collect the reflected laser signal. The configuration of the probe tip is shown in Figure 2.8.

Figure 2.9 shows how the FBRM measures the particles, when a slurry is being measured. The focused beam rotates and swipes many crystals on its circular path. For the examples shown in Figure 2.9, four line segments with high backscattered intensity, corresponding to the paths scanned across the surfaces of four crystals, are detected. These paths are called chords, which are defined as lines connecting two arbitrary edging points. As the focused beam rotates, numerous chords are detected by the FBRM, and the distribution of chords are displayed as a histogram, named the chord-length distribution (CLD) histogram. The chords between 1–1000 μm are measured and divided into 100 logarithmic-spaced bins.
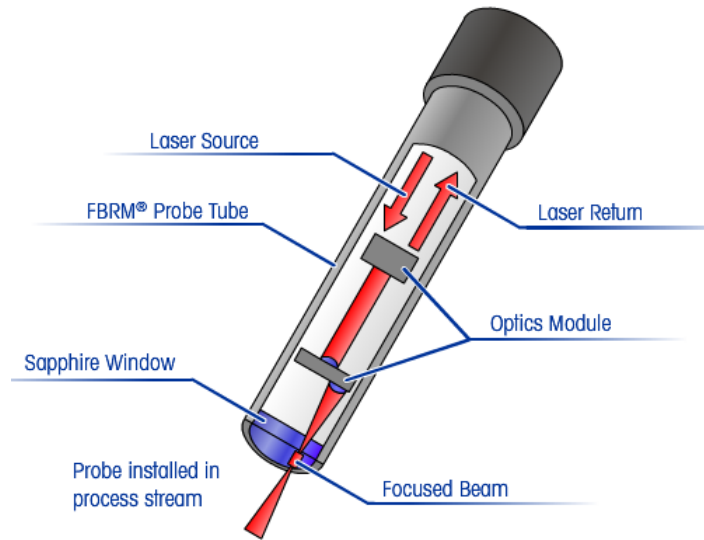
Figure 2.8: The schematic of FBRM, image courtesy of us.mt.com

The relationship between the CLD from FBRM and CSD has been investigated
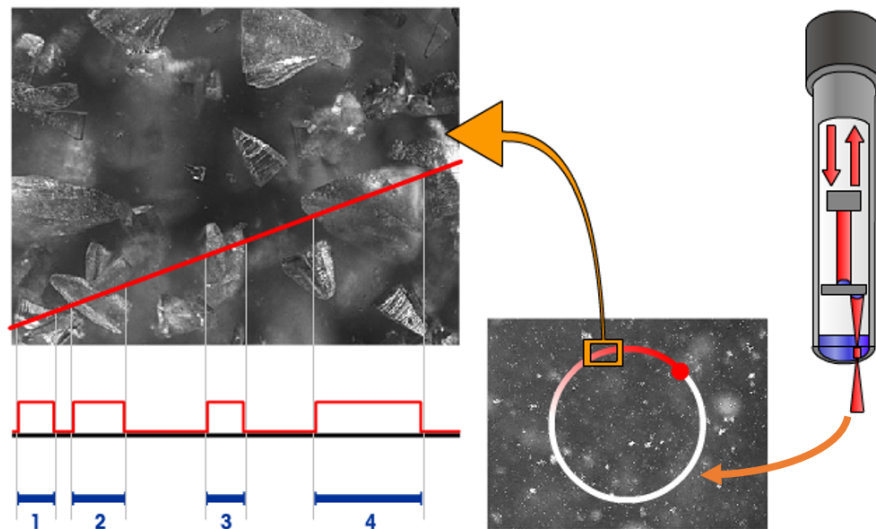
Figure 2.9: Chords measured by the FBRM, image courtesy of us.mt.com

extensively [4, 42, 146], which revealed that more particles lead to more chord counts and large particles have longer mean chord lengths. Such properties provide the FBRM the ability to qualitatively detect the onset of nucleation, crystal growth, and dissolution, and changes in the form of the CLD linked to crystal morphology [5].

Therefore, FBRM was used to study nucleation kinetics [91] and control crystallization [23, 44, 131, 140]. It can also be used to study polymerization [49] and emulsions [68].

To make quantitative estimation of the CSD, researchers have attempted to establish a mathematical model of FBRM that correlates CLD with CSD. The physical phenomena are simplified and first-principles models are built, assuming:

- the particles are spheres with a known diameter

- the laser beam scans the 2D projections of these particles

- the projections are non-overlapping

- chords can be assumed as straight lines cutting though random places on the 2D projections

As we can see, the model includes two steps: the particles are first projected to a 2D space, and then the laser beam is scanned randomly. This type of models, based on the geometric orientations, is called the geometric model. The illustration of this model is shown in Figure 2.10. The line segments in the blue circles are chords.

If the shape of particles is regular, such as a sphere or ellipsoid, the CLD can be
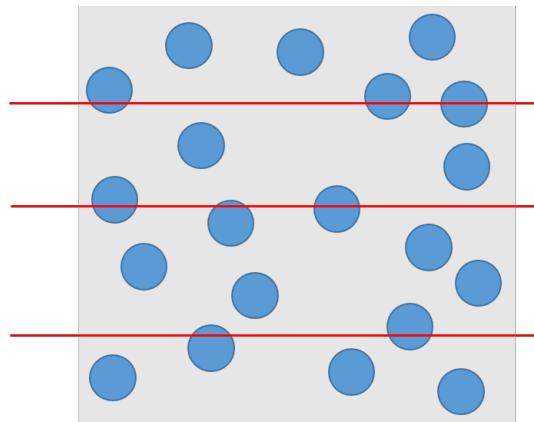
Figure 2.10: Illustration of geometric model: blue circles are the projections of spherical particles and red lines mimic three scans
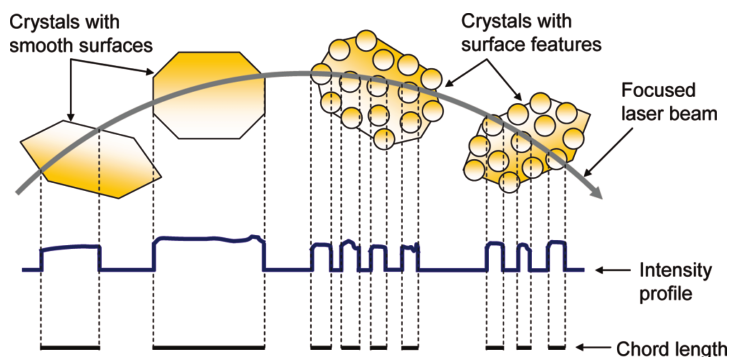
Figure 2.11: Illustration of chord splitting. Reprinted with permission from [3]. Copyright 2010 American Chemistry Society

solved analytically [74, 124, 129, 144]. When the shape is a cube or polyhedron, the 2D projection is difficult to resolve by analytical methods. Therefore, Monte Carlo simulation [102, 120] is used to model the projection of a given shape at random orientations. The possibility of crystals being sampled by the laser beam is assumed proportional to the size of particles. For the geometric model, agreements of CLD data to model predictions have been reported in various suspensions, especially with those of opaque and sphere-like particle systems, such as ceramic beads, aluminium particles, and polymer beads [73, 129, 139].

In a crystallization process, the simple assumptions of the geometric model may be insufficient to estimate the CLD; e.g., the laser may not be backscattered completely because of the transparency of the crystals. Due to the edges and facets of the crystals, the laser scattered from the crystal surface is not as stable as from opaque particles, which is called known as chord splitting [3] (see Figure 2.11). If two particles are close, the light signals can be identified as one chord, known as chord concatenation [55]. In actual measurements, such as the CLD of glycine crystals in ethanol, the peaks of the CLD have no dependence on the size of the crystals and only the skewness of the CLD differs [146], as shown in Figure 2.12. This observation violates the conclusions from the geometric model.

Kail et al. [56, 57] stated such issues for the geometric model and built an op-

20
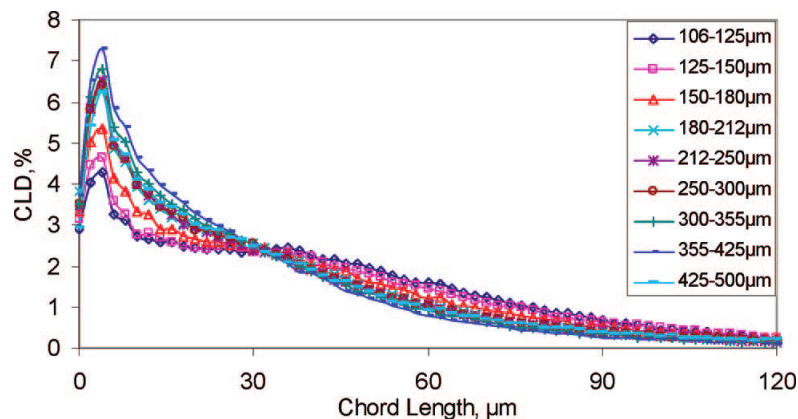
Figure 2.12: The CLDs of glycine crystals at difference sizes. Reprinted with permission from [146]. Copyright 2008 American Chemistry Society

tical model that has many physical subtleties, including laser intensity profile, chord discrimination criteria, refractive indices, particle velocity and so on. Chords are identified if the simulated backscattered laser intensity is greater than a threshold value. These processes are modeled by Monte Carlo simulation, which is much more complicated than that used in the geometric model. The optical model predicts the FBRM measurement much better than the geometric model. It has been applied to estimate the crystal size distribution (CSD), for example, in preferential crystallization [16].

To achieve accurate CSD estimation in crystallization, first-principles models can be very sophisticated. Yet they may still neglect some factors that influence the lengths of chords, for example, the surface roughness of crystals may develop when the crystals are growing. As a result, the backscattering intensity varies as the laser scans across a crystal. Such microscopic features are difficult to model especially when crystal surface is changing due to crystal growth. In batch crystallization, where small crystals grow significantly over time, the CSD estimation can be greatly affected by such phenomenon.

In summary, FBRM is a promising technique that can provide *in situ* information

about crystal size. In order to obtain quantitative size measurements, a model between CLD and CSD must be established. With certain simplifications of the FBRM, a first-principles model was developed, but it is difficult for the first-principles models to characterize and incorporate the surface features of crystals.

2.4.2 ATR-FTIR spectroscopy

Infrared spectra are usually determined *ex situ*, where the infrared ray travels through the sample and the absorbance (or transmittance) is measured. The sample can be liquids, solutions, solids, or thin films. In the determination of solution concentration, the Beer-Lambert law is often used.

$$A = \epsilon l c \tag{2.20}$$

in which l is the path length, c is the solution concentration, and ϵ is an intrinsic constant that relates chemical properties and ambient conditions. Equation (2.20) suggests that the concentration is linearly correlated with absorbance A, which is defined as

$$A = -\ln(I/I_0) \tag{2.21}$$

where I_0 and I is the intensity of the incident radiation and transmitted radiation, respectively. To measure the solute concentration during crystallization processes, practical difficulties are:

- ensure no solids remains in the sample

- select proper length path or dilution ratio in order to obtain effective absorbance

- avoid phase change, such as nucleation, crystal growth, dissolution, and evaporation of solvent

These are common error sources when performing off-line IR spectroscopy. On-line method can use external circulating lines to introduce a solid-free stream to the IR measuring cell. However, it is difficult to ensure the circulation path is solid free, making this on-line method fragile.

Attenuated total reflectance (ATR)-FTIR allows the *in situ* measurement of IR spectra without any preparation of samples. By using an ATR crystal, IR absorption only takes place at the interface of the ATR crystal and the solution. As shown in Figure 2.13 [93], there is a small penetration of the infrared light into the sample at each IR reflection. Absorpance occurs when the wave penetrates into the sample. Multiple total reflections happen on the interface and the IR spectrum of the solution is determined.

The ATR crystal and other optical devices are incorporated into a probe, which
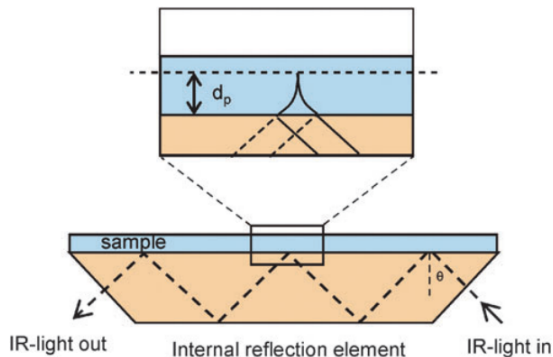
Figure 2.13: The schematic of ATR-FTIR. Reprinted with permission from [93]. Copyright 2010 Royal Society of Chemistry.

is placed in the crystallizer and measures the IR spectra *in situ*. Since the depth of evanescent wave is only a few micrometers, the influence of solids can be neglected if no crystals attach to the ATR crystal. Therefore, the ATR-FTIR can provide robust *in situ* measurements of the solution.

The IR spectra from a solution are determined by two factors: (i) the concentration of the chemical species ; (ii) the temperature of the solution.

$$\mathbf{y} = f(c, T) \tag{2.22}$$

where $y \in \mathbb{R}^{N_w}$ is the IR absorpance at N_w wavenumbers. Estimation of the solution concentration c requires the inversion of Equation (2.22) with known $\mathbf{y}$ and T. Therefore, $h = f^{-1}$ should be determined by some training experiments.

$$c = h(y, T) \tag{2.23}$$

The heights or areas of some prominent peaks can be used as the index of concentration to establish the correlation h. Then h is a polynomial function of the peak heights (or areas) and the temperature. Another approach to determining the solute concentration is using chemometric methods [15, 26, 130], such as principle component analysis and partial least squares regression.

ATR-FTIR is widely used to provide prompt solution measurements in process monitoring [20, 70, 72] and control [23, 33, 34, 78] of crystallization. With similar physical principles, ATR-UV/Vis [21, 121, 12] employs the radiation at different wavelengths to determine solution concentration.

2.4.3 Raman spectroscopy

Different from light transmittance in IR or UV/Vis, Raman spectroscopy is a light scattering technique. The samples are illuminated by a monochromatic laser source and the scattered light is shifted to different wavelengths due to the interaction of photons with the molecular vibrations of the sample. The scattered light at various wavelengths is collected and can be used to analyze the composition of the sample [80, 41]. The schematic is shown in Figure 2.14.

In crystallization applications, one major disadvantage of *in situ* Raman spectroscopy is that both liquid and solid phase can result Raman scattering. Properties of both phases need to be considered for quantitative purposes, and thus, a number of factors, such as suspension density, solute concentration, crystal size, and temperature can influence the Raman spectra [15]. However, with a robust chemometric method, the Raman spectroscopy can distinguish the changes within the solid phase,

24
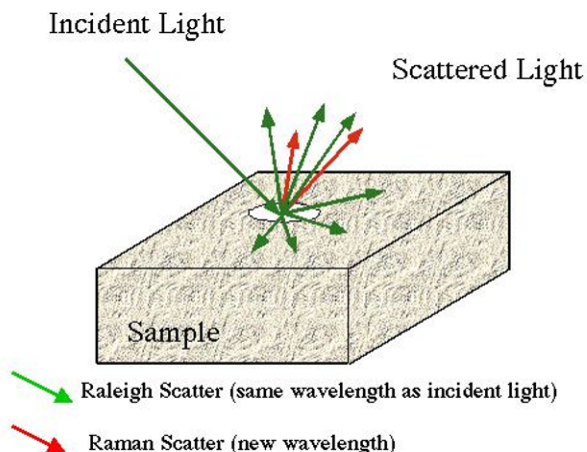
Figure 2.14: The schematic of Raman spectroscopy, image courtesy of www-che.engr.ccny.cuny.edu/courses/che5535

such as polymorphic transformation. The development of the chemometric methods are similar to what has been used for ATR-FTIR and ATR-UV/Vis, with the training samples coming from multiple crystal forms. Therefore, polymorphic transformation can be monitored and modeled [106, 108, 137]. Raman spectroscopy is often applied together with other probes to facilitate monitoring and control polymorphic transformation [9, 24, 107, 115].

2.4.4 Particle image analysis

Real-time images can be taken with a probe that integrates a camera with illumination. Size and morphology of the crystals can be qualitatively determined from the images. To obtain quantitative information about the CSD, not only high-resolution and sharp-contrast images are required, but also powerful image processing algorithms are essential to the identification and sizing of the crystals. Algorithms have been developed to isolate particles from their background for both prismatic [10] or needle-shaped crystals [116, 67]. When the slurry has high solid concentration, overlapped particles are problematic [136]. A Review of current image processing methods can be found in Zhou *et al.* [149].

2.5　Parameter estimation of crystallization kinetics

As described earlier, the crystallization processes are determined by the thermodynamics and kinetics. The thermodynamics property is a function of state, irrelevant to the path that system acquires the state. It can be measured if sufficient time is given to the system to achieve equilibrium. On the other hand, kinetics are the rates of occurrence for certain events, dependent on the transient states of the system. Therefore, in the study of crystallization kinetics, measurements must be taken during the process, and certain models are required to describe the phenomena of crystallization.

2.5.1　Induction time experiments

Induction time is usually related to the nucleation rate [97]. For a supersaturated solution, there is a delay between the achievement of saturation and the observation of crystallization in an unseeded process. In induction time experiments, the supersaturation is assumed to be achieved instantaneously, such as quenching a small amount of solution or mixing anti-solvent with a solution. The time of delay is defined as induction time.

The observable nucleation is the outcome of primary nucleation and growth of nuclei to an observable size. Therefore, the induction time consists of time spent on primary nucleation t_{ind} and time of growth t_g [54].

$$t_{ind} = t_n + t_g \tag{2.24}$$

Usually t_g is negligible, compared with t_n, hence

$$t_{ind} = t_n \tag{2.25}$$

If the appearance of the first nucleus indicates the onset of nucleation, then

$$t_n = 1/B_1 \tag{2.26}$$

26

Therefore, t_{ind} is the reciprocal of the nucleation rate [58]. From Equations (2.6), (2.7) and (2.8), the induction time can be related with the supersaturation, the temperature, and the interfacial tension. For Equations (2.6) and (2.8),

$$\ln t_{ind} = -lnk_{b1} + \frac{B}{T^3(\ln S)^2} \tag{2.27}$$

Equation (2.27) has been applied in many experimental observations, in which straight lines were fitted [30, 31, 83, 138]. In some studies [46, 77, 109, 122, 125], two regimes that had different slopes were observed, as shown in Figure 2.15. The two regimes are usually explained by the transition from heterogeneous nucleation to homogeneous nucleation when supersaturation increased. Steep slope with low $(\ln S)^{-2}$ (high S) suggests high interfacial tension, which means that homogeneous nucleation occurs with high supersaturation.
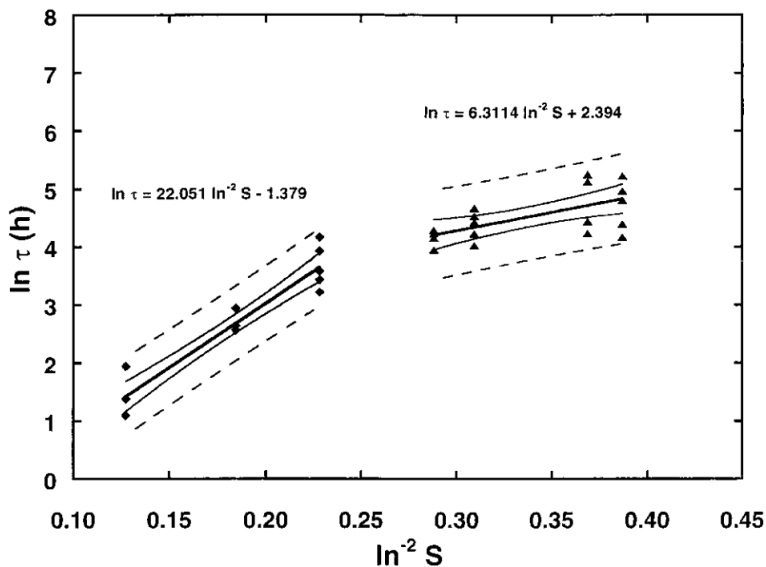
Figure 2.15: Two regimes in induction time measurements. Induction time denoted by τ. Reprinted with permission from [109]. Copyright 2001 American Chemical Society.

External energy exerted on the solution is found to enhance the nucleation rate and reduce the induction time. Two energy sources have been studied, including sonication and shear rate (agitation). Experimental evidence has been shown that

27

ultrasound can change the intercepts [38, 81] and slopes [82] of the fitted straight lines, i.e. the rate constant and interfacial tension were influenced by the sonication. Induction times under different shear rates were measured in a Taylor-Couette flow system [79]. The results suggested that the rate constant of primary nucleation increased when high shear was applied.

Another phenomenon associated with induction time is its high variability, as can be seen in the wide error bar in Figure 2.15. The stochastic model of the induction time assumes that the number of nuclei at time t follows Poisson's law [51, 110].

$$P(m,t) = \frac{N(t)^m \exp(-N(t))}{m!} \qquad (2.28)$$

in which $P(m,t)$ is the probability of finding m nuclei at time t, and N is the expected number of nuclei. Then the probability of no nucleation at t is

$$P(m = 0, t) = \exp(-N(t)) \qquad (2.29)$$

Therefore, the probability of the onset of nucleation at t is

$$P_{nuc}(t) = 1 - \exp(-N(t)) \qquad (2.30)$$

Equation (2.30) explains the probability of nucleation happens before time t, i.e. $t_{ind} < t$. Therefore, $P_{nuc}(t)$ is the cumulative density function of t_{ind},

$$P(t_{ind} < t) = 1 - \exp(-N(t)) \qquad (2.31)$$

Therefore, the probability density function of t_{ind} is the derivative of t

$$P(t_{ind} = t) = \exp(-N(t))N'(t) \qquad (2.32)$$

and $N(t)$ can be calculated by

$$N(t) = \int_0^t BV_{cryst} \, d\tau \qquad (2.33)$$

where V_{cryst} is the volume of the crystallizer.

According to this stochastic model, the effects of the primary nucleation rate B [51, 53, 63, 145] and the volume of crystallizer V_{cryst} [53, 54, 123] on induction time were investigated. Figure 2.16 shows the cumulative distributions of t_{ind} at different supersaturations. Kinetic parameters of primary nucleation can be estimated by fitting the stochastic model with the measured distributions. Figure 2.17 shows that a large volume of crystallizer reduces the randomness of the onset of nucleation.
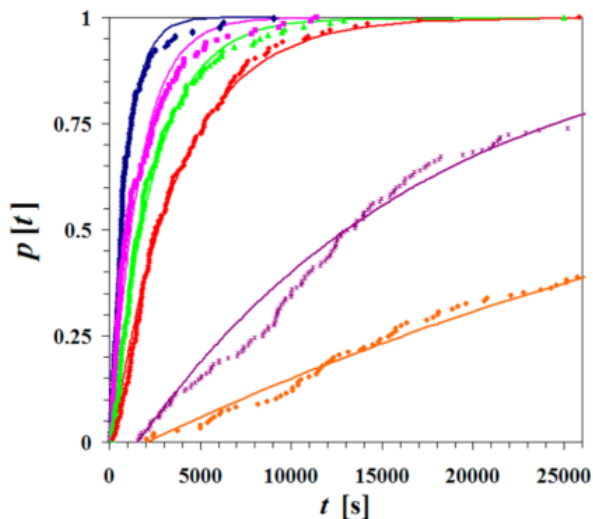
Figure 2.16: Cumulative distribution of induction time changed with supersaturation. Isonicotinamide nucleates at 5 different supersaturation ratios $S = 1.26$ (orange dots), 1.30 (brown X), 1.36 (red dots), 1.40 (green triangles), 1.44 (pink squares) and 1.48 (blue diamonds). Reprinted with permission from [63]. Copyright 2013 American Chemical Society.

2.5.2 PBE-based approach

The kinetic parameters can be estimated by fitting the solution of the PBE to experimental data, if some *ex situ* or *in situ* measurements are available, such as sieving, laser diffraction, IR spectra, FBRM, or Raman spectra. Two categories of modeling methods are candidates for solving PBE: one is based on the moments transformation of PBE (MOM, QMOM) and the other one is directly solving the PBE with proper
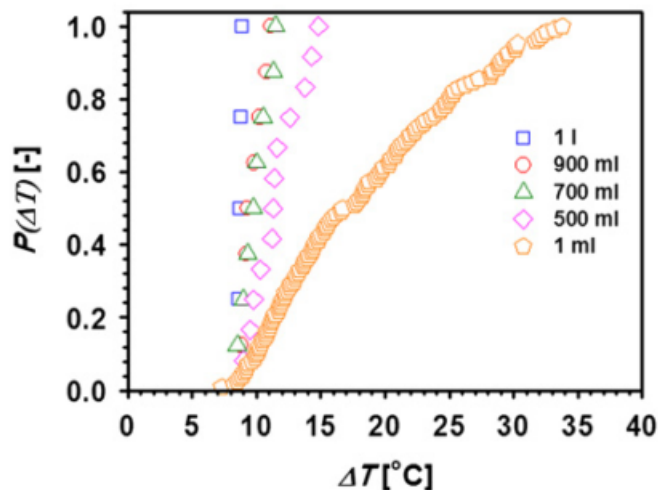
Figure 2.17: Metastable zone width measured in different crystallizer volumes in paracetamol-water system. Reprinted with permission from [54]. Copyright 2012 Elsevier.

numerical methods. The choice of the modeling method is determined by the measurements one can obtain.

Studies on crystallization kinetics that combined measurement tools and PBE models are summarized in Table 2.1. As we can see, earlier studies used the density of liquid to correlate with concentration, which may not be applicable for some systems, as stated by Hu *et al.* [48]. The development of ATR-FTIR has made the *in situ* determination of concentration achievable and it has facilitated many studies in crystallization kinetics [2, 45, 77, 92, 140]. However, parameters of nucleation and growth cannot be resolved only with concentration data [27], since both can decrease the concentration. As a result, additional measurements from CSD are necessary for estimation of kinetic parameters.

The measurement of the CSD has advanced significantly from off-line methods to on-line or *in situ*, as we can see in Table 2.1. FBRM has been commonly used to monitor the change of the particle size. However, quantification of the CSD is still a challenging task, so the moments of the CLD are usually used, assuming they are

proportional to the moments of the CSD. The correlation is based on the assumption that the mapping between the CLD and the CSD is static, i.e. the mapping is constant regardless of the changes of the CSD. In fact, it may not be always hold in a crystallization process, where the size of crystals varies by nucleation, growth, breakage, and agglomeration. The first-principles models (the geometric model and the optical model) have been applied successfully [140, 16], but they are less popular due to their complexity.

Table 2.1: A survey of kinetic parameter estimation

Authors	Year	Kinetics	System	Seeded	Model type	Measurements	Objective
Miller and Rawlings [90]	1994	Sec. nuc., growth	KNO_3–water	Y	MOM	Laser transmittence for μ_2, densitometer for c	c, μ_2
Monnier et al. [94]	1997	Prim. nuc., sec. nuc., growth	Adipic acid–water	N	PBE	Calorimter for supersatureation at onset of primary nucleation, image analysis of final CSD	Final CSD
Tadayon et al. [128]	2002	Sec. nuc., growth	$(NH_4)_2C_2O_4$–water	Y	MOC	Laser diff. for final CSD, liquid density for c	Final CSD, c
Togkalidou et al. [131]	2004	Sec. nuc., growth	N/A	Y	MOM	μ_{CLD} for μ_{CSD}, ATR-FTIR for c	μ_i, $i = 0, \ldots, 4$, c
Worlitschek and Mazzotti [140]	2004	Sec. nuc., growth, dissolution	Paracetamol-EtOH	Y	Galerkin-h,p	CSD estimated from CLD (geometric model), ATR-FTIR for c	S, $\mu_0/\mu_0(t=0)$, CSD
Hu et al. [48]	2005	Sec. nuc., growth(size depend.)	$(NH_4)_2SO_4$–water	Y	MOC	Laser diff. of final CSD, liquid denisty is inaccurate for c	Final CSD
Nagy et al. [100]	2008	Prim. nuc., growth	Paracetamol-water	N	MOM	μ_{CLD} for μ_{CSD}, ATR-FTIR for c	μ_i/μ_0, $i = 1, 2, 3$, c
Hermanto et al. [45]	2008	Polymorphic trans., sec. nuc., growth	L-glutamic acid–water	Y	MOM	$\mu_{\text{CSD},1}$ for $\mu_{\text{CSD},1}$, ATR-FTIR for c	μ_1, c

Table 2.1 continued: A survey of kinetic parameter estimation

Authors	Year	Kinetics	System	Seeded	Model type	Measurements	Objective
Aamir et al. [2]	2009	Sec. nuc., growth(size depend.)	KAlSO$_4$-water	Y	MOC, QMOM	Online laser diff. for CSD, online concentration measurements	CSD, c
Lindenberg et al. [77]	2009	Prim. nuc., growth	Acetylsalicylic acid in EtOH, water as antisolvent	N	DPB	ATR-FTIR for c	Supersaturation
Czapla et al. [16]	2010	Sec. nuc., growth	Threonine(D/L)-water	Y	MOC	CLD (optical model), optical rotation	optical rotation, normalized moments of CLD
Mitchell et al. [92]	2011	Growth	Paracetamol-EtOH	Y	MOM	ATR-FTIR for c	Supersaturation
Kee et al. [60]	2011	Sec. nuc., growth	L-phenylalanine-propanol-water	Y	MOM	μ_{CLD} for μ_{CSD}, ATR-FTIR for c	$\mu_i, i = 1, \ldots, 4, c$
O'ciadha et al. [105]	2012	Sec. nuc., growth, agglomeration	Paracetamol-MeOH	Y	MOM	μ_{CLD} for μ_{CSD}, ATR-FTIR for c	$\mu_i, i = 0, \ldots, 4, c$
Gherras et al. [27]	2012	Prim. nuc., sec. nuc., growth	(NH$_4$)$_2$C$_2$O$_4$-water	N	MOC	Final CSD by image analysis, ATR-FTIR for c	c, final CSD
Ochsenbein et al. [104]	2014	2D-growth (size depend.)	β L-glutamic acid-water	Y	FVM	Two characteristic lengths of needle-shaped parties, ATR-FTIR for c	c, CSD

2.6　Summary

In this chapter, several important aspects of crystallization have been reviewed, including thermodynamics, kinetics, modeling, and current measurement techniques. Thermodynamics and kinetics have been studied for over a century. Major kinetic events have been identified and the mathematical models are available. The population balance model, incorporating the kinetic equations, can be solved with various numerical methods. Currently, the research about crystallization is largely limited by the observation techniques. When the crystals are considered as a population, the observations on the macroscopic scale are of great help in understanding various crystallization kinetics, which leads to better manipulation of manufacturing processes. Concentration can be successfully measured, as reported in many studies. Information about CSD is critical to understand crystallization kinetics, but the use of CSD is limited by the lack of a convenient and powerful measuring tool. Such service can be potentially provided by the FBRM, which is the objective of this doctoral study.

CHAPTER III

ESTABLISHMENT OF THE EMPIRICAL FBRM MODEL IN NONSOLVENT

3.1 Objective

To establish a descriptive yet simple FBRM model is the aim of this chapter. An accurate first-principles model is preferred but it demands a dedicated Monte Carlo model that can mimic the FBRM process. In addition to the Monte Carlo model, many calibration experiments are required in order to determine the parameters in the model. However, there are always some features that are difficult to describe by physical model, such as surface roughness of the crystals. Therefore, an empirical model of FBRM is proposed and established, which neglects the physical process in the FBRM measurement. Assuming a linear transformation from CSDs to CLDs, the model considers the FBRM as a blackbox model, taking the sizes of crystals is as the input and providing the CLDs as responses, thus it is a matrix mapping CSDs to CLDs. The matrix can be determined experimentally by adding crystals from a specific sieve tray to a nonsolvent. The recorded CLD is defined as the fingerprint vector of the size range. Linearity and additivity of the empirical model should be validated by experimental results as well. If the results is successful, algorithms that estimate CSD from CLD can be developed.

Procedures and results in this chapter are reprinted with permission from [71]. Copyright 2013 Elsevier.

3.2 Method

3.2.1 Theoretical derivation of the FBRM model

The empirical model is generated from a discretized equation for modeling the CLD-CSD relationship. The experimental data are used to estimate the values of every entry in the transformation matrix.

Chord length distribution $q(s)$ is a density function, deduced as a convolution form [139]. Define $n(L_0)$ as the number density of crystals at an infinitely small size interval around L_0 in the sampling volume of the FBRM. Such crystals at L_0 lead to a certain CLD $q^{L_0}(s)$ by a transformation function $q_p(s, L_0)$.

$$q^{L_0}(s) = q_p(s, L_0)n(L_0)dL \tag{3.1}$$

The resulting $q^{L_0}(s)$ also depends on FBRM settings, for instance, the sampling time, but all those factors are incorporated in $q_p(s, L_0)$ as long as they are kept unchanged. Notice that both sides of Equation (3.1) are distribution density functions and $n(L_0)dL$ is a scalar, so $q_p(s, L_0)$ stands for the CLD induced by crystals at size L_0. If such equations of crystal size from zero to infinity are summed up, we have the following equation:

$$q(s) = \int_0^\infty q_p(s, L)n(L)dL \tag{3.2}$$

where $q(s)$ $[\#/\mu m]$ is the total CLD as a function of chord length s. $n(L)$ $[\text{no.}/(\mu m\, mL)]$ is the CSD function, and $q_p(s, L)$ is the CLD for a single crystal CLD at size L. Thus, the unit of $q_p(s, L)$ is $\text{mL}/\mu m$.

By defining

$$q_i = \frac{\int_{s_i}^{s_{i+1}} q(s)ds}{s_{i+1} - s_i} \tag{3.3}$$

$$n_j = \frac{\int_{L_j}^{L_{j+1}} n(L)dL}{L_{j+1} - L_j} \tag{3.4}$$

Equation (3.2) can be reformulated into a discrete matrix form:

$$\mathbf{q} = A\mathbf{n} \tag{3.5}$$

where $\mathbf{q}$ and $\mathbf{n}$ are chord length density and population density vectors, respectively. If $q_p(s, L)$ in a size bin $[L_j, L_{j+1}]$ is assumed to be constant, the square root of $L_j L_{j+1}$ is assumed to be the representative size for the jth bin. Each element in the matrix A, $A_{i,j}$, is obtained as

$$A_{i,j} = \frac{L_{j+1} - L_j}{s_{i+1} - s_i} \int_{s_i}^{s_{i+1}} q_p(s, \sqrt{L_j L_{j+1}}) ds \tag{3.6}$$

In order to turn the density vectors into histogram vectors, decomposing the equation with the bin width Δs and ΔL leads to the following equation:

$$\begin{bmatrix} 1/\Delta s_1 & 0 & \dots & 0 \\ 0 & 1/\Delta s_2 & \dots & 0 \\ \vdots & \vdots & \ddots & \vdots \\ 0 & 0 & \dots & 1/\Delta s_p \end{bmatrix} \begin{bmatrix} q_1 \Delta s_1 \\ q_2 \Delta s_2 \\ \vdots \\ q_p \Delta s_p \end{bmatrix} =$$

$$A \begin{bmatrix} 1/\Delta L_1 & 0 & \dots & 0 \\ 0 & 1/\Delta L_2 & \dots & 0 \\ \vdots & \vdots & \ddots & \vdots \\ 0 & 0 & \dots & 1/\Delta L_r \end{bmatrix} \begin{bmatrix} n_1 \Delta L_1 \\ n_2 \Delta L_2 \\ \vdots \\ n_r \Delta L_r \end{bmatrix} \tag{3.7}$$

The histogram vector for s has the same bin discretization as the FBRM data, so the measured chord length histogram (CLH) from the FBRM can be used directly. Note that the number of bins for chord length is p and that for crystal size is r.

Two vectors $\mathbf{b}$ and $\mathbf{x}$ are defined to stand for CLH and crystal size histogram (CSH), respectively.

$$\mathbf{b} = \begin{bmatrix} q_1 \Delta s_1 \\ q_2 \Delta s_2 \\ \vdots \\ q_p \Delta s_p \end{bmatrix} \qquad \mathbf{x} = \begin{bmatrix} n_1 \Delta L_1 \\ n_2 \Delta L_2 \\ \vdots \\ n_r \Delta L_r \end{bmatrix}$$

37

The matrix U is defined as

$$U = \begin{bmatrix} \Delta s_1 & 0 & \dots & 0 \\ 0 & \Delta s_2 & \dots & 0 \\ \vdots & \vdots & \ddots & \vdots \\ 0 & 0 & \dots & \Delta s_p \end{bmatrix} A \begin{bmatrix} 1/\Delta L_1 & 0 & \dots & 0 \\ 0 & 1/\Delta L_2 & \dots & 0 \\ \vdots & \vdots & \ddots & \vdots \\ 0 & 0 & \dots & 1/\Delta L_r \end{bmatrix}$$

Equation (3.7) then can be rewritten as

$$\mathbf{b} = U\mathbf{x} = \sum_{i=1}^{r} x_i \mathbf{u}_i \tag{3.8}$$

Here $\mathbf{b}$ and $\mathbf{x}$ are vectors that stand for histograms of CLD and CSD, respectively, in which each element is the number in a particular bin. Thus, $\mathbf{b}$ has the same format as the data structure of the FBRM (chord count no.) so that the FBRM measurement can be used directly. Similarly, $\mathbf{x}$ represents the crystal size population histogram, containing the volumetric concentrations of crystals in each size interval [# of crystal/mL]. Therefore, matrix U relates the CLH $\mathbf{b}$ and CSH $\mathbf{x}$.

The transformation matrix U is determined from experimental results instead of a first-principles model, since it is unknown that how a chord is generated and what factors have an impact on the measurement. However, from a statistical point of view, it is assumed that for a given size range of a fixed shape, the CLH is a constant vector $\mathbf{u}_i$. Note that $\mathbf{u}_i$, the fingerprint for size range i, is the ith column of U as shown in Equation (3.8). The CLH, $\mathbf{b}$, is a linear combination of the different fingerprints, where the coefficients are the crystal concentrations x_i [#/mL].

3.2.2 Inversion Techniques

Inversion of Equation (3.8) is required to estimate the CSH. Usually if a matrix is ill-conditioned, which is true for this case, the inversion would be subject to oscillation. One solution to this problem is using a smoothing term which numerically approximates the derivative at each data point [141]. Regularized minimization is

38

used:

$$\min_{\mathbf{x}} \quad \| U\mathbf{x} - \mathbf{b} \| + \lambda f(\mathbf{x}) \tag{3.9}$$

$$\text{s.t.} \quad x_i \geq 0, i = 1...r$$

$$f(\mathbf{x}) = \sum_{i=0}^{r-2} \left[\frac{(x/\Delta L)_{i+2} - 4(x/\Delta L)_{i+1} + 3(x/\Delta L)_i}{L_{i+2} - L_i} \right]^2, x_0, l_0 = 0$$

The second term in Equation (3.9) penalizes the change of derivatives to make the function smooth, using the first-order finite difference approximation for the first derivatives. The value of its weight λ is important to the accuracy because a large weight may emphasize too much on smoothing, failing to maintain the shape of the original CSD. Conversely, a small weight helps little on the oscillation suppression.

Another method uses principal component analysis (PC method), which considers the important features of the transformation matrix U to regress $\mathbf{x}$. Multiplying U^T on both sides of Equation (3.8) and defining $\tilde{\mathbf{b}} = U^T b$ and $\tilde{U} = U^T U$, we have

$$\tilde{\mathbf{b}} = \tilde{U}\mathbf{x} \tag{3.10}$$

The important features are identified by the eigenvalues of $\tilde{U}$ according to Grover et al. [35]. The errors are greatly amplified on those features with small eigenvalues, and thus these small-eigenvalue features are neglected. Suppose k eigenvectors, $\mathbf{c}_i, i = 1, ..., k$, corresponding to large eigenvalues, are chosen as principal components. $\mathbf{x}$ is a linear combination of these principal components with a non-negativity constraint, as shown in Equation 3.11. Both of the two optimization problems are quadratic and solved by *fmincon* of MATLAB on a Core i3 CPU.

$$\min_{\mu} \quad \| \tilde{U}(\sum_{i=1}^{k} \mu_i \mathbf{c}_i) - \tilde{\mathbf{b}} \| \tag{3.11}$$

$$\text{s.t.} \quad x_i \geq 0, i = 1...r$$

$$\mathbf{x} = \sum_{i=1}^{k} \mu_i \mathbf{c}_i$$

3.3 Materials and Experiments

To construct U, we carry out experiments to obtain CLH and CSH. Paracetamol (SigmaAldrich, 99%) crystals, which are obtained by batch cooling crystallization from its ethanolic solution, are sieved into nine size fractions. Then a known amount of crystals is added to toluene (BDH, 99%). As a nonsolvent of paracetamol, toluene does not induce significant change in the shape and size of the crystals, which is confirmed by our microscopy observations. The experiments are carried out in a 500 mL vessel with 400 rpm agitation to guarantee sufficient mixing.

The CLH vector **b** is measured by a D600 FBRM (Mettler Toledo) every ten seconds. The FBRM is set in fine mode, and the 1- to 1000- μm chord range is divided into 90 bins logarithmically. The noise of the FBRM is always an issue that affects measurement of CLH, especially when the solid fraction is low. To minimize the signal-to-noise ratio, the focal point was adjusted to 250 μm. However, even under such settings, chord counts in the first 30 bins (1 to 30 μm) are noisy and those in later bins are nearly zero. Therefore, only bins in the middle range are considered as qualified data for modeling. For the non-weighted CLH, the 46th to 75th bins are selected, which is from 30 μm to 300 μm. The CLH vector $\mathbf{b} \in \mathbb{R}^{30}$ is the system output that can be analysed under various CSH inputs $\mathbf{x} \in \mathbb{R}^9$, as discussed in the following section. For length weighted or length-square weighted CLH, the 47th to 84th bins (34–584 μm) are selected.

3.4 Results and Discussions

3.4.1 Sieving and FBRM Tests

Paracetamol crystals were sieved into nine fractions (20–53 μm, 53–75 μm, 75–106 μm, 106–150 μm, 150–200 μm, 200–250 μm, 250–300 μm, 300–425 μm, and 425–500 μm) and optical photomicrographs of three fractions are pictured in Figure 3.1. Paracetamol has three polymorphic forms and the stable and dominating form is
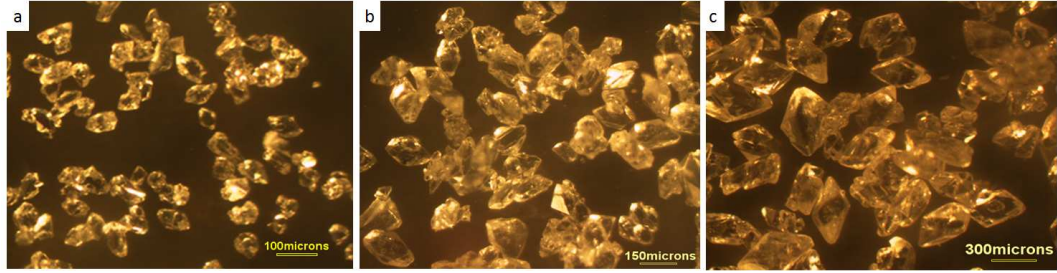
Figure 3.1: Microscopic photo of three size ranges: (a) 20 μm to 53 μm; (b) 106 μm to 150 μm; (c) 250 μm to 300 μm

Form I (monoclinic) according to the Beyer *et al.* [8]. Crystals obtained in this form from batch cooling crystallization appeared as octahedrons as shown in Figure 3.1. However, in all three size fractions in Figure 3.1, a portion of the crystals are imperfect octahedrons, presumably because of stirrer-crystal collision or crystal agglomeration. Accounting for these irregular shapes and their optics in first-principles models may be time consuming or even impossible. This is one motivation for developing an empirical model.

Another reason for developing an empirical model is that, if we put four different sizes into the non-solvent toluene, the normalized CLHs have similar shapes, as shown in Figure 3.2. It can been seen that there is no significant differences except a peak
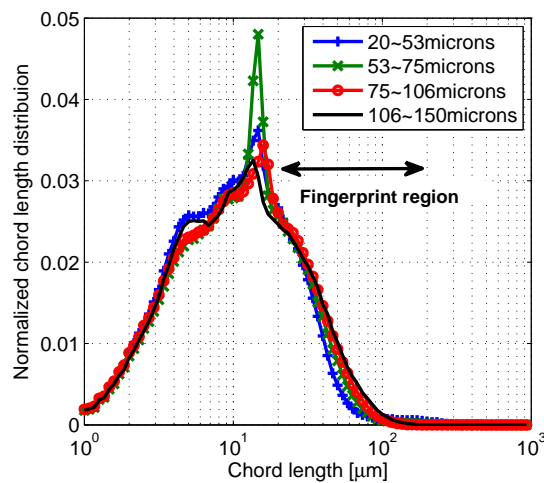
Figure 3.2: Chord length distributions of four size ranges measured by the FBRM. The histograms are direct unweighted FBRM measurements and plotted as dots instead of bars to make them clear.

41

around 20 μm, which is probably caused by a scratch on the probe window. This is inconsistent with first-principles models, where the simulated CLHs should follow a fixed shape. Furthermore, according to such models, the statistics of the CLH, such as modes, means, and longest chords, should be proportional to the crystal size being used in the simulation, but such features are not observed in Figure 3.2. Therefore, an empirical model is needed to incorporate all the factors that cause these phenomena.

3.4.2 Verifying Linearity: Single Size Crystal Addition

To demonstrate our empirical approach, we observe the chord count vector $\mathbf{b}$ when the crystals only from the kth size range are added into the vessel. The change in CLH after each addition is investigated. In Equation (3.8), if $x_i = 0, i = 1, 2, ...r$ for $i \neq k$, we have

$$\mathbf{b} = x_k \mathbf{u}_k \tag{3.12}$$

Summing all components,

$$\sum_{i=1}^{p} b_i = x_k \sum_{i=1}^{p} u_{k,i} \tag{3.13}$$

which means the total chord counts should be proportional to the number of crystals. To obtain $\mathbf{u}_k$ for a given $\mathbf{x}_k$, we can use

$$\mathbf{u}_k = \frac{\mathbf{b}}{x_k} \tag{3.14}$$

Crystals from 212 μm–250 μm, corresponding to $k = 6$, are chosen as an example. In our case, $p = 30$ and $r = 9$.

In Figure 3.3(a), the total chord count of non-weighted CLH in bins 46–75 is plotted against the crystal concentration. As we can see, the crosses on Figure 3.3(a) indicate a linear trend, as fit by the straight line. The linearity is also demonstrated by the convergence of fingerprint vector $\mathbf{u}_6$ in Figure 3.3(b). Since the signal-to-noise ratio is relatively high when the crystal concentration is small, $\mathbf{u}_6$ is subject to noticeable variability in Additions 1, 2, and 3 in Figure 3.3(b). However, once the crystal
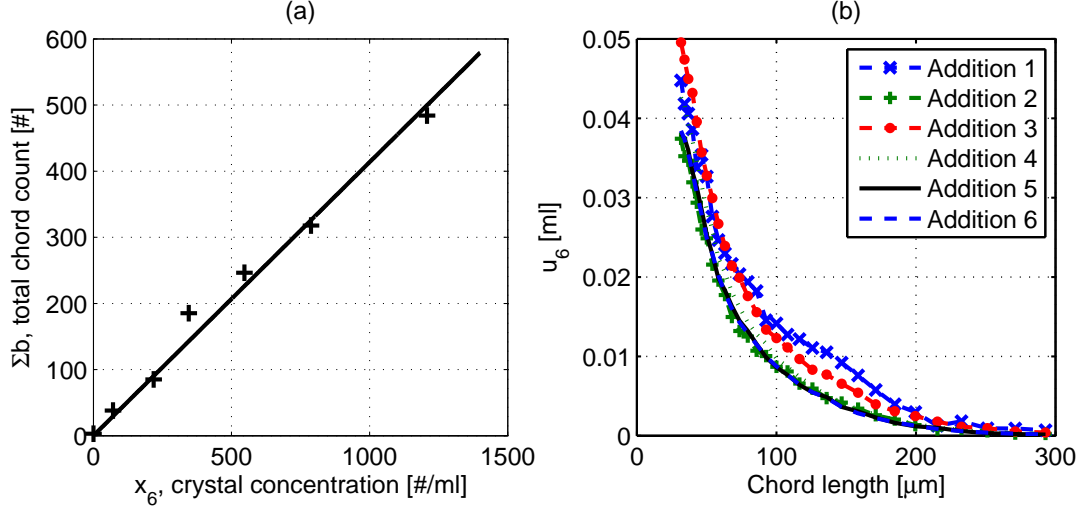
Figure 3.3: (a) Total chord count vs. crystal concentration for crystals in the 212-250 μm tray; (b) Fingerprint vector $\mathbf{u}_6$ calculated after each addition

concentration is high enough, the noise is no longer significant and $\mathbf{u}_6$ becomes constant (Additions 4, 5, and 6). Therefore, $\mathbf{u}_6$ is determined by $\mathbf{b}/x_6$ after the final addition and is named as the fingerprint of the crystals of size 212–250 μm.

The same experiments for all nine size fractions were carried out and the fingerprints for the nine ranges were obtained, as shown in Figure 3.4(a). Figure 3.4(b) is the sum of each fingerprint vector, $\sum_{i=1}^{p} u_{i,k}$ for size range k, against the size of the crystals to show the crystal size dependence of total chord count. It can be seen that
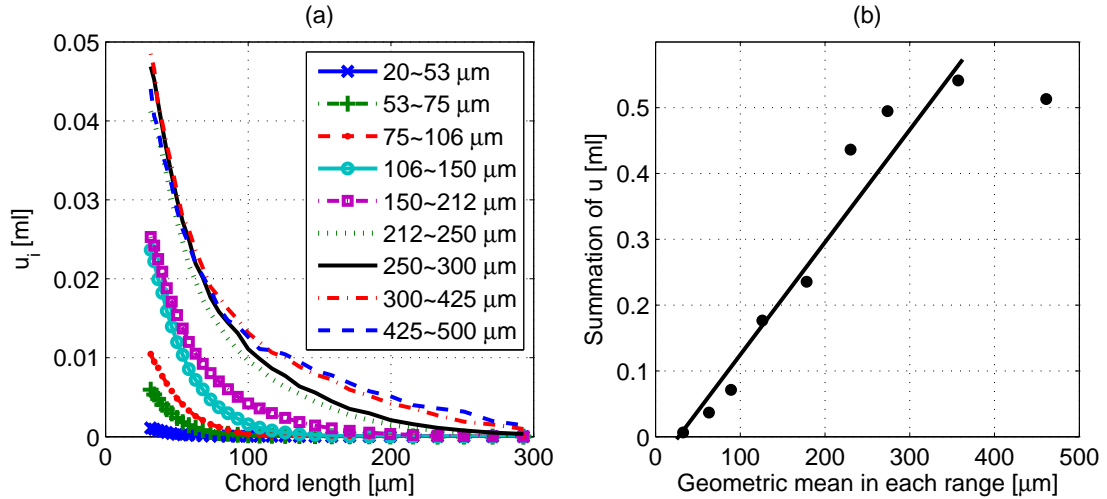
Figure 3.4: (a) Fingerprint for each size range; (b) Chord generation vs. crystal size

the chord count trend is nearly proportional to the size of the crystals except for the last data point. An explanation for this outlier is this size may reach the limit of the empirical model. To validate this point, more data from crystals above 500 μm may be needed. However, for the purpose of crystallizing APIs, it is rarely necessary to estimate the fraction of this size range and any range above, since the population densities are usually negligible. Generally, the figure demonstrates that larger crystals have a higher possibility to be detected by the FBRM, which corresponds to the usage of length-weighted crystal size distribution in the construction of the mapping matrix by first principles [139].

After obtaining the fingerprints for individual size ranges, the next step is to check the interactions between crystals of different sizes.

3.4.3 Verifying Additivity: Mixing of Different Sizes

In this section, we use a crystal suspension to investigate whether the fingerprint vectors are sensitive to pre-existing crystals of a different size. The following equation describes the additivity

$$\mathbf{b} = x_k \mathbf{u}_k + x_j \mathbf{u}_j, k \neq j \tag{3.15}$$

Assuming x_k is known and invariant, we treat the data $(\mathbf{b} - x_k \mathbf{u}_k)$ and $\mathbf{u}_j$ in the same way as in the previous experiments.

In one of the experiments, a 400-mL toluene suspension containing 5 gram of 106–150 μm (bin 4) crystals is prepared, and crystals of size 75–106 μm (bin 3) are then added to the suspension. Because x_4 is known and invariant, in Figure 3.5(a) the total chord count $\sum_{i=1}^{p}(\mathbf{b}_i - x_4 \mathbf{u}_{4,i})$ is plotted against the concentration of 75–106 μm crystals. The resulting linearity of adding 75–106 μm crystals is not interfered by the pre-existing 106–150 μm crystals. In Figure 3.5(b), the converged fingerprint $(\mathbf{b} - x_4 \mathbf{u}_4)/x_3$ is compared with three fingerprints from Section 4.4.2. The fingerprint for bin 3 obtained in this experiment is nearly identical to the fingerprint in the single

crystal addition in Section 4.4.2. The fingerprints of neighboring fractions (53–75 μm and 106–150 μm) are also shown in this figure. As can be seen in this figure, a notable difference is observed from the neighboring fingerprints, and the slight deviation due to the pre-existing crystals can be considered negligible. From this experiment, we conclude that the fingerprints are nearly constant under 3% volume fraction [vol. of crystal / vol. of toluene], although there is another size of crystal present in the suspension.
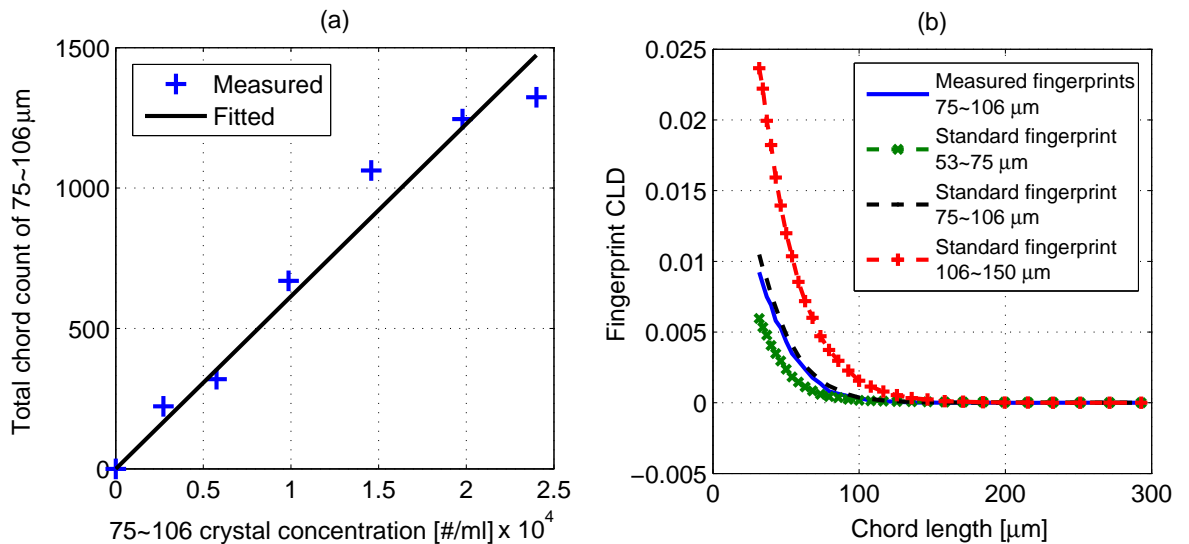
Figure 3.5: (a) Total chord count of 75–106 μm crystals in a suspension containing 106–150 μm crystals at each addition; (b) Fingerprint obtained in this experiment and comparison with previous fingerprint results

3.4.4 Length Weighted and Length-Square Weighted Fingerprints

Besides the non-weighted CLH, length-weighted CLH and length-square-weighted CLH as alternatives in estimating CSD are also investigated. In theory, the weighting methods should make no impact on the linearity and additivity because they are just different linear numerical treatments. Nevertheless, a better weighting leads to construction of a better conditioned matrix U.

The range of chord lengths included in the analysis is limited to 34 μm to 584

μm, which totals 38 bins. The weighted value in each bin is the product of the chord count and the geometric mean of that bin as shown in Equation (3.16) (or the square of the geometric mean for length-square weighting in Equation (3.17)).

$$b_{l,i} = b_i \tilde{l}_i \tag{3.16}$$

$$b_{lsq,i} = b_i \tilde{l}_i^2 \tag{3.17}$$

where,

$$\tilde{l}_i = \sqrt{l_i l_{i+1}} \tag{3.18}$$

By comparing Figure 3.6 with Figure 3.3, It can be seen that the differences between sizes are more obvious when the weighting strategies are applied. In length-square
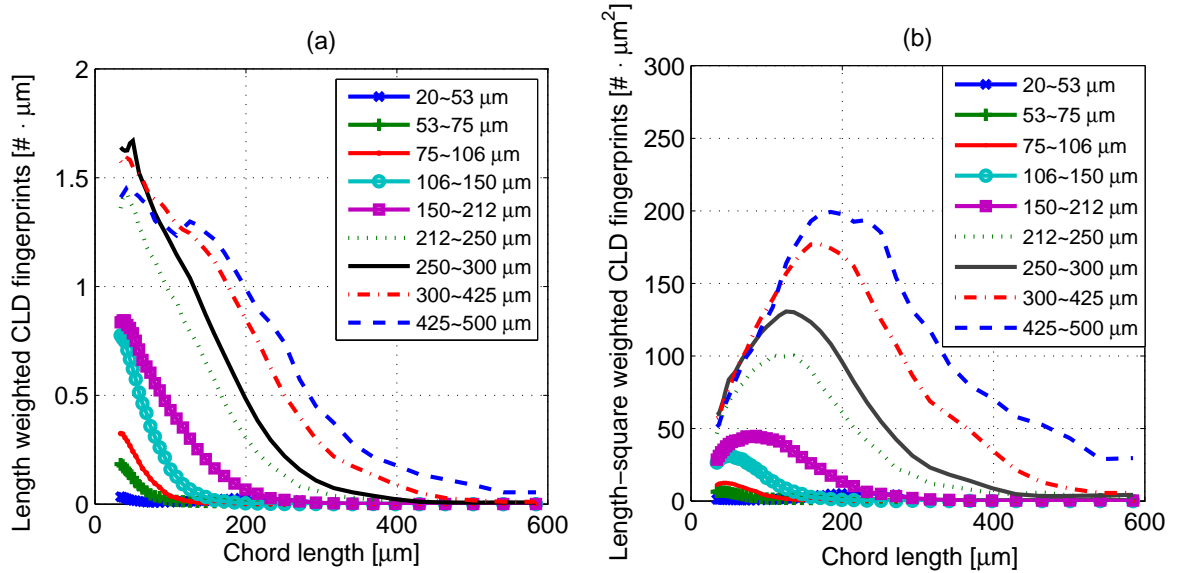
Figure 3.6: (a) Fingerprints from length weighted CLD; (b) Fingerprints from length-square weighted CLD

weighting, the shape of each fingerprint turns into a curve with a peak in the middle, whereas the shape of the non-weighed fingerprints always has a monotonically decreasing slope. Such a difference may impact the inversion of the transformation matrix, which is used in estimating CSD from measured CLH. As shown in Table 3.1, all the matrices are ill-conditioned, which means that the FBRM measurement is dominated by large particles since their fingerprint vectors are much higher. Length-square

Table 3.1: Comparison of different weighting methods

Weighting	Bin	Condition number of $U^T U$
Nonweighted	46–75	1.06×10^7
Nonweighted	38–84	9.48×10^6
Length	38–84	1.99×10^6
Square	38–84	1.96×10^6

weighting and length weighting have similar condition numbers, which is almost one order of magnitude smaller than the non-weighted one. Because the length-square weighting has the smallest condition number, we employ this weighting approach in the study.

3.4.5 Matrix Inversion for CSD Estimation

3.4.5.1 Simulation Study

The two techniques explained in Section 2.2 are studied with simulated data in this section. The simulated CLH is corrupted by an uncorrelated Gaussian noise, whose amplitude is estimated from the experiments. The CLH, $\mathbf{b} = U\mathbf{x} + \epsilon$, is formulated with the U matrix and a designed CSH $\mathbf{x}$. Ten noise-corrupted CLH data sets were created for a monodispersed distribution, a unimodal distribution, and a bimodal distribution, respectively. The estimated results and the known $\mathbf{x}$ are converted to $\mathbf{n}$, the population density distribution. Note that nine sieve trays are used to approximate a crystal size distribution, where the crystal size of each point is the geometric mean of its size ranges.

For the regularization method (see Equation (3.9)), the objective function has two terms in order to decrease the difference between estimation and observation as well as to suppress oscillations. Five weighting values of λ are chosen, 1×10^2, 1×10^3, 1×10^4, 1×10^5, and 1×10^6, which represent five smoothing strategies from weak to strong. A known histogram $\mathbf{x}_0$, is estimated in N runs with varied noise, denoted

as $\mathbf{x}_i, i = 1, ..., N$. $\bar{\mathbf{x}} = (\sum_{i=1}^{N} \mathbf{x}_i)/N$ is the mean of the CSH estimates and the CSD estimates $\{\bar{x}_j/\Delta L_j\}, j = 1, ...r$, are plotted in Figure 3.7. In our case, $N = 10$ and $r = 9$.

For the unimodal distributions, as can be seen in Figure 3.7(a) and (b), when λ is decreased, no oscillations appear and the estimates converge to the true value. On the other hand, given a bimodal distribution, the number of modes and their
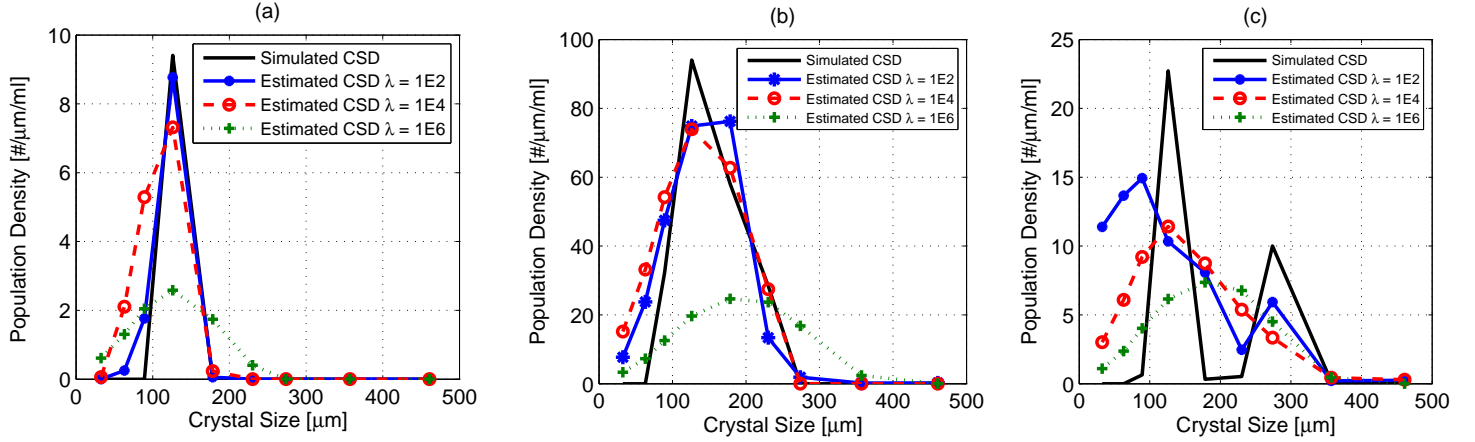
Figure 3.7: CSD used in simulation and estimates with five λ values: (a) Monodispersed distribution; (b) Unimodal distribution; (c) Bimodal distribution

locations depend on the value of λ. When λ is greater than 1×10^4, the second mode disappears. Weak smoothing can reveal the second mode but the location of the first mode is shifted. Therefore, if this method is used, the value of λ should be selected carefully, particularly if the CSD is not expected to be smooth.

Define estimation error as

$$\sum_{i=1}^{N} ||\mathbf{x}_i - \mathbf{x}_0||_2^2$$

where $\mathbf{x}_0$ is the true CSD. To expose the variation introduced by the noise, the maximum deviation over all bins is divided by the largest value in the estimate to define the maximum variation:

$$\frac{\max\limits_{j=1,..,r} \sqrt{\sum_{i=1}^{N} \frac{1}{N-1}(x_{i,j} - \bar{x}_j)^2}}{\max\limits_{j=1,..,r} \bar{x}_j}$$

Table 3.2: Estimation results for regularized optimization

Distributions	λ ($\times 10^4$)	Estimation Error ($\times 10^5$)	Max. Variation (%)
Monodispersed	0.01	0.84	17
	0.1	1.5	11
	1	3.8	3.6
	10	6.4	1.6
	100	10.7	0.5
Unimodal	0.01	500	22
	0.1	264	14
	1	219	4.3
	10	442	2.6
	100	1620	2.3
Bimodal	0.01	158	99
	0.1	71.7	44
	1	80.0	17
	10	87.5	9.3
	100	87.4	9.5

Table 3.2 shows that mild smoothing is preferred to reduce the estimation error. The maximum variation column represents the robustness of this method against noise, which is the ratio of the maximum variation from the mean value divided by the maximum value of the estimated CSD. It illustrates that, for the unimodal distribution, the method is very robust with λ larger than 1×10^3. For the bimodal distribution, noise makes the CSD even more difficult to estimate. Notice that lowering the estimated error and decreasing the maximum error cannot be achieved at the same time. As a result, there is a trade-off between these two objectives. A value of λ between 1×10^3 to 1×10^4 decreases the estimated error and keeps the fluctuation of the estimates relatively low.

The simulated results of using different numbers of principal components are shown in Figure 3.8. As can be seen, the averaged CSD estimate from ten noisy CLH samples displays varied shapes with different number of principal components.

Detailed results on various regression settings are shown in Table 3.3. Similar to the regularization method, the PC method needs a user-defined parameter—number of principal components. Using fewer principal components leads to losing features. When more components are considered, noise amplifies the estimation error. Therefore, five principal components are selected to balance these two effects. Note that the bimodal distribution is not accurately estimated with either inversion method, indicating that the information content in the FBRM alone is not sufficient for this challenging distribution.
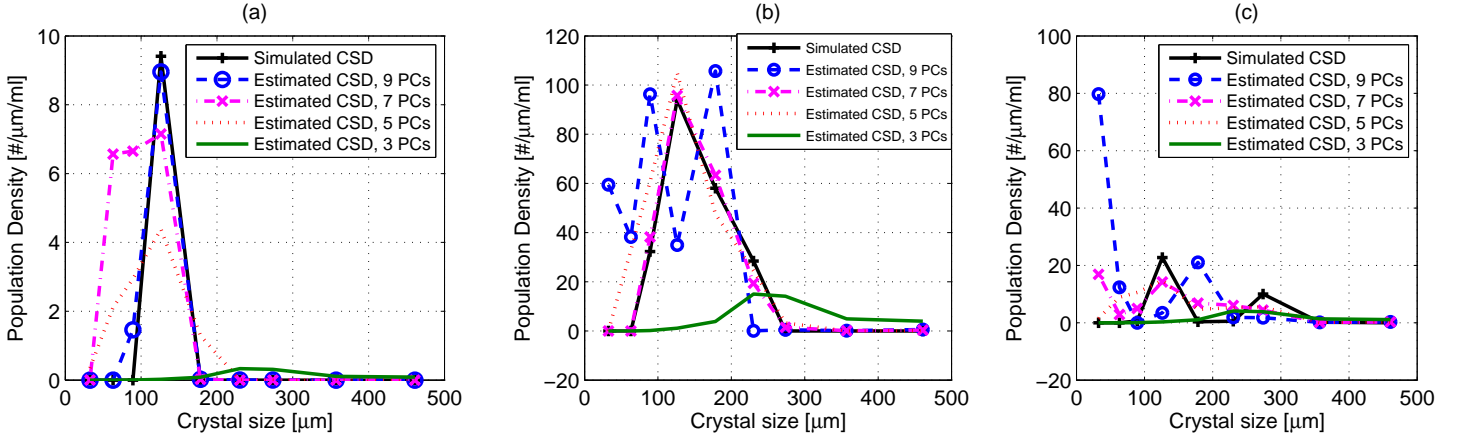
Figure 3.8: CSD used in simulation and estimated CSD by principle component method: (a) Monodispersed distribution; (b) Unimodal distribution; (c) Bimodal distribution

3.4.5.2 Experimental Validation

Based on the results above, the regularization method with $\lambda = 1 \times 10^3$ and the PC method with five principal components are validated in this section, using experimental CLH data.

A CSD, $\mathbf{x}_0$, was prepared by adding a known amount of crystals from each size fraction into a known volume of toluene, and its CLH is measured by the FBRM for this CSD. As the first step, some monodisperse suspensions were tested, which contain crystals only from one size fraction. In Figure 3.9, crystals of sizes 106–150 μm

Table 3.3: Estimation error results for principal component method

Distributions	No. of PC	Estimation Error ($\times 10^5$)	Max. Variation (%)
Monodispersed	4	7.58	4.50
	5	6.58	4.50
	6	7.08	0.451
	7	7.33	0.979
Unimodal	4	497	7.82
	5	215	6.83
	6	255	14.2
	7	42.3	6.04
Bimodal	4	51.8	15.6
	5	48.6	24.8
	6	57.6	40.5
	7	136	111

and 250–300 μm are measured by FBRM and the CSDs are estimated, respectively. It can be seen that both the regularization method and the PC method can estimate the correct peak location but they also expand the width of the peak.

The estimated CSD in Figure 3.10(a) is a mixture of four size fractions from 106
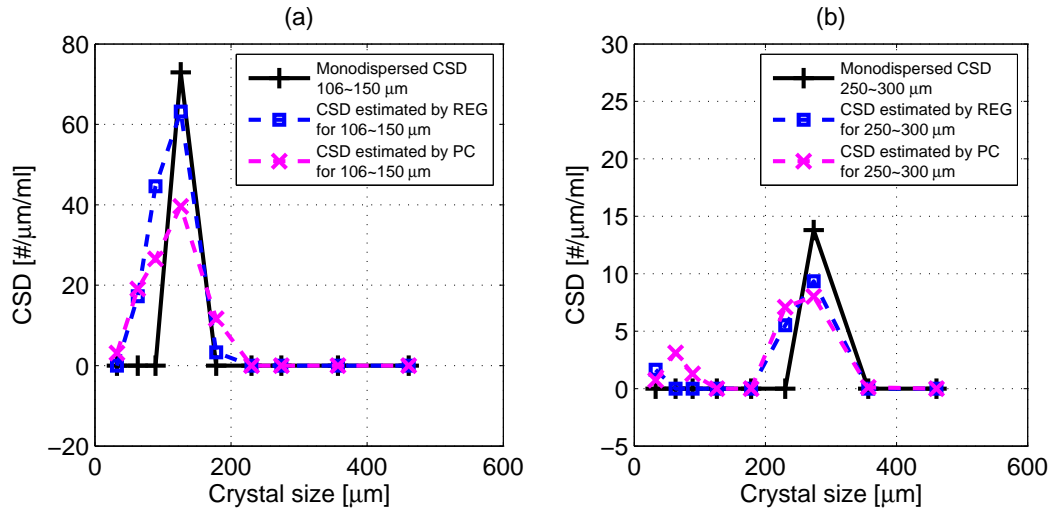
Figure 3.9: Monodispersed CSD estimation: (a) 106–150 μm crystals; (b) 250–300 μm crystals

μm to 300 μm. The estimated $\mathbf{x}_{REG}$ approximates the shape successfully, but with a certain amount of error. The PC method obtains the same peak location while the

peak is estimated to be wider. In Figure 3.10(b), the corresponding four CLHs are plotted. The match between the experimental length-square weighted CLH and our estimated CLH, $U\mathbf{x}_{REG}$ and $U\mathbf{x}_{PC}$, validates that the algorithm is capable of finding the best estimate. Moreover, the prediction of CLH by our empirical fingerprint model $U\mathbf{x}_0$ is also close to the measured CLH, which demonstrates the fingerprint approach is able to describe the FBRM measurement.

A more challenging case was also explored, which is a bimodal distribution of
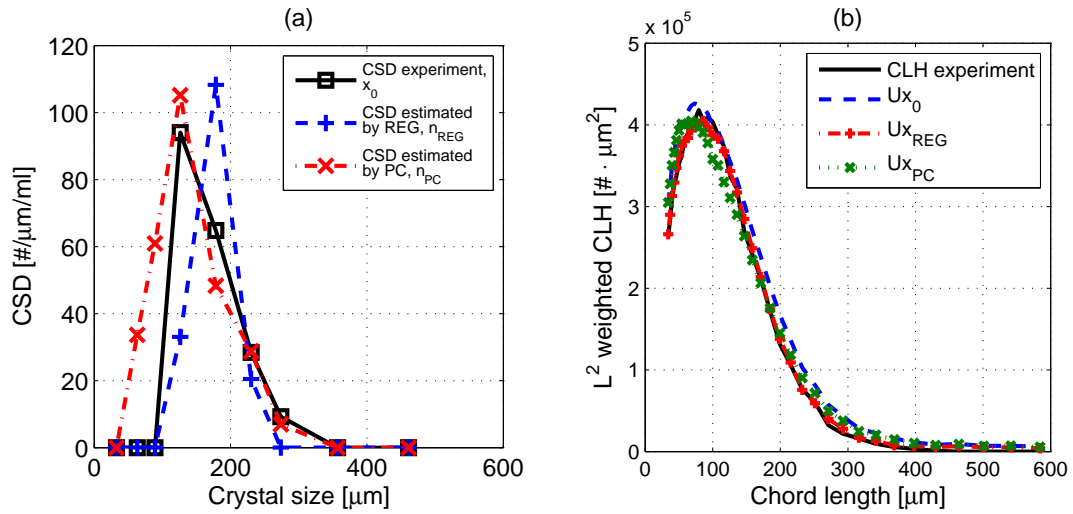
Figure 3.10: (a) Estimated CSDs with different methods; (b) Measured CLH and reconstructed CLHs

106–150 μm and 250–300 μm crystals. In this test, as shown in Figure 3.6(b), the fingerprint vector of the 250–300 μm crystals is much larger than that of the 106–150 μm crystals, which poses the challenge of identifying the smaller size crystals from the mixture. The crystal population densities of the two sizes of crystals are the same order of magnitude. As a result, the contribution of 250–300 μm crystals is dominant in the measured CLH, when multiplying a large fingerprint vector. In Figure 3.11(a), the regularization method finds two modes at lower bins. Two modes are also located by the PC method but the crystals are distributed into more size ranges. One reason is that large particles dominate the CLH and interfere with the

detection of small particles. Figure 3.11(b) shows that another reason is the difference between the experimental CLH and the model prediction by Equation (3.8), $U\mathbf{x}_0$. This mismatch originates from potential lack of linearity at large crystal sizes as observed in Figure 3.4(b). The measurement at around 275 μm (seventh point from left) corresponding to the larger crystals of the bimodal distribution is above the straight line, which might indicate that our calculated fingerprint overvalues the true one. As a result, $U\mathbf{x}_0$ is not consistent with the measured CLH. Such issues will be further studied in future research.

Since both optimization problems are quadratic and small-scaled, it only takes less than one second to perform the optimization, which allows on-line estimation feasible. Moreover, a Kalman filter combining a process dynamic model and sequential CLH measurements can reduce the variability of estimates caused by measurement noise [84].
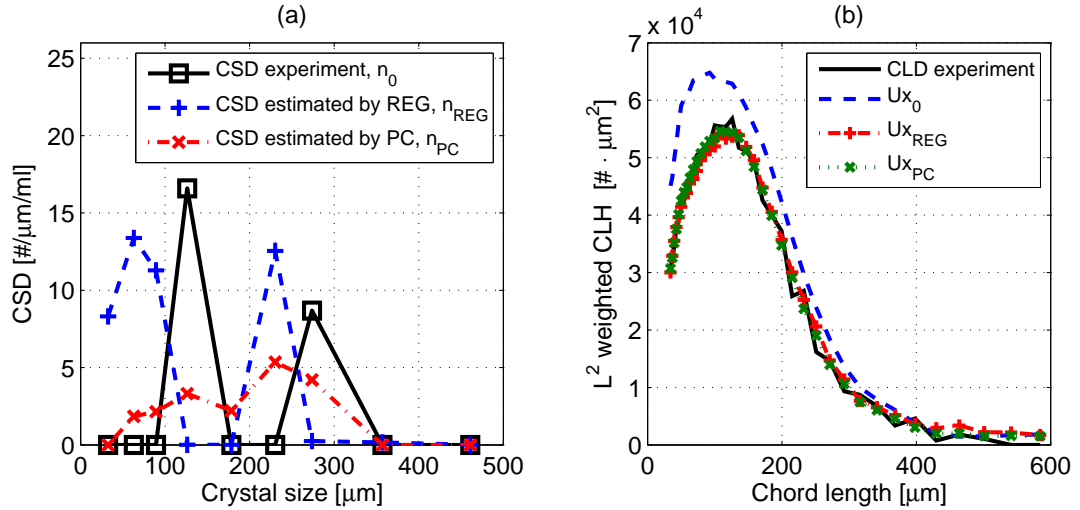
Figure 3.11: (a) CSD estimation for a bimodal distribution; (b) Comparison of measured and estimated CLH

3.5 Conclusion

The primary contribution of this work is the development of a method by which chord length data obtained with an FBRM instrument can be used in an empirical model to

estimate crystal (or particle) size distribution. The model offers the potential of real-time estimation of the CSD in crystallization processes from chord length histogram generated by the FBRM. This chapter illustrates how a matrix to transform from chord length measurements to CSD is determined from experimental data. In the process of developing the method, the linearity and additivity of such measurements have been validated.

To invert the transformation matrix properly, regularized least square and principle component analysis are first developed and then investigated in a simulated study. Both techniques are applied to systems of paracetamol crystals suspended in the non-solvent toluene. Our results showed the success of the empirical model in estimating CSD in a number of cases and we point out concerns about its general applicability. We also have shown the potential of on-line implementation. To demonstrate the advantages of the empirical model we have developed, our work will focus on how to overcome the high solid fraction and apply such model to a crystallization process.

CHAPTER IV

APPLICATION OF THE FBRM MODEL TO BATCH CRYSTALLIZATION

4.1 Objectives

In the previous chapter, the potential of FBRM as an *in situ* CSD observer has been shown in crystal-toluene slurry. Two algorithms of estimating the CSD from the CLD measured by the FBRM have been tested, and the CSD estimates are comparable with the experimental results with both two methods with a unimodal CSD. The estimate can be inaccurate when a bimodal distribution is measured.

This chapter targets at development of a framework that can determine the solute concentration and CSD from the IR spectra and the CLD measurements. Paracetamol-ethanol is selected as the model system. Modifications and reconstruction to the empirical model described in last chapter include:

- determination of fingerprint matrix in ethanolic solution of paracetamol

- validation of the linear model in the system

- quantification of the solute concentration from the IR spectra

- implementation of mass balance of the solute in solid and liquid phases

- refinement of the algorithm for CSD estimation

Procedures and results in this chapter are reprinted with permission from [72]. Copyright 2014 American Chemical Society.

4.2 Experimental setup

The experimental setup is shown in Figure 4.1. The ATR-FTIR is manufactured by Mettler Toledo, and it is commercially called ReactIR$^{\text{TM}}$ iC10. The FBRM$^{®}$ D600 is also from Mettler Toledo. All the other parts, including the temperature probe, stirring system, a 1-L glass crystallizer, and heating/cooling metal jacket, are assembled into the OptiMax$^{\text{TM}}$ from Mettler Toledo. The IR spectrum of the solution
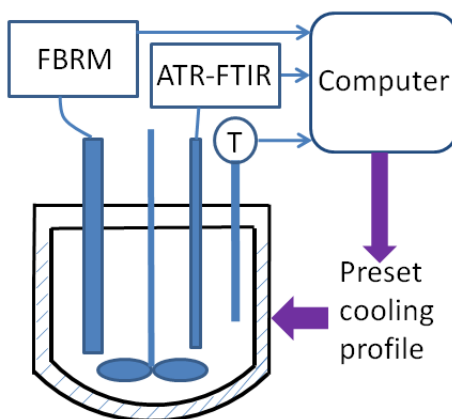
Figure 4.1: Experimental setup

from 653 cm^{-1} to 2998 cm^{-1} was measured every minute. The ReactIR$^{\text{TM}}$, purged by compressed air, is equipped with a diamond probe on a AgX interface. The FBRM$^{®}$ D600 was set in the fine mode, and the chord range from 1 to 1000 μm was divided logarithmically into 100 bins. The CLD histogram was recorded every ten seconds at 2 m/s scanning speed with 0 μm focal point, smoothed by an exponential filter. The temperature range was from 0°C to 70°C and the stirring speed was set at 400 rpm. These instruments monitored the crystallization process and communicated with a computer via the iC software from Mettler-Toledo (iC FBRM 4.2.234, iC IR 4.3.27, and iControl 5.1.29).

Paracetamol (SigmaAldrich, 99%) powder was dissolved in ethanol (SigmaAldrich, HPLC grade), some of which was recrystallized by batch cooling crystallization. The crystals are in Form I (monoclinic), which were in the shape of octahedra by our

micrograph observation. They were sieved into nine fractions (53–75 μm, 75–106 μm, 106–150 μm, 150–200 μm, 200–250 μm, 250–300 μm, 300–355 μm, 355–425 μm, and 425–500 μm) in a Ro-Tap$^{\circledR}$ RX-29 shaker. To measure the fingerprint CLD histograms, the crystals were added to a 400 mL saturated solution at 24°C. From the infrared spectrum, no change in solute concentration was observed on addition of the crystals. This indicated that the solution was well-equilibrated and no change in crystal size occurred after addition to the solution.

4.3 Method

4.3.1 Fingerprint model

The fingerprint for size range i is obtained in the following procedure: 1) the crystals in size range i are obtained from sieving, and these crystals are added to a saturated solution at multiple times. For each addition, the mass of crystals being added is measured, in order to calculate the crystal concentration in the suspension [# of crystals/mL]; 2) After the jth addition, the crystal concentration $\mathbf{x}_j$ was calculated. Since only $x_{i,j}$ is nonzero and $x_{k,j} = 0$ for $k \neq i$, $\mathbf{x}_j$ can be calculated by:

$$x_{i,j} = \frac{m_{crystal}}{k_V \rho l_i^3 V_{solution}} \tag{4.1}$$

where $m_{crystal}$ is the mass that has been added to the saturated solution, ρ is the density of paracetamol crystals, which equals to 1.263g/cm^3, l_i is the geometric mean of the ith size range, and $V_{solution}$ is the volume of the solution, which is assumed to be the volume of the ethanol that was used to prepare the solution. From our inspection with an optical microscope, the crystals have an octahedral shape, and the aspect ratio of longest and second longest dimensions is around 2.0. Thus the shape factor k_V is determined to be 1/3; 3) Fingerprint $\mathbf{u}_i$ for the same size range can be obtained by

$$\mathbf{u}_i = \frac{1}{x_{i,j}} \mathbf{b}_j \tag{4.2}$$

57

where $\mathbf{b}_j$ is the CLD measurement of the FBRM, which has unit [# of chords] and $x_{i,j}$ is crystal concentration [# of crystals/mL], the fingerprint $\mathbf{u}_i$ carries the unit of [# of chords·mL/# of crystals]. After several additions, $\mathbf{u}_i$ converges and its values are defined as the fingerprint for the ith size range. More details on the procedure can be found in our previous work [71].

Estimating the CSD histogram $\mathbf{x}$ from a known $\mathbf{b}$ requires the inversion of Equation (3.5). In practice, the matrix A is often ill-conditioned. To deal with this problem a regularization term is added to the least square minimization, as shown in Equation (4.3).

$$\min_{\mathbf{x}} \parallel U\mathbf{x} - \mathbf{b} \parallel_2^2 + \lambda f(\mathbf{y}) \tag{4.3a}$$

$$\text{s.t.} \ \ x_i \geq 0, \ i = 1, 2, ..., r \tag{4.3b}$$

$$y_i = l_i^3 \frac{x_i}{L_i - L_{i-1}}, \ i = 1, 2..., r \tag{4.3c}$$

$$f(\mathbf{y}) = \sum_{i=0}^{r-2} \left(\frac{y_{i+2} - 4y_{i+1} + 3y_i}{l_{i+2} - l_i} \right)^2, y_0 = 0 \tag{4.3d}$$

$$l_i = \sqrt{L_i L_{i+1}}, \ i = 1, 2, ..., r \tag{4.3e}$$

where r is the number of size ranges, L_i and L_{i+1} are the boundaries of the ith size range, and l_i is the geometric mean of the boundary values for the average size in each size range. The first constraint Equation (4.3b) enforces non-negative values for crystal concentrations. The second constraint Equation (4.3d) defines a penalty term that suppresses the oscillation in the CSD estimate; $\mathbf{y}$ is defined as the volume- or mass-weighted number density. The penalty function $f(\mathbf{y})$ is the sum of square of the forward difference approximation of the first-order derivative on the spatial direction. This function is multiplied by λ, which is the weight for the penalty term and chosen to be 1×10^{-10} $[\mu\mathrm{m/mL}]^{-2}$.

4.3.2 Quantification of IR spectra

In addition to information on the solids from the FBRM, the solution concentration is also investigated. As shown in Figure 4.2, paracetamol is highly soluble in ethanol; its solubility was reported in several references [31, 40, 140]. We suspect these values
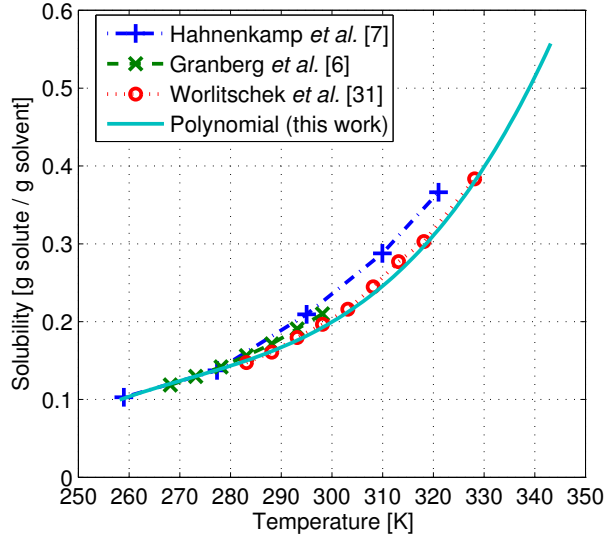
Figure 4.2: Solubility of paracetamol in ethanol

vary because of differences in methods and materials used in the experiments. Here, the lower bound of the solubility data was used to fit the third-order polynomial for the solubility c_s [g solute/g solvent] at the temperature T [K]:

$$c_s = 7.915 \times 10^{-7}T^3 - 6.439 \times 10^{-4}T^2 + 1.765 \times 10^{-1}T - 16.17 \qquad (4.4)$$

The infrared spectrum of the liquid phase is measured by attenuated total reflectance - Fourier transform infrared (ATR-FTIR) spectroscopy to estimate solute concentration. For paracetamol dissolved in ethanol, the spectrum depends on both temperature and concentration. We measured the IR spectra at various paracetamol concentrations (between 0.0 and 0.5 g solute/g solvent) and temperatures (between 0 and 70 °C). There are several approaches to quantify the solution concentration from the *in situ* spectra [15], including peak height/area regression, multi-wavelength

regression, principal component regression, and partial least square regression. In this study, we found that using peak heights is simple and sufficiently accurate. The AU at 1667 cm^{-1} is chosen as the characteristic peak of paracetamol and the AU at wavenumber 1048 cm^{-1} represents ethanol as shown in Figure 4.3, for such choice leads to good fitting between the peak height ratio and concentrations.

The ratio $h = AU(1667)/AU(1048)$ was correlated with temperature $T[\text{K}^{-1}]$ and
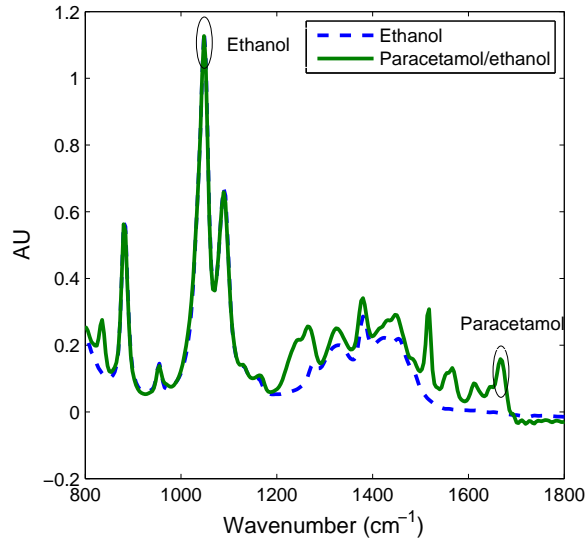
Figure 4.3: Infrared spectrum of paracetamol dissolved in ethanol

molar percentage of paracetamol X as in the equation:

$$h = k_1 X^2 + k_2 X (T - 273.15) + k_3 X + k_4 (T - 273.15) + k_5 \qquad (4.5)$$

The calibration experiments were carried out in a sealed and jacketed vessel. Five solutions with known concentrations were cooled from high to low temperature for calibration. With known h, X, and T, linear fitting yields estimates of $k_1 = -8.781(-)$, $k_2 = 1.974 \times 10^{-3}(\text{K}^{-1})$, $k_3 = 3.648(-)$, $k_4 = -2.546 \times 10^{-4}(\text{K}^{-1})$, $k_5 = -2.819 \times 10^{-4}(-)$ with $R^2 = 0.988$. The parity plot of the fitting is shown in Figure 4.4. The molar fraction can be calculated accordingly if h and T are obtained. Then the concentration estimated by IR, c_{IR}, is then: $c_{IR} = M_{w,paracetamol} X / M_{w,ethanol} (1 - X)$.

60
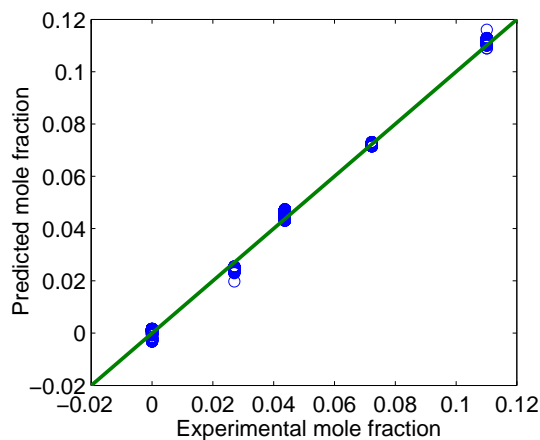
Figure 4.4: Calibration of peak height ratio to concentration at various temperature

We also carried out an *ad hoc* correction against day-to-day variability, which are mainly caused by differences on the background spectrum and optical fiber curvature [32]. In-run calibration is used by assuming that the concentration reaches the solubility value when the temperature is kept constant for a sufficiently long time. More specifically, the temperature is kept at 34°C and 0°C for about an hour in our experiment. Pure ethanol is also used for this calibration at $X = 0$ at temperatures from 0°C to 20°C. These three concentrations are used to linearly correct c_{IR} against the day-to-day variability. One example is shown in Figure 4.5
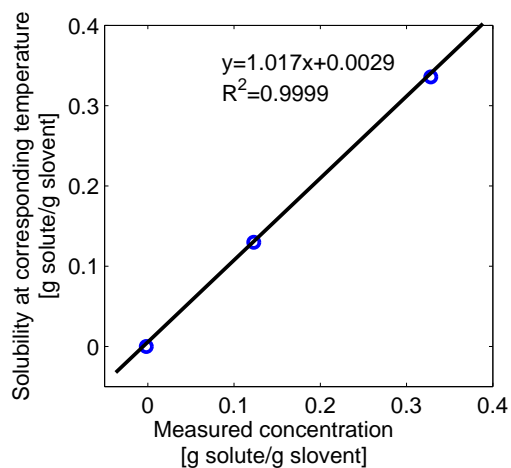
Figure 4.5: *Ad hoc* calibration to correct day-to-day variablity

4.3.3 Combination of FBRM and ATR-FTIR

The FBRM and ATR-FTIR measurements can be combined by the following mass balance equation:

$$m_{solid} + m_{liq} = m_{tot} \tag{4.6}$$

where m_{solid} and m_{liquid} are the mass of solute in solid and liquid phases, respectively, and m_{tot} is the total amount when the solution is prepared. If m_{liquid} and m_{tot} are known, m_{solid} can be calculated accordingly. The mass of the solid phase can be also obtained by:

$$m_{solid}(\mathbf{x}_{est}) \approx \sum_{i=1}^{r} m_{crystal,i} x_{est,i} \tag{4.7}$$

where $m_{crystal,i}$ is the mass per crystal in size range i. However, the CSD estimate $\mathbf{x}_{est}$ by Equation (4.3) may not always satisfy Equation (4.6) due to estimation error. In particular, large crystals have a stronger influence on the mass estimate and thus any slight error at the large crystal size can cause significant differences in the evaluation of crystal mass. We introduce a modification by calculating a scaling coefficient:

$$\hat{\mathbf{x}} = \frac{m_{tot} - m_{liq}}{m_{solid}(\mathbf{x}_{est})} \mathbf{x}_{est} \tag{4.8}$$

which satisfies $m_{solid}(\hat{\mathbf{x}}) + m_{liq} = m_{tot}$. We use $\hat{\mathbf{x}}$ as the estimate of CSD throughout this study.

Since the solid phase information and solution concentration are connected via the mass balance, we need to synchronize the two measurements from their own sampling intervals. The CLD measurement interval is set at ten seconds and the IR spectrum is taken every one minute. For each IR spectrum, four temporally closest CLDs are selected and their averaged CLD is calculated and defined as the CLD at the moment when the IR spectrum is recorded. Temperature values at each IR sampling time are obtained similarly. After the CSD estimates are obtained, a low pass filter, which is a moving average with window width of 10, is applied to reduce the fluctuation of the estimates in the temporal direction.

4.4 Results

4.4.1 Fingerprint CLD histograms

The fingerprint histograms of sieved paracetamol crystals were measured in saturated ethanolic solution, displayed as number-based and mass-based versions in Figure 4.6 and 4.7, respectively.
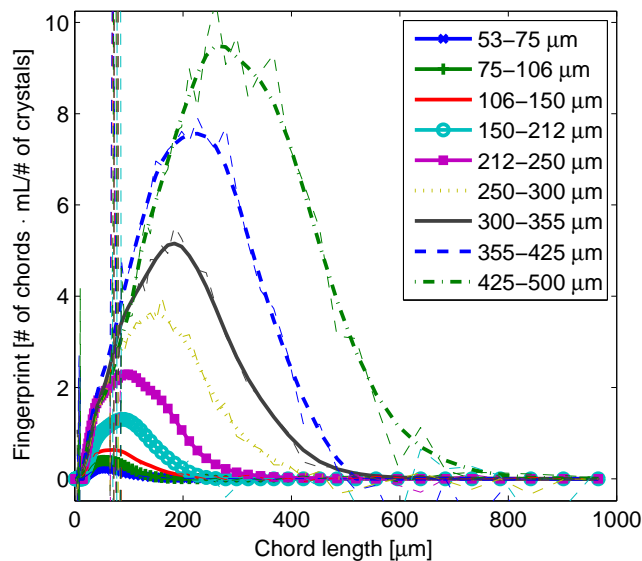
Figure 4.6: Number-based fingerprint histograms

The number-based fingerprint CLD histograms are shown in Figure 4.6, on the basis of the number of crystals suspended in the unit volume of the solution as derived in Equation (4.2). In the calibration of fingerprints, five or six additions are used and each addition has 0.2 to 2 g of crystals. The results are shown as the thin lines, which exhibited spikes, especially in the 65.3–85.7 μm region, probably due to the fouling of the probe. This region usually included three to five points and was smoothed by linear interpolation according to the neighboring data. The other slight oscillations were smoothed by a moving average filter using three data points to obtain the final fingerprints (thick lines). Figure 4.6 shows that the fingerprints become higher and wider when the crystal size increases, because large crystals occupy more space and have greater chance to reflect the laser beam. Such an observation suggests that
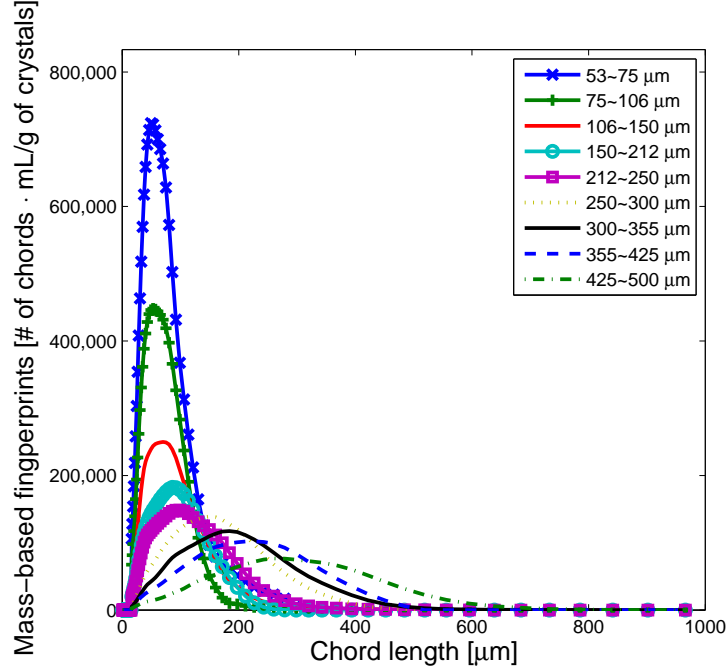
Figure 4.7: Mass-based fingerprint histograms

large crystals are more influential to the CLD than small crystals. The shapes and heights of the fingerprints suggest that this effect is very significant in our case. This property causes the ill-conditioning of the system, which requires the regularized least square method as shown in Equation (4.3). Assuming the growth of crystals is the prevailing process in the crystallizer, the total chord count should increase even though the number of crystals is approximately constant. Therefore, an increase in total chord count can result from growth and should not always be attributed to the birth of crystals.

On the other hand, since kinetics processes such as ripening or agglomeration may happen only within the solid phase, we are also interested in the mass-based fingerprint histograms. The mass-based fingerprint histograms are directly calculated by dividing the number-based fingerprints by the mass of one crystal ($\mathbf{u}_i / m_{crystal,i}$). These fingerprint histograms have the opposite trend as shown in Figure 4.7; for a fixed mass of crystals, more chords are observed if that mass is made of smaller

crystals. This is because, compared to the same mass of large crystals, small crystals can spread more pervasively, and therefore their chance of being detected is greater. If the crystals are agglomerating or ripening, for example, 1 gram of crystals at 50 μm turns into 1 gram of crystals at 100 μm due to agglomeration, we could expect that the total chord count would decrease.

4.4.2 Model Validation

To confirm the linearity of the FBRM model, we experimentally tested to see if the total chord count of a CLD changes linearly with a change of the CSD. If Equation (3.5) holds, then the following relationship is satisfied:

$$\sum_{i=1}^{p} b_i = \sum_{i=1}^{p} (U\mathbf{x})_i \tag{4.9}$$

Here we use two crystal size distribution samples: Sample 1 and Sample 2. These two samples have their own mass-based CSD histograms, $\mathbf{x}_{1,N}$ and $\mathbf{x}_{2,N}$. The mass of crystals in $\mathbf{x}_{1,N}$ or $\mathbf{x}_{2,N}$ is 1.0 g. If we change the CSD histogram by adding crystals either from Sample 1 or Sample 2, the CSD can be written as $\mathbf{x}^\gamma = k_1^\alpha \mathbf{x}_{1,N} + k_2^\beta \mathbf{x}_{2,N}$, where k_1 and k_2 are the masses of crystal from Sample 1 and Sample 2, and the superscript $\alpha = 1, 2, ..., P$ and $\beta = 1, 2, ..., Q$ represent the time index of additions of Sample 1 and 2 with the total number of additions $\gamma = \alpha + \beta$. Hence $\mathbf{x}^\gamma$ is the CSD histogram after the γth addition of crystals. Equation (4.9) can be reduced to

$$\sum_{i=1}^{p} b_i = k_1^\alpha \sum_{i=1}^{p} (U\mathbf{x}_{1,N})_i + k_2^\beta \sum_{i=1}^{p} (U\mathbf{x}_{2,N})_i \tag{4.10}$$

where $\sum_{i=1}^{p}(U\mathbf{x}_{1,N})_i$ and $\sum_{i=1}^{p}(U\mathbf{x}_{2,N})_i$ are constant. If we sequentially made P additions of Sample 1 and then Q additions of Sample 2, the total chord count should increase linearly, exhibiting two slopes, $\sum_{i=1}^{p}(U\mathbf{x}_{1,N})_i$ and $\sum_{i=1}^{p}(U\mathbf{x}_{2,N})_i$.

Samples 1 and 2 with CSD histograms shown in Table 4.1 were used to test the model in a saturated solution of 500 mL prepared at 24.2 °C. The mass-weighted mean sizes of crystals are 218 μm for Sample 1 and 247 μm for Sample 2. The first

seven additions of Sample 1 were all chosen to be less than two grams so that we can investigate if there exists a threshold where the CLD starts to behave nonlinearly. Figure 4.8 shows that the linear trend is well-maintained through the 14 additions of Sample 1 ($P = 14$). Six additions ($Q = 6$) of Sample 2 also showed proportionality between mass of crystals and total chord count with the presence of Sample 1. Notice that the slope of Sample 1 is higher than that of Sample 2, which agrees with the finding in the mass-based fingerprint discussion that small crystals generate more chords per unit mass. The normalized CLD histogram measurement calculated from the final slurry ($\mathbf{x}^{20}$) was compared with the normalized simulation result of Equation (3.5). The consistency of these two normalized CLDs also validates the linear model.

Table 4.1: The compositions of two CSD histograms

Pore opening [μm]	Mass percentage [%]	
	Sample 1, $\mathbf{x}_1$	Sample 2, $\mathbf{x}_2$
500	0.86	7.20
425	1.53	4.86
355	3.15	10.47
300	10.52	15.05
250	16.63	19.72
212	19.41	16.54
150	31.36	19.44
106	11.57	5.70
75	3.82	1.03
53	1.15	0.00
20	0.00	0.00
0	0.00	0.00

4.4.3 CSD monitoring

An experiment of batch cooling crystallization of paracetamol was monitored by both FBRM and ATR-FTIR, with the initial concentration at 0.385 g solute/g solvent. The cooling profiles were designed to include two cooling steps. The first one was cooling the clear solution to a temperature that created a high supersaturation and triggered
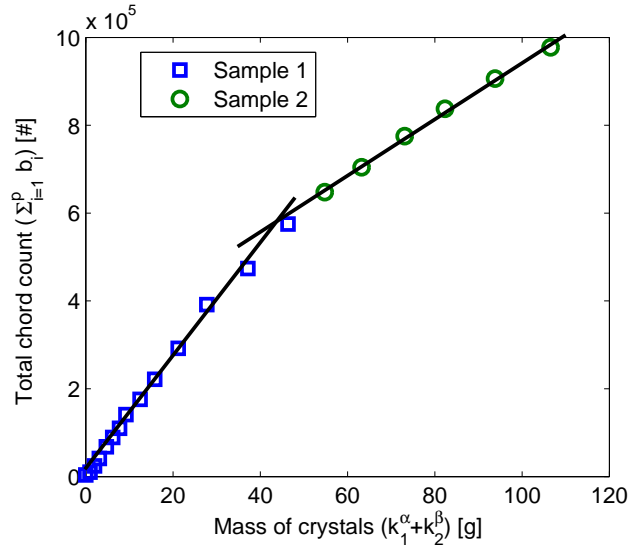
Figure 4.8: Total chord count after each addition
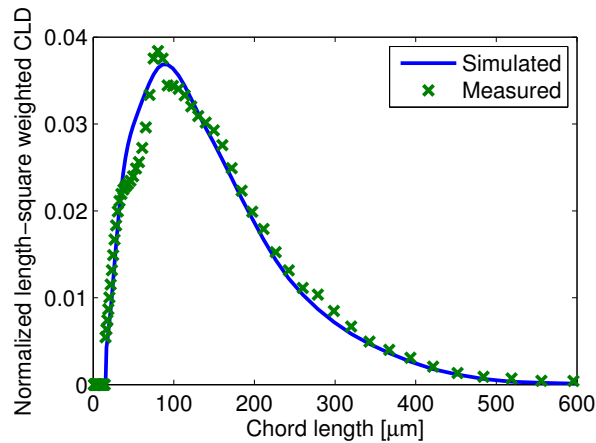
Figure 4.9: Comparison of model simulation and measurement of CLD of $\mathbf{x}^{20}$

primary nucleation. Then the temperature was held so that the crystals generated consumed the remaining supersaturation. The second cooling further decreased the temperature to the lowest operating temperature in order to induce further crystal growth in the absence of primary nucleation.

After the temperature was held at the final value for about 100 minutes, two post-run actions were performed sequentially to confirm that the supersaturation had been completely consumed: (1) adding paracetamol crystals to the slurry and (2) increasing temperature by 1°C. The purpose of adding crystals is to eliminate any

remaining supersaturation for the *ad hoc* concentration correction mentioned earlier. Furthermore, by comparing the concentration and solubility change after the slightly increase of temperature, we can confirm our concentration prediction is accurate. Such a minor increase of temperature is assumed not to change the CSD significantly for the subsequent sieving test.

The experimental procedure produced results referred as Run I and Run II. Since these two runs are similar, we discuss Run I first, and discuss Run II only briefly.

4.4.3.1 Run I: temperature and concentration

Temperature and concentration profiles for Run I are shown in Figure 4.10. In the first cooling step from 70°C to 34°C, the concentration was constant as there was no crystallization. The concentration then started to drop drastically at Point A, which is evidence that primary nucleation occurred at about 34°C, and the concentration rapidly decreased to the saturation value. Cooling was resumed at B and stopped at C when the temperature reached 0°C. In the period from B to D, supersaturation increased modestly and was depleted when cooling stopped.

In order to check the assumption of saturation at the end of the run, (1) 2.0
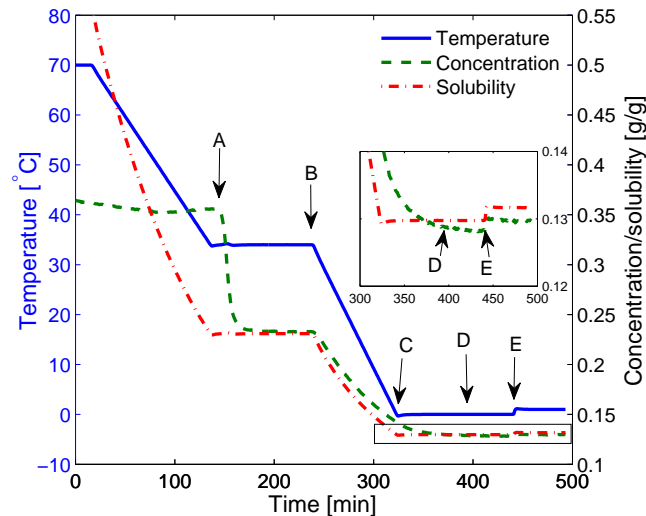
Figure 4.10: Temperature and concentration profiles of Run I

68

grams of crystals were added at D and (2) the temperature was raised to 1.0°C at E. Step (1) had no effect on the concentration. At Step (2) the concentration and solubility changed simultaneously and both increased by 0.002 g/g, which indicates there was little supersaturation before E.

The supersaturation ratio (c/c_s) during Run I is shown in Figure 4.11. Note that from Point B until the end of the experiment, the supersaturation ratio was lower than 1.1. From the variation of supersaturation, we cannot infer whether secondary nucleation occurred, but this question will be revisited later in the manuscript.
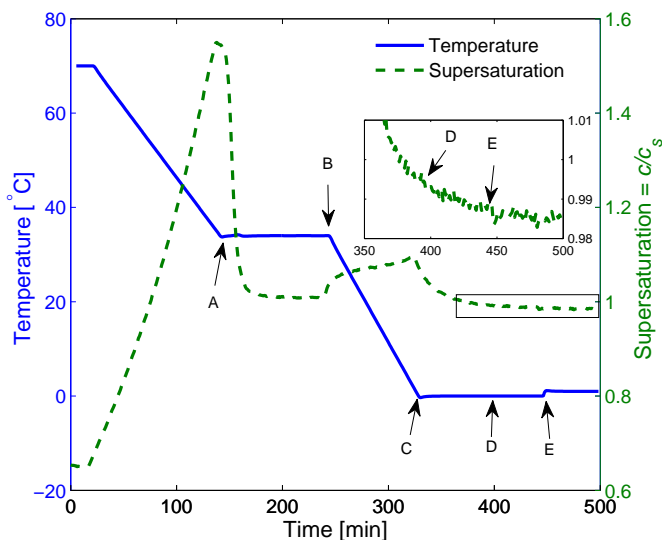
Figure 4.11: The supersaturation profile of Run I

4.4.3.2   Run I: tracking key parameters of CSD

The total number of crystals and mean size of the crystal population calculated from the CSD estimates are shown in Figure 4.12(a) and (b). They are compared with the total chord count and mean length from the CLD histogram, which are commonly used to represent the number of crystals and size of crystals.

Figure 4.12(a) shows that the total number of crystals obtained from the CSD estimates resulting from the developed model is more representative of the process
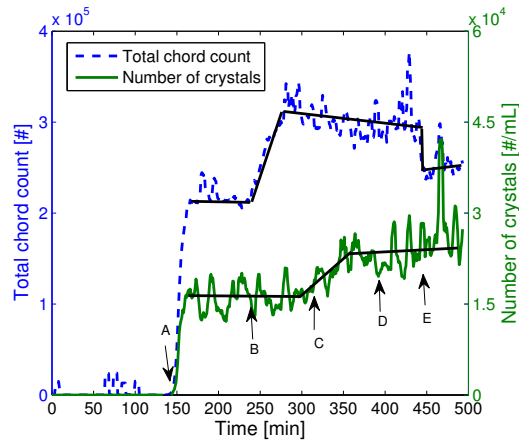
(a)
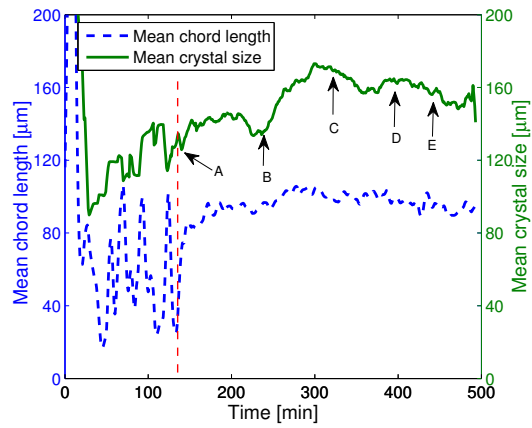
(b)

Figure 4.12: Comparison between CLD histogram measurement and estimated CSD histogram of Run I: (a) total chord count and estimated number of crystals (black lines for guiding the eye); (b) mean chord length and estimated mean size of crystals

than simply using the total chord count. For example, an increase in both the total chord count and the number of crystals indicate primary nucleation at A, but the subsequent total chord count shows a rapid increase at B that could be misinterpreted as nucleation. However, since the supersaturation ratio was close to 1 at B, as shown in Figure 4.11, the increase in chord counts is much more likely due to growth than to nucleation. This is an example of our analysis of fingerprint histograms in Figure 4.6: the total chord count highly increases with the size of the crystals, i.e., growth of crystals leads to an increase of the total chord count. Note that the estimated number of crystals was constant after B. When the process was approaching C, there was a slow increase in the number of crystals from 300 minutes to 350 minutes, probably caused by secondary nucleation. Such a change was not seen from the total chord count.

At D, neither of the total chord count nor the number of crystals responded to the addition of 2.0 g of crystals. Because these crystals were taken from the 100-g product of batch cooling crystallization operated similarly, it is reasonable that the 2% change in the population can hardly affect the CLD and the estimated CSD. At E, temperature was increased by 1.0°C, which corresponds to a crystal mass decrease of only 1.5% according to the solubility dependence on temperature. This minor dissolution of crystals was overestimated by the total chord count, which dropped suddenly. On the contrary, there was no substantial change in the estimated number of crystals.

For tracking the change of crystal size, the comparison in Figure 4.12(b) shows the capability of the mean size of the estimated CSD over the mean chord length. During the crystallization process, the crystal mean size was estimated from 130 μm at B to 175 μm at C, whereas the mean chord length varied only between 80 to 100 μm, which is not as large as that of the mean size. The CLD measurements prior to the red vertical line were considered as noise, since it was confirmed by visual inspection

that no crystals had been formed before A.

4.4.3.3 Run I: validation of CSD estimates

The estimated CSD density functions at A, B, C, and D are shown in Figure 4.13(a), which is obtained by applying Equation (4.3) and then transforming the estimated CSD histogram to the number density. The evolution of the CSD densities is consistent with our understanding of the kinetics of the process. At A, crystals appeared due to primary nucleation. The CSD at B was obtained after the supersaturation accumulated in the first cooling step was consumed. From B to C, the density functions had approximately the same height, whereas the numbers of crystals at small sizes decreased and those at large sizes were greatly increased, which suggests the growth of crystals in the second cooling step. The change from C to D, corresponding to the depletion of the remaining supersaturation after C as can be seen from Figure 4.11, also implied a slight growth of crystals.

These changes from A to D are also shown in the three-dimensional Figure 4.13(b). In addition, we can see that crystals at the first bin (smallest size) started to increase slowly at C, which indicates secondary nucleation. The secondary nucleation may have been triggered because the supersaturation was accumulated to its maximum value at C. In the subsequent period to D, these new-born crystals became larger and moved to the second bin ($75 - 106$ μm), and secondary nucleation gradually ceased because of the depletion of supersaturation. Therefore, the number density of the smallest size dropped again.

The estimated CSDs are demonstrated to be sufficiently accurate by comparing the final estimate with the sieving result, as shown in Figure 4.14. After the experimental run was completed, crystals were filtered, washed with toluene, and then dried in an oven. The mass histogram was obtained by sieving and recalculating to the number density. Only minor differences are seen between the estimated and

72
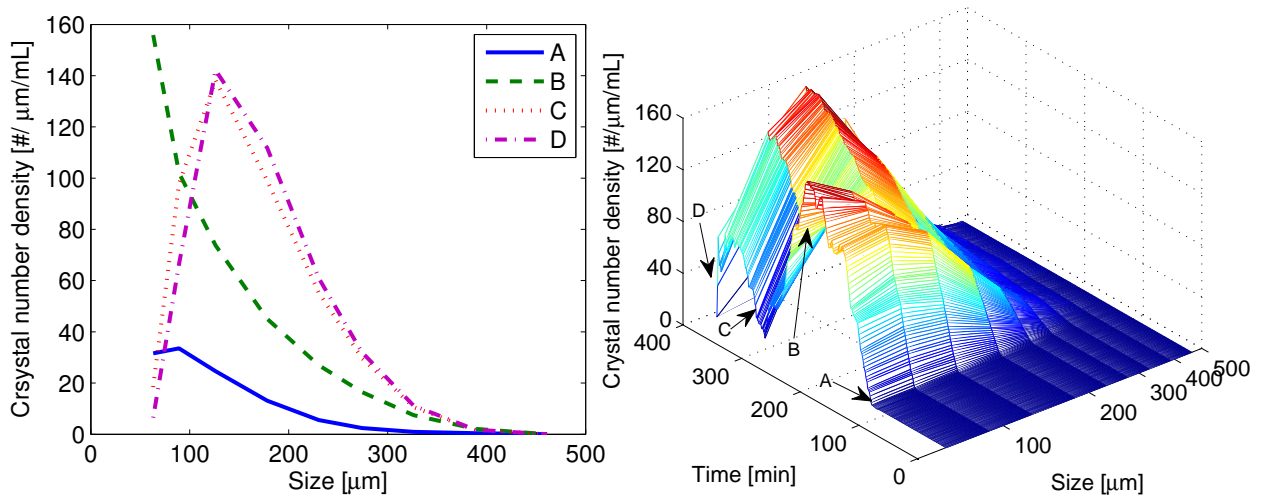
Figure 4.13: Estimated crystal number density of Run I: (a) at A, B, C, and D; (b) evolution of CSD estimates

measured population densities; the shape and magnitude of the density functions are remarkably similar. Moreover, the sieving result estimated the total number of crystals to be 2.72×10^4 per mL and mean size to be 150 μm while values estimated from our model were 2.42×10^4 crystals per mL and 141 μm, respectively.
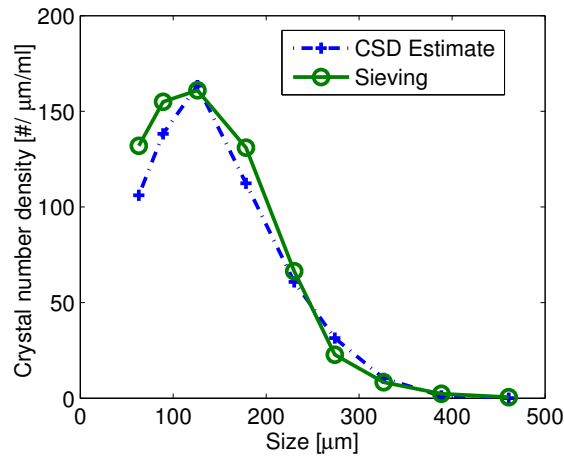
Figure 4.14: Estimated crystal number density and sieving result of Run I

4.4.3.4   Run II: different cooling rate and post-run analysis

The first cooling step from 70°C to 34°C in Run II was reduced by 1/3 that of Run I (0.2°C/min vs. 0.3°C/min), while the initial concentration, instrument settings, and second-stage cooling rate were the same as in Run I. The temperature and supersaturation profiles are shown in Figure 4.15. The rapid decrease in supersaturation at A' (about 42°C) is indicative of primary nucleation; the decrease continued until it became nearly constant. Cooling ended at B', and the supersaturation again began to decrease. The second-stage cooling began at C', and again the supersaturation began to increase until at D' cooling was stopped.

The effects of the post-run analysis are shown in the inset of Figure 4.15. They indicate the solution was saturated at around 350 minutes (i.e. at F'). To confirm this, we added 1.0 gram of paracetamol powder (not crystals as were added in Run I). We chose to add powder in expectation of the greater surface area inducing more rapid consumption of any remaining supersaturation. (Microscopy confirmed the powder was of smaller size and had significantly greater surface area per unit mass.) Nevertheless, the supersaturation ratio did not drop significantly even after this addition. Furthermore, when the temperature was increased by 1.0°C at F', the solute concentration increased slightly while the supersaturation ratio remained constant. From these observations, we conclude that supersaturation indeed reached 1.0, and the ATR-FTIR measurement and solubility model are accurate.

Estimates of the crystal population density at each of the times identified in the previous paragraph were obtained by applying our model to *in situ* measurements of CLD data from Run II shown in Figure 4.16. Crystals started to appear at A', which indicates primary nucleation. The crystal population developed to the CSD estimate of B' at the end of the first-stage cooling. Slight growth occurred in the temperature plateau from B' to C', where large crystals increased and small crystals decreased. The crystals grew significantly in the subsequent cooling stage, as shown

74
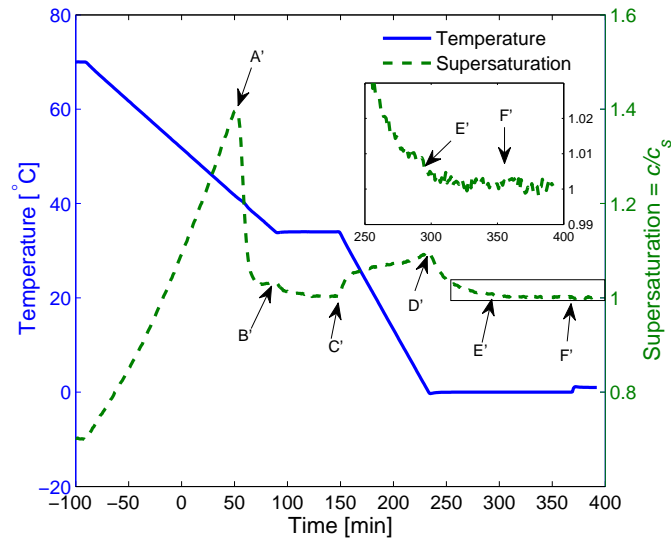
Figure 4.15: The temperature and supersaturation profiles of Run II

in the evolution from C' to E'.

Table 4.2 lists key variables and observations associated with Runs I and II, which
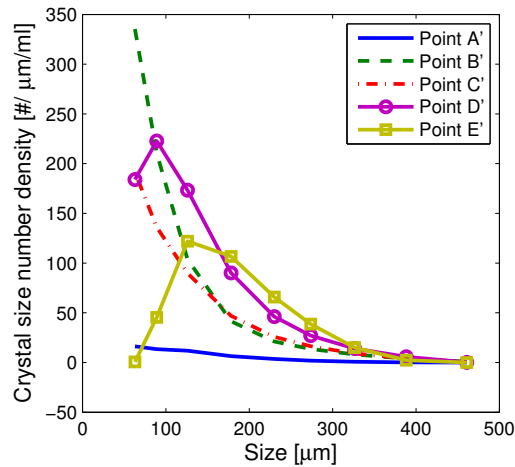
Figure 4.16: Development of CSD number density of Run II

were begun with identical conditions and operated identically, with the exception of the first-stage cooling rate. Run I had a wider metastable zone than Run II (21°C vs.13°C), and thus the supersaturation at primary nucleation in Run I was much higher than in Run II. Higher supersaturation at nucleation usually leads to higher

production of a larger number of crystals, but in these two runs that seems not to have been the case; in other words, comparison of N_1 (the number of crystals per unit volume at B in Figure 4.11 and C' in Figure 4.15) for the two runs shows similar values. Interestingly, nucleation in Run I occurred during the constant-temperature plateau, while in Run II it occurred while the temperature was still decreasing. It is unclear whether these two factors (i.e. higher supersaturation at nucleation and cooling at nucleation) played similar roles in producing similar numbers of crystals.

Starting from the similar CSD, the second stages of the two runs were at the same cooling rate, and the supersaturation ratios for both followed similar patterns, which was shown in Figure 4.11 and 4.15. The maximum supersaturation ratios of 1.10 were achieved at the end of the second-stage cooling in the two runs. If secondary nucleation had been a major factor in either of the runs, the final population density function would be expected to be bimodal. Since that is not the case with either run, as confirmed by our model predictions and sieving at the end of Run I, we conclude that secondary nucleation was a minor factor in determining the final crystal size distribution. Figure 4.17 shows remarkable similarity between population density functions predicted for Runs I and II.

Table 4.2: Comparison between Run I and Run II

Run	dT/dt (°C/min)	T_{nuc}(°C)	ΔT (°C)	S_{nuc}	N_1 (#/mL)	$S_{2,max}$	N_{end} (#/mL)
I	-0.3	34	21	1.55	1.40×10^4	1.10	2.35×10^4
II	-0.2	42	13	1.40	1.47×10^4	1.10	2.19×10^4

dT/dt is the cooling rate in first cooling stage;
T_{nuc} is the temperature when primary nucleation occurred;
$\Delta T = T_{sat} - T_{nuc}$, where T_{sat} is the temperature at which the solution is saturated (S=1);
S_{nuc} is the degree of supersaturation when primary nucleation occurred in first cooling stage;
N_1 is the number of crystals at the end of the temperature plateau;
$S_{2,max}$ is the maximum degree of supersaturation in second cooling stage;
N_{end} is the number of crystals at the end of the crystallization run (D for Run I and E' for Run II).
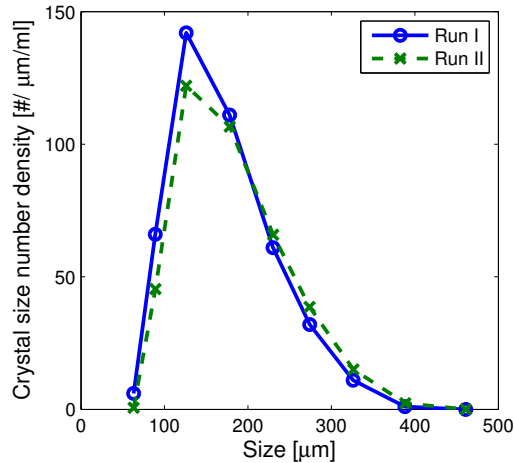
Figure 4.17: The comparison between estimated crystal number density at D in Run I and at E' in Run II

4.5 Discussion

4.5.1 The advantages of the model

The empirical model is simple to construct, and it can be inverted by applying regularized least square minimization. As we showed in our two example runs, the CSD of crystallization processes are well monitored, not only agreeing with our understanding of the crystallization kinetics, but also being consistent with the sieving results. This method is applicable to various crystallization processes, if the crystals have no high aspect ratio and the shape is fixed. For needle-shaped crystals, the method can still be valid but the issue would be finding a way of separating these crystals into different size ranges.

4.5.2 The nature of the FBRM and the empirical model

We create the model based on a simple linear system, which directly relates CSD to CLD from experimental results. Therefore, the model depends on the technique of classifying the crystals with respect to their size. In this study, we used sieving to separate the crystals into nine size ranges and measured the fingerprint CLD

histograms. The fingerprints also revealed the nature of the FBRM—the CLD measurement is dominated by the large crystals. These are two potential error sources of this methodology: (1) the model is a partial observer, which has a limited number of bins covering a limited size range; (2) the ill-conditioning of the model always brings difficulty in estimating small crystals, as we saw the overestimation in Run II when powder were added. The former source is specific to the empirical model, which can be mediated by using more sieve trays. The latter one is a general issue for all kinds of crystals, which requires a tailored algorithm.

4.5.3 Process monitoring and direct control

The crystallization process can be monitored based on the CSD estimates, instead of total chord count of CLD and mean chord length. Without quantified knowledge about the relationship between the CSD and the CLD, it may be ineffective to use the total chord count and the mean chord length as the process indicators. Moreover, this technique can be used in a direct control; the number of crystals, the mean size, and other metrics of the CSD can be estimated to determine the cooling/heating rate without a numerical model of crystallization.

The robustness of the model may be influenced by several factors. The fingerprint model assumes the crystals have a fixed shape, but it neglects possibilities such as polymorph transformation, agglomeration, and breakage. The fingerprint model also assumes linearity. Although not observed in our study, at higher crystal concentrations the linear assumption may not be justified. Furthermore, our model assumes linearity between the CLD and the CSD as confirmed in Figure 4.8, which may not hold at a higher crystal concentration. Nevertheless, as can be seen in Figure 4.14, the proposed model estimated the CSD sufficiently accurately, which may indicate that the above assumptions are valid in our case study.

4.5.4 Parameter estimation and model-based control

With the FBRM and the ATR-FTIR, a full picture is drawn for a crystallization process, including temperature, concentration, and CSD, which are sufficient for estimating crystallization kinetic parameters by the population balance or its reduced model (method of moments), given that our estimates are consistent with sieving analysis. Once the parameters are obtained, we can predict the development of the CSD for a given cooling profile, and thus we can select the optimal profile to meet the requirement of CSD of the final product [99, 148]. Moreover, a model predictive controller can be programmed based on the parameters.

4.6   Conclusion

In this article, an empirical model of FBRM measurements was used to map CLD to CSD. The model is intuitive and simple to build by using characteristic CLD histograms of different sizes of crystals as the fingerprint for crystal size. The FBRM model was then applied to batch cooling crystallization, and our results demonstrated an ability to extract the CSD with the knowledge of the solution concentration. It successfully detected the onset of primary nucleation, secondary nucleation, and crystal growth. The framework developed here can provide the CSD information not only for batch cooling crystallization, but to general solid-liquid processes, where the fingerprint CLD histograms can be obtained. It is a very promising technique for process monitoring, parameter estimation, and control of crystallization.

CHAPTER V

PARAMETER ESTIMATION

5.1 Objective

In previous chapters, unseeded batch cooling crystallization processes are successfully monitor by the empirical FBRM model, with the help from ATR-FTIR and OptiMax. In this chapter, the method is used to extract process measurements from multiple crystallization runs. The data, combined with sieve data on final products, are used for estimation of kinetic parameters in crystal growth and both primary and secondary nucleation.

The work presented in this chapter is reproduced with permission from Industrial & Engineering Chemistry Research, in press. Unpublished work copyright 2015 American Chemical Society.

5.2 Method

5.2.1 Population balance equation and crystallization kinetics

The batch cooling crystallization process can be described by a population balance equation, in which the size of crystals is represented in one dimension and size-independent growth is assumed,

$$\frac{\partial n}{\partial t} + G\frac{\partial n}{\partial x} = 0 \tag{5.1}$$

in which n is the number density [No./μm /kg of solvent], G is the growth rate [μm/min], x is the one-dimensional size of a crystal [μm], and t is the time [min]. Boundary conditions, initial conditions and mass balance are

$$n(t, x = 0) = B/G \tag{5.2}$$

$$n(t = 0, x) = n_0 \tag{5.3}$$

$$c(t) = c_0 - k_v \rho \mu_3(t) \tag{5.4}$$

where B is the nucleation rate [No./min/kg of solvent], n_0 is the initial CSD, c_0 is the initial concentration of the solution, $c(t)$ is the solute concentration, k_v is the shape factor, ρ is the density of crystals, and μ_3 is the third moments of the CSD. For unseeded experiments, n_0 is zero at all sizes.

In this work, three mechanisms are considered for the crystallization kinetics: primary nucleation, secondary nucleation, and crystal growth. CNT was used to describe primary nucleation, in which the net value of volume excess free energy and surface excess free energy is assumed to determine the nucleation rate. [97]. The nucleation model is

$$B_1 = k_{b1} \exp\left(-\frac{16\pi\nu^2}{3k^3} \frac{\sigma^3}{T^3(\ln S)^2}\right) \tag{5.5}$$

in which k_{b1} is a constant [No./min/kg of solvent], ν is the volume of one solute molecule [m^3], k is the Boltzmann constant [m^{2}kg/(s^{2}K)], σ is the crystal-solution interfacial tension [J/m^2], T is the temperature [K], and S is supersaturation ratio (SSR) (c/c_s). In this study, k_{b1} and σ were the parameters to be estimated, T and S were measured during experiments, and ν is approximated by molecular weight and density of the solute crystals.

There are some arguments that CNT may oversimplify the nucleation process, since some dense liquid phase is observed prior to the occurrence of the crystalline nuclei. The dense liquid phase consists of solute molecules appearing as some tiny droplets or spherical particles, which later transform to crystalline structure [25, 59]. According to this theory, the primary nucleation then is divided into two steps. The first step is the formation of the dense liquid phase and the second one is the transformation of the dense liquid phase to crystals. The two-step nucleation was observed in both inorganic [103] and organic [133] systems, but no such report have been published for the system in this study. Moreover, it is difficult to model the two-step

phenomena, since little is known about the transient liquid phase. Therefore, CNT is used to model primary nucleation in this study.

It also may be questioned if the primary nucleation is a homogeneous or heterogeneous process. It is very difficult to guarantee that foreign particles are completely excluded, even if care is taken to provide a clean solution each time the experiment is run. In this study, the mechanism is assumed to remain the same across all the experiments since materials and experimental procedures are consistent. Under this assumption, the surface tension estimated in Equation (5.5) is an effective value representing the combination of homogeneous and heterogeneous nucleation.

For secondary nucleation, since the mechanism is complicated, an empirical form is used.

$$B_2 = k_{b2}(S-1)^\alpha m_s^\beta \tag{5.6}$$

in which k_{b2} is the nucleation constant [No./min/kg of solvent], and m_s is the mass of crystals [g crystal/kg solvent]. The pre-existing crystals create nuclei by shear flow and collisions applied on their surfaces. The crystal mass is assumed to be proportional to the momentum of the crystals, and thus related to the frequency and energy of collision. The effect of agitation is contained in k_{b2}, which is assumed constant in our experiments since stirring speed (mixing intensity) is fixed.

Growth rate is related to temperature and supersaturation.

$$G = k_g \exp\left(-\frac{E_a}{RT}\right) \Delta c^\gamma \tag{5.7}$$

in which k_g is the growth constant [μm/min], E_a is the activation energy to explain temperature dependence [J/mol], and $\Delta c = c - c_s$ [g solute/g solvent] is the supersaturation that drives crystal growth. While the SSR $S = c/c_s$ could alternatively be used as the driving force, Δc is chosen here in order to compare our results with previous studies [140, 92].

5.2.2 Numerical method

Solving the PBE with the kinetics models of Equation (5.5)–(5.7) requires an efficient numerical scheme, especially in a parameter estimation that simulates the process with many different sets of parameters. The CPU time and accuracy of a particular numerical scheme strongly rely on the parameters used in the simulation. For example, a rough discretization of the spatial domain may be acceptable when nucleation and growth occur at modest levels. On the other hand, if the parameters cause high nucleation and growth rates, improper discretization could make the numerical scheme unstable, and thus a fine discretization of the spatial domain is required. Fine discretization generally increases the computational burden. An ideal numerical solution should maintain an acceptable accuracy even with a coarse spatial discretization.

In this work, we used the conservation element/solution element (CE/SE) scheme to solve the PBE. Originally designed for aerodynamic problems, this scheme adopts a staggered way of discretizing spatial domains, and the conservation law of mass is enforced locally and globally[13]. The method was applied to solve partial differential equations in the chemical engineering field, such as simulated moving bed[76, 75] and PBE[95]. In particular, Qamar *et al.*[112] compared CE/SE with finite volume method (FVM) and the finite element method (FEM) for one-dimensional population balance modelling, and concluded that CE/SE has "much better performance as compared to the other schemes". We used this scheme and made several modifications to simulate our cooling experiment, which is coded in MATLAB. One comparison shown in Figure 5.1 is the CSD of the final product in one particular simulation. The reference solution labeled as "limit" is obtained by setting Δx to be sufficiently small; $\Delta x = 1\mu$m in FVM and CE/SE. When Δx is increased to 10 μm, the solution from CE/SE overlays on the reference, whereas the solution of FVM slightly shifts to the right and flattens the peak around 120 μm. Both methods take nearly identical CPU times (less than one second). More details about this scheme and the algorithm can

83

be found in Appendix B.
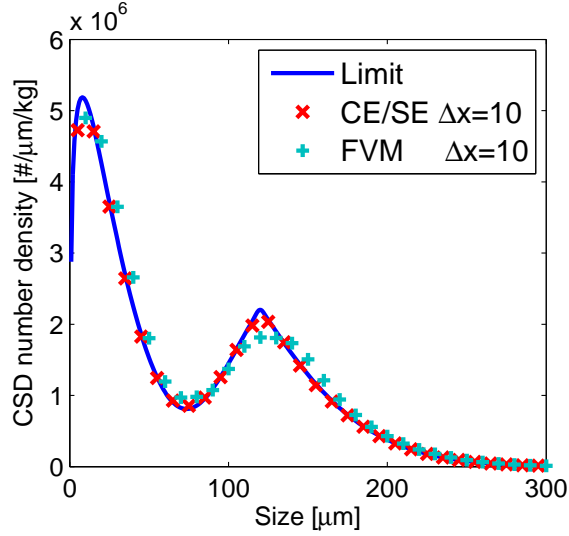
Figure 5.1: Comparison of the solution obtained from CE/SE and FVM

5.2.3 Parameter estimation

If the experimental data are processed and the PBE is solved numerically, kinetic parameters can be estimated by minimizing the error between the measurements and the model predictions. There are four indices needed to define the estimation problem: the type of measurements (using subscripts or superscripts "S" for SSR, "sv" for sieving results, and "F" for CSD estimates from FBRM), the number of experiments (runs) N_r in each type, the number of sample points N_d in each experiment, and the number of measured variables N_m in each sample. The objective function includes errors from SSR, sieving, and the estimated CSD from FBRM.

$$\Phi(\boldsymbol{\theta}) = w_S e_S(\boldsymbol{\theta}) + w_{sv} e_{sv}(\boldsymbol{\theta}) + w_F e_F(\boldsymbol{\theta}) \tag{5.8}$$

where

$$e_S(\boldsymbol{\theta}) = \sum_{i=1}^{N_{r,s}} \sum_{j=1}^{N_{d,i}} \left(\hat{S}_{ij} - S_{ij}\right)^2 \tag{5.9}$$

$$e_{sv}(\boldsymbol{\theta}) = \sum_{i=1}^{N_{r,sv}} \sum_{k=1}^{N_{m,sv}} \left(\hat{n}_{v,ik} - n_{v,ik}\right)^2 \tag{5.10}$$

$$e_F(\boldsymbol{\theta}) = \sum_{i=1}^{N_{r,F}} \sum_{k=1}^{N_{d,F}} \sum_{j=1}^{N_{m,F}} (\hat{n}_{v,ijk} - n_{v,ijk})^2 \tag{5.11}$$

In the equations above, $\boldsymbol{\theta} = \{k_{b1}, \sigma, k_{b2}, \alpha, \beta, k_g, E_a, \gamma\}$ is the parameter set , e_S is the fitting error of SSR, e_{sv} is the fitting error to sieving analysis, e_F for fitting error to volume-weighted CSD estimates from FBRM, w_S, w_{sv}, w_F are the weights for the error terms, the n_v is the volume density of the crystal population. Solutions obtained from the CE/SE scheme are synchronized with experimental data by interpolation in the temporal domain. Since the CSD measurements from sieving or *in situ* CSD estimation only have nine bins, the simulated volume density of the CSD is averaged within the nine size ranges. The sum of the squared errors $\Phi(\boldsymbol{\theta})$ is minimized by *fminsearch* algorithm in MATLAB R2009a, which uses a derivative–free Nelder-Mead method [101].

The confidence region of the parameters is calculated according to Rawlings *et al.* [119]. The confidence region around the estimated parameter $\hat{\boldsymbol{\theta}}$ is estimated by the following quadratic form.

$$(\boldsymbol{\theta} - \hat{\boldsymbol{\theta}})^T V_\theta^{-1} (\boldsymbol{\theta} - \hat{\boldsymbol{\theta}}) \leq \chi^2_{N_p,\alpha} \tag{5.12}$$

in which V_θ is the convariance matrix of θ from different measured variables, $V_\theta = V_\theta^S + V_\theta^{sv} + V_\theta^F$. The sum of squared errors follows a chi-square distribution with degree of freedom N_p and $\alpha = 0.05$ for 95% confidence, where N_p is the number of parameters. For each type of measured variables, the covariance matrix V_θ^q is obtained from the model sensitivity B_q^j and the variance of the measurements V^q.

$$V_\theta^q = \sum_j (B_q^j)^T (V^q)^{-1} B_q^j, \ q \in \{S, sv, F\} \tag{5.13}$$

The variance of measurement V is approximated by the fitting error:

$$V_{ii}^q = \frac{1}{N_{d,q}} \sum_{i=1}^{N_{d,q}} e_{i,q}^2, \ q \in \{S, sv, F\} \tag{5.14}$$

where N_d is the number of sample points considered in the experiments. The matrix B^j represents the sensitivity of the jth sample to parameter set θ, and $B^j \in \mathbb{R}^{N_m \times N_p}$, is usually approximated by finite difference method.

$$B_{k,q}^j \approx \frac{y_{k,q}^j(\hat{\boldsymbol{\theta}} + h_k \mathbf{e_k}) - y_{k,q}^j(\hat{\boldsymbol{\theta}})}{h_k}, \ q \in \{S, sv, F\} \qquad (5.15)$$

in which $k = 1, 2, ..., N_m$ is the ith measured variable, $j = 1, 2, ..., N_d$ is the jth sample points, and $h_k \mathbf{e_k}$ is the perturbation given to $\hat{\boldsymbol{\theta}}$. In this study, $N_m = 1$ for supersaturation, $N_m = 9$ for sieving and *in situ* CSD estimates, and $h_k \mathbf{e_k}$ is 1% variation of each estimated parameter. As a result, $V^S \in \mathbb{R}^{1 \times 1}$, $V^{sv} \in \mathbb{R}^{9 \times 9}$, and $V^F \in \mathbb{R}^{9 \times 9}$.

5.3 Results

5.3.1 Experiments

Three experiments were carried out for parameter estimation, as shown in Table 5.1. The apparatus and materials were as same as used in Chapter 5. The solution of 0.5 L was maintained at 70 °C for one hour, and then cooled to a designated plateau temperature T_{plat} at 0.5 °C/min. This fast cooling rate was selected so that the solution was kept clear before reaching T_{plat}. At some point on the temperature plateau, the reading from the FBRM and the IR changed when nucleation occurred and crystals appeared. The plateau was held for two hours so that the saturation of the solution was depleted, as indicated by the stable and constant signal from the FBRM and IR. Then the second cooling stage began to cool the solution to the final temperature of 0 °C.

Table 5.1 lists the experimental conditions. Considering supersaturation as the most important factor in kinetics, these experiments were designed to vary only T_{plat} to control the SSR at the beginning of the temperature plateau S_{plat}. Other factors that can affect the process, such as cooling rates and total mass of solute, were not

Table 5.1: Conditions of experiments for parameter estimation

Name	Initial concentration [g solute/kg solvent]	1st cooling [°C/min]	T_{plat} [°C]	S_{plat} after 1st cooling	2nd cooling [°C/min]
Run 1			40.0	1.4	
Run 2	370	0.5	43.2	1.3	0.25
Run 3			46.6	1.2	

varied between the runs.

Figure 5.2 summarizes the temperature profiles, the SSR, and the final CSDs of the three experimental runs. In Figure 5.2(a), the temperature profiles of the three runs are shown as a function of time, which are distinguished by T_{plat}. As we can see in Figure 5.2(b), S increased as the solutions were cooled in the first cooling stage (around 60 min). A small spike appeared around the end of the cooling stage, due to slight overcooling in the temperature control. Then the level of SSR were maintained until nucleation occurred. With smaller nucleation and growth rates at lower S_{plat}, it took longer time for the observation of nucleation. The desupersaturation was also slower for a lower S_{plat}. The second cooling stage started around 190 min, when S had stabilized at one in all three runs. When the cooling began, S immediately increased again. Cooling stopped when the final temperature was reached (around 350 min) and S again returned to one.

The final CSDs were influenced by S_{plat}, as indicated in Figure 5.2(c). It can
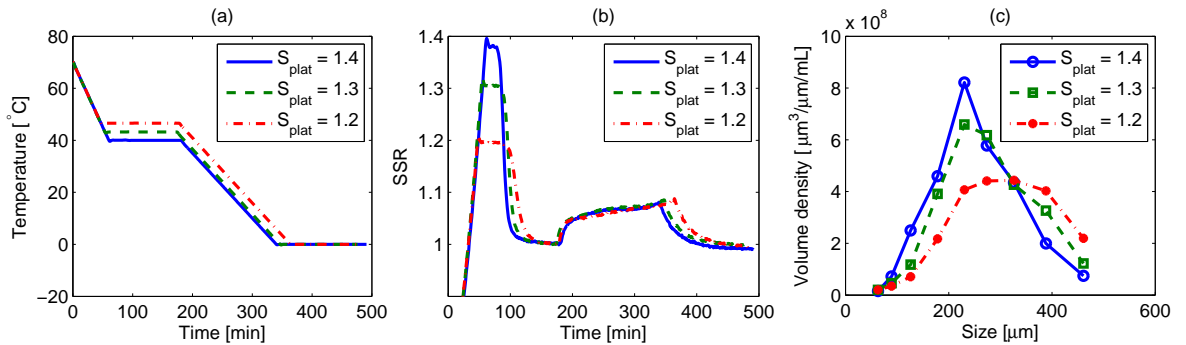
Figure 5.2: (a) temperature profiles in Runs 1 − 3; (b) SSR in Runs 1 − 3; (c) CSD of final product measured by sieving

be seen that the peak locations of the CSDs decreased and the spread of the CSDs became narrower with increase of S_{plat}. Higher S_{plat} led to faster nucleation and growth rates, but nucleation was more sensitive to the change of S_{plat}. Therefore, the supersaturation was more consumed by nucleation when S_{plat} was increased. Started with less crystals created, the second cooling stage allowed each crystals growth to a larger size. This is the reason of Run 3 having the largest mean size. Moreover, the width of the distribution was related with the desuperaturation period at the temperature plateau. Figure 5.2(b) suggests Run 3 had the longest period, so the widest CSD was obtained in Run 3.

The final CLD histogram of the three runs were shown in Figure 5.3. The peak location and the shoulder height between 200–400 μm decreased from Run 1 to Run 3. This trend suggests that Run 3 had more small crystals and less large crystals than the other runs, which apparently conflict with the sieving results shown in Figure 5.2(c). This potential contradiction is analyzed with our CSD estimation technique discussed below.

The CSD estimates of the final product determined from CLD histograms are
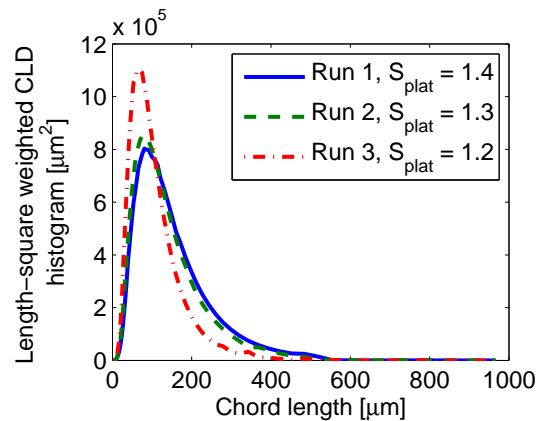
Figure 5.3: CLD of final product in Runs 1–3

compared with sieving in Figure 5.4. The estimated CSDs are in general agreement with the sieved CSDs of Runs 1 and 2, while significant errors can be observed in

Run 3. We attribute this disagreement to the presence of fine particles (smaller than the smallest sieve tray of 53 μm) and large particles (beyond the size of the largest sieve tray of 500 μm). Neither of these size ranges was calibrated in our fingerprint model but they influence the CLD and the CSD estimate. Run 3, in particular, ended with 18% weight of final product greater than 500 μm, violating our assumption that there is no crystals above 500 μm. It probably had the most number of fines as well, because many short-length chords were observed for the final CLD of Run 3 in Figure 5.3. The fines less than 53 μm could be easily altered during washing and drying, and thus they would be difficult to quantify by sieving. However, FBRM may still detect many short chords from the fines and change the CLD, which would be out of the range considered by the fingerprints model. Therefore, only the *in situ* CSD estimates from Runs 1 and 2 were used in parameter estimation, while Run 3 was excluded. We also note the disagreement in Figure 5.4(a) at the largest sizes. While this comprises a significant volume, it is actually a relatively small number of crystals. Parameter estimation was also performed excluding CSD estimates from Run 1, and the estimated values of the parameters were similar.
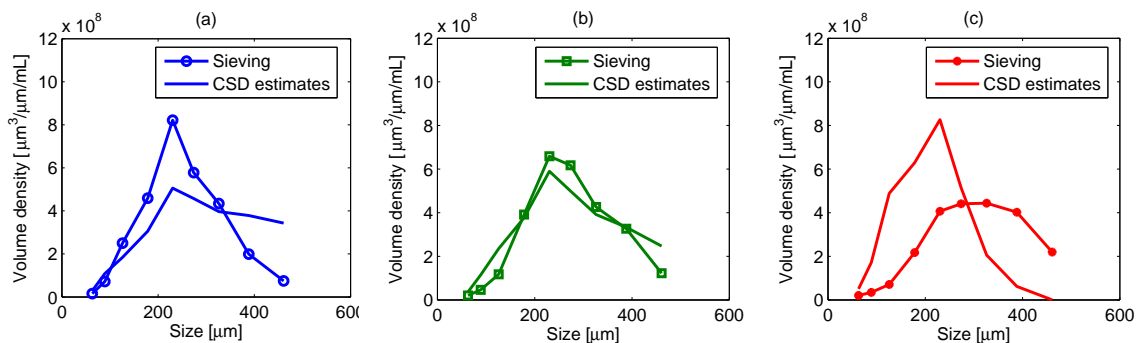
Figure 5.4: The CSD estimates of final product compared with sieving analysis: (a) Run 1; (b) Run 2; (c) Run 3

5.3.2 Parameter estimation

The training set used in parameter estimation contains S and volume density of CSD estimates, from the following data set: $n_S \in \{\text{Run 1, Run 2, Run 3}\}$, $n_{sv} \in \{\text{Run 1, Run 2, Run 3}\}$, and $n_F \in \{\text{Run 1, Run 2}\}$. Weighting of different error sources are selected to be $w_S = 100$, $w_{sv} = 2 \times 10^{-7}$, and $w_F = 5 \times 10^{-11}$.

Table 5.2: Estimated kinetic parameters

k_{b1}	σ	k_{b2}	α	β	k_g	E_a	γ
No./s/kg solvent	mJ/m^2	No./s/kg solvent			(m/s)(g/g)$^\gamma$	kJ/mol	
53.9	4.61	7.44×10^4	1.92	0.714	40.5	40.8	1.28
95% confidence interval obtained by 1% perturbation							
15.8–183	4.25–4.91	(6.64–8.34)×10^4	±0.08	±0.021	39.2–41.9	±0.1	±0.01

In the parameter estimation, $\log k_{b1}$,σ^3,$\log k_{b2}$, and $\ln k_g$ were used in the minimization of the fitting error and the evaluation of the 95% confidence intervals. Since the logarithm and cube are nonlinear transformations, the estimated parameters may not center in their confidence intervals.

Parameters estimated from the experiments are shown in Table 5.2. The estimated value of interfacial tension is 4.61 mJ/m^2, while that estimated by equation from Mersmann [88] is 7.60 mJ/m^2. Other studies on the same system estimated the growth kinetic parameters as $\{10.0 \text{ (m/s)(m}^3/\text{kmol)}^\gamma, 40.6 \text{ kJ/mol}, 1.6\}$ in Mitchell *et al.*[92] and $\{21.0 \text{ (m/s)(m}^3/\text{kmol)}^\gamma, 41.6 \text{ kJ/mol}, 1.9\}$ in Worlitschek and Mazzotti[140]. The growth rate constant in this study is 5.30 (m/s)(m^3/kmol)$^\gamma$ after unit conversion. The activation energy is 40.8 kJ/mol, close to the reported values. The growth exponent γ is usually between 1 to 2, and our estimate is 1.28.

The 95% confidence intervals of the parameters are shown in Table 5.2. Primary nucleation constant k_{b1} varies within one order of magnitude at 95% confidence level, which indicates that the fitting error is relatively insensitive to k_{b1}. Around 10% variation also exists for σ and k_{b2}, while the confidence intervals for the rest of the parameters are narrow.

The predictions of the model are shown in Figures 5.5–5.8. The supersaturation

profiles agree with the experiments well, as shown in Figure 5.5. The optimization program successfully found a single parameter set that can match the onset of nucleation and the subsequent evolution of the SSR in all three runs. The increase of supersaturation during the second cooling stage was also described successfully by this model.

In terms of the final CSD, Figure 5.6 shows that not only each final CSD pre-
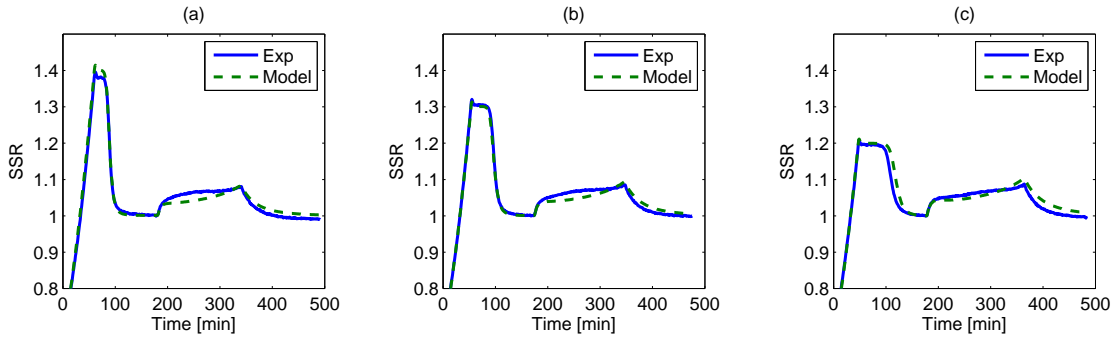
Figure 5.5: Supersaturation-time profile in experiments and simulations: (a) Run 1; (b) Run 2; (c) Run 3

diction is close to its corresponding sieving results, but the model also explains the influence of S_{plat} to final CSD, which is that higher S_{plat} leads to smaller mean sizes and narrower final CSD.

The CSD evolution estimated from the CLD histograms of Runs 1 and 2 and the
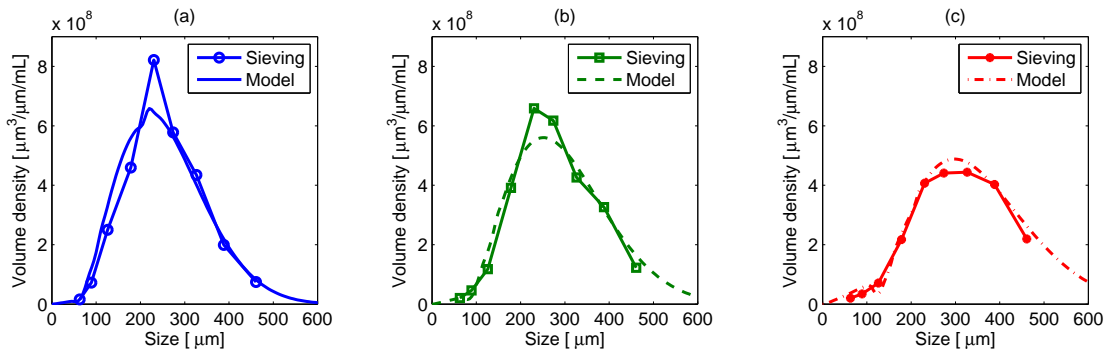
Figure 5.6: Final CSD volume density in experiments and simulations: (a) Run 1; (b) Run 2; (c) Run 3

model predictions are shown in Figures 5.7 and 5.8, respectively. The independent

axes on these three-dimensional plots are crystal size and time, while the volume density is plotted as the dependent variable on the vertical axis. Notice that $t = 0$ corresponds to the beginning of the temperature plateau, since no crystals are generated prior to this time. Both *in situ* CSD estimates and model predictions show two major developments in the CSD volume density. The first rapid change of CSD was around 50 min, corresponding to the initial nucleation and growth on the temperature plateau. The CSD stabilized over the remainder of the plateau, remaining constant until 200 min. Then the second stage started with the second cooling, indicating further crystal growth. Significant secondary nucleation is not observed at the small sizes during this period. The consistency between *in situ* CSD estimates and model predictions suggests the model can accurately describe the changes during the batch cooling process.

The influence of the uncertainty in the parameters is shown in Figure 5.9, by
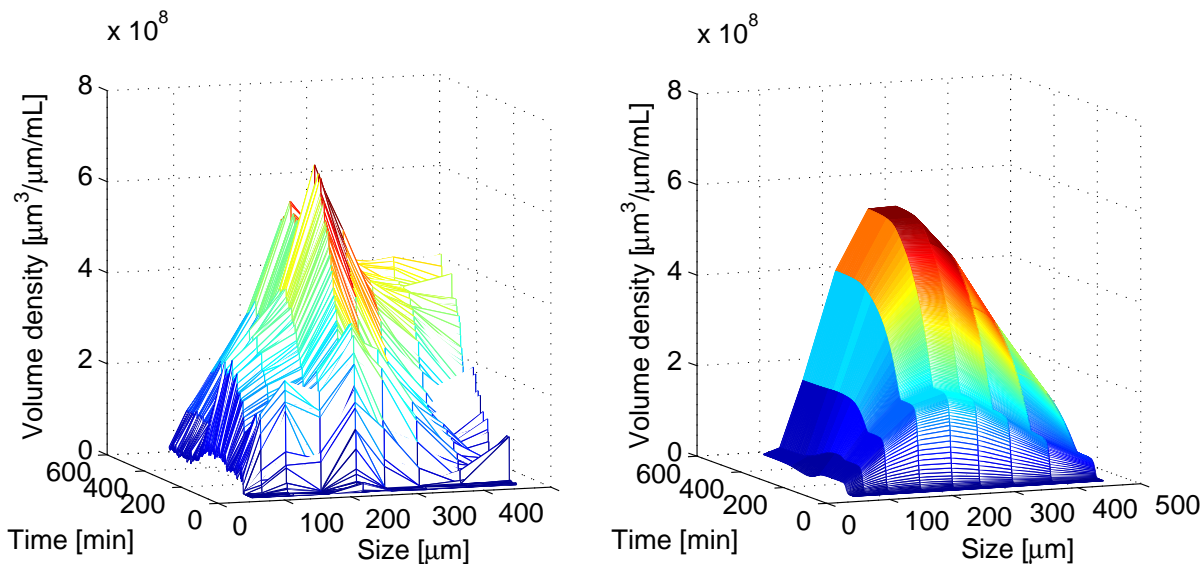
Figure 5.7: Evolution of CSD volume density in Run 1: (a) estimates from CLD; (b) model predictions

simulating Run 2 with parameters randomly sampled from the confidence intervals
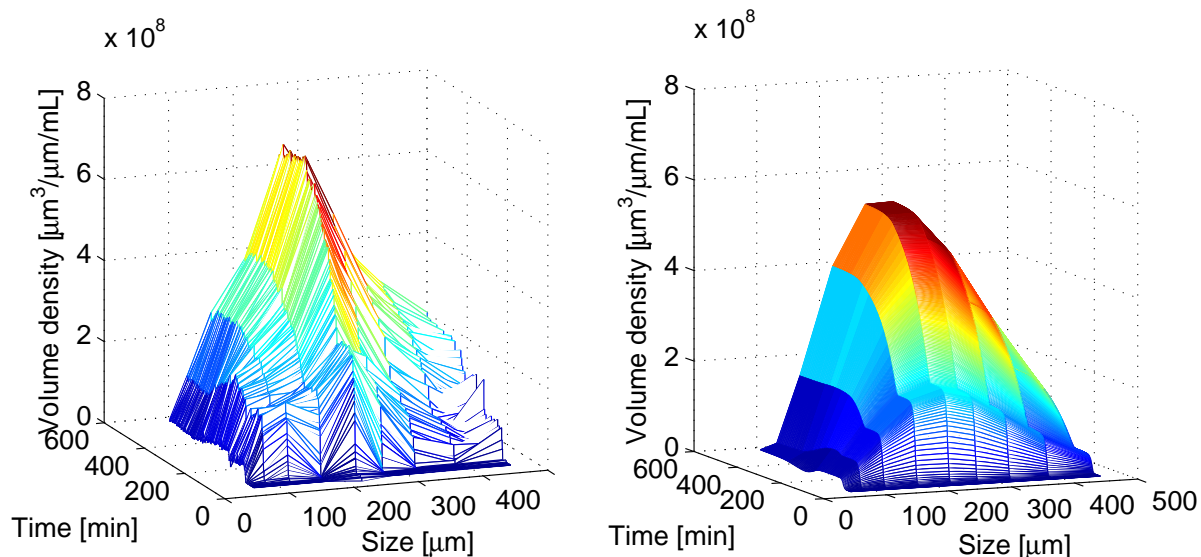
Figure 5.8: Evolution of CSD volume density in Run 2: (a) estimates from CLD; (b) model predictions

in Table 5.2. Assuming the parameters are distributed uniformly in the 95% confidence intervals, 1000 parameter sets have been simulated. The results from 1000 simulations outline the variation caused by the uncertainty of the parameters, and the boundaries of the variation are plotted in Figure 5.9. The predictions in Figure 5.9(a) imply that the onset of nucleation occurs on the temperature plateau for any of the parameter combinations from the confidence region, but the difference can be as large as 13 minutes. The predicted CSD volume density functions in Figure 5.9(b) have a spread of approximately 50 μm in their mean sizes.

An identical experiment to Run 2 was carried out to test the reproducibility of our experiment. The onset of crystallization in the repetition run was observed to be six minutes earlier than that in Run 2, as shown in Figure 5.10(a). The primary nucleation event is expected to be stochastic, so some difference in nucleation time is expected. However, one role of the temperature plateau can be to minimize the impact of this variation for the final CSD. Regardless of the time of nucleation, the crystallization is always driven by a constant S_{plat} so that the CSD remains nearly

unchanged. The sieving analysis in Figure 5.10(b) estimated almost the same final CSD volume density function as the final product of Run 2.
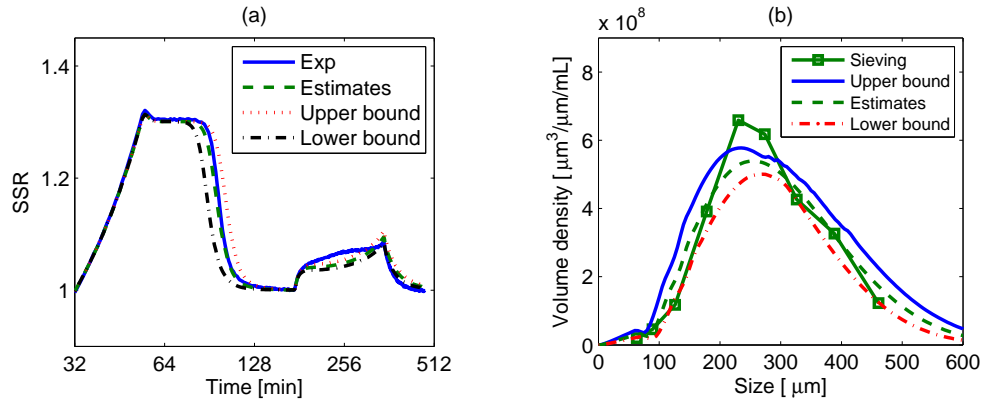
Figure 5.9: Results of 1000 simulations of Run 2. Only the boundaries of the simulated results are shown. (a) SSR; (b) CSD of final product
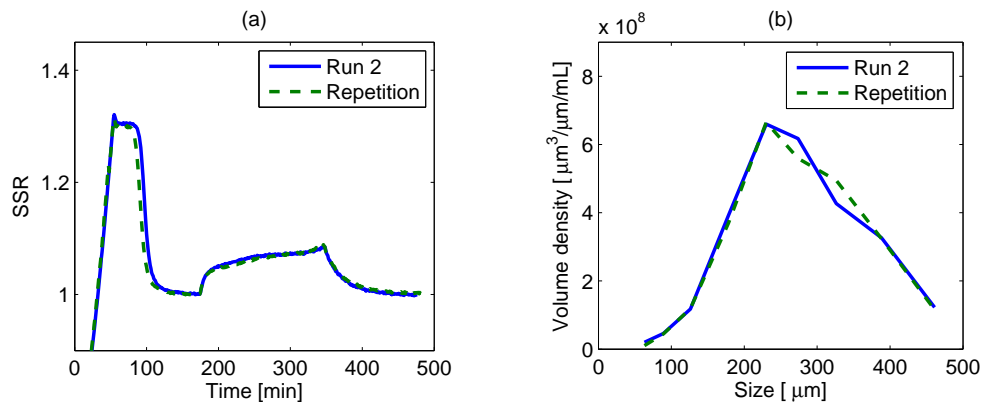
Figure 5.10: Run 2 and its repetition: (a) SSR profile; (b) sieving results

5.3.3 Importance of the FBRM model

The CSD estimated from CLD tracked the change of the CSD during the cooling process, and thus, the CSD information facilitates the parameter estimation. Figure 5.11(a) and (b) show the CSDs obtained from various methods for the end points of the temperature plateau and the cooling process. In the case of Run 1, the difference of the CSD estimated from the FBRM model is not exactly the same as the PBE
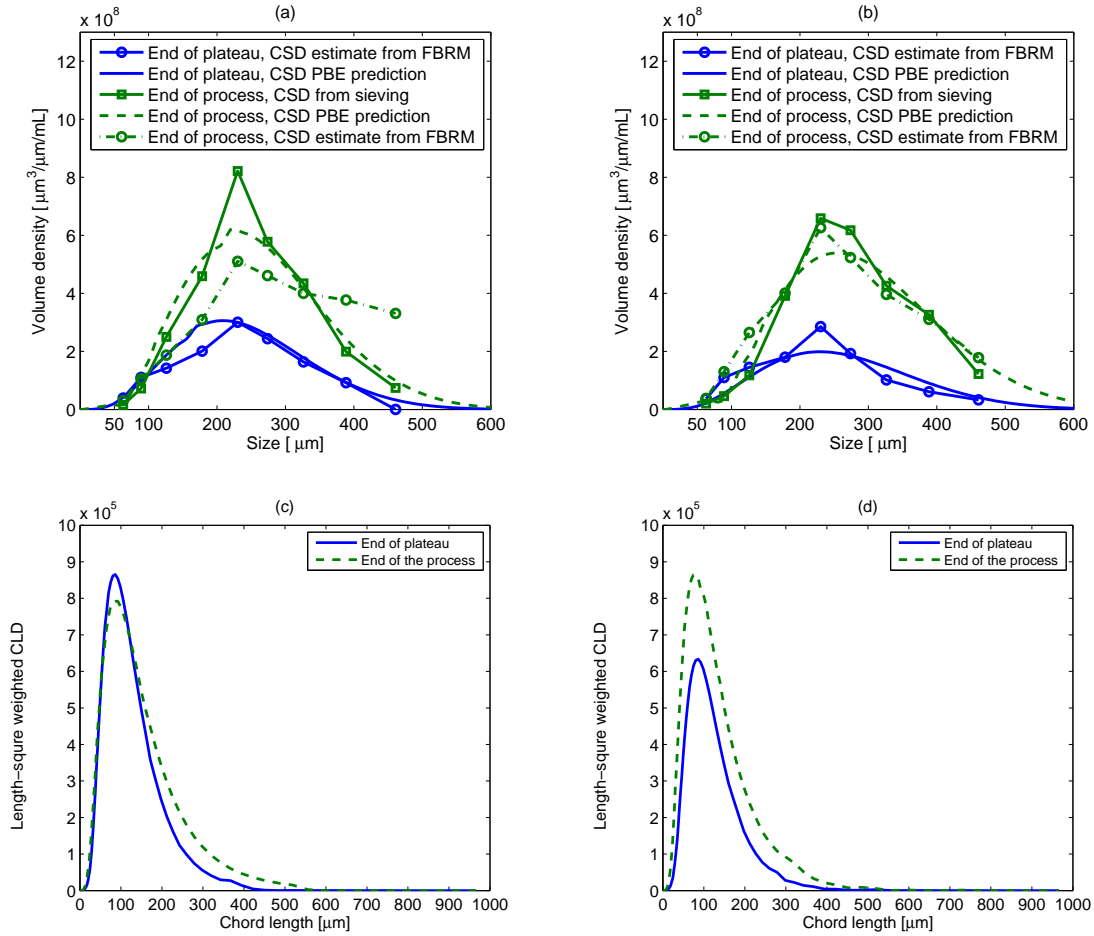
Figure 5.11: *In situ* CSD estimates obtained from the FBRM model at the end of plateau and at the end of the process: (a) Run 1, (b) Run 2. The CLD measured at two corresponding points: (c) Run 1; (d) Run 2.

model prediction, and it also deviates from the sieving result. However, it reflects how the CSD evolves during the second cooling, which helps the search of parameters. In the case of Run 2, Figure 5.11(b) shows good agreements among the FBRM model estimates, the PBE model predictions, and the sieving result. It can be seen that the change of the CSD is well captured by the CSD estimates from the FBRM model. The good fitting of the PBE model to CSD estimates at the end of the temperature plateau also supports the accuracy of the FBRM model.

On the other hands, the change of the CLDs are unable to reflect the CSDs and their change during the cooling processes, as shown in Figure 5.11. For Run 1, the

level of CLD is not changed greatly, except the increase between 200–500 μm. This increase only qualitatively implies the growth of crystals during the second cooling, but it is not comparable to the evolution of CSD shown in Figure 5.11(a). Similarly, CLD increment in Run 2 is about 30%, as shown in Figure 5.11(d), which is unable to describe the growth of crystals shown in Figure 5.11(b).   Without the *in situ* CSD estimates in the parameter estimation, the minimization of fitting error turns into a more challenging task. With less information about the process, the confidence intervals become wider, although the parameter estimates just change slightly, as seen in Table 5.3. To understand the sensitivity of the model predictions to the parameter

Table 5.3: Estimated kinetic parameters without using *in situ* CSD estimates

k_{b1} No./s/kg solvent	σ mJ/m^2	k_{b2} No./s/kg solvent	α	β	k_g (m/s)(g/g)$^\gamma$	E_a kJ/mol	γ
0.192	4.25	$1.00{\times}10^5$	2.08	0.713	45.5	41.3	1.24
95% confidence interval obtained by 1% perturbation							
10^{-9}–10^7	3.59–4.76	$(0.74\text{–}1.36){\times}10^5$	± 0.21	± 0.056	± 1.7	± 0.2	± 0.03

values, the fitting errors were calculated using various combinations of k_{b1} and k_{b2}. Figure 5.12 shows the objective function $\Phi(\boldsymbol{\theta})$ (Equation (5.8)) in the reduced parameter space of k_{b1} and k_{b2}, while all the other parameters are fixed at their optimal values given in Table 5.2. As we can see from Figure 5.12(a), the black L-shaped region suggests the optimization problem is ill-conditioned, because there exist multiple near-optimal solutions for the parameters. The original problem varying eight kinetic parameters could be even more challenging. However, when the *in situ* CSD estimates are available, the L-shaped region transforms into an elongated valley as shown in Figure 5.12(b), where the minimum for k_{b2} is easier to locate. The black regions in both (a) and (b) imply that the error function is insensitive to the value of k_{b1}, and thus its confidence interval is wider than k_{b2} as seen in Table 5.2.

Corresponding to the case in Figure 5.12(a), Table 5.3 gives the values of the
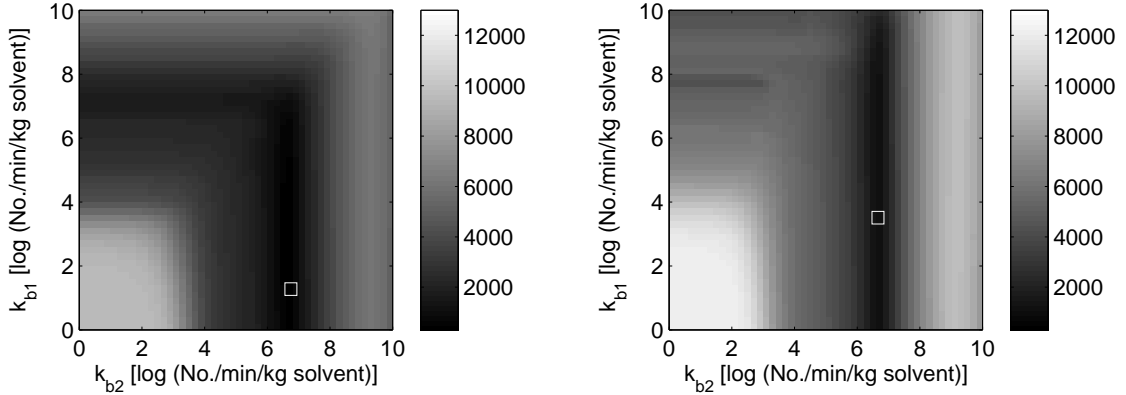
Figure 5.12: Error landscape as a function of k_{b1} and k_{b2}: (a) without *in situ* CSD estimates; (b) with *in situ* CSD estimates of Run 1 and 2; White squares indicate the locations of the optimal solutions

parameter estimates and their confidence intervals. The values of the estimated parameters are similar but with wider confidence intervals, compared to Table 5.2. Notice that the confidence interval of k_{b1} is relatively wide in both cases. This can be explained by the vertical black regions in Figure 5.12(a) and (b), indicating that the error function is insensitive to the value of k_{b1}.

5.3.4 Model verification

Additional unseeded and seeded runs were implemented to test the capability and limitation of our PBE model. The details of experiments are shown in Table 5.4. The SSR profiles and final CSDs (number density) are compared in Figures 5.13 and 5.14.

First, we tested the model at a different second cooling rate. The experimental condition in Run 4 was the same as in Run 2, except that the second cooling rate was doubled. Therefore, it was expected that the supersaturation should increase to a higher level in second cooling stage, compared to Run 2. As shown in Figure 5.13(a), the value of SSR at the end of the second cooling reached around 1.2, compared with 1.1 in Run 2 (Figure 5.2(b)). Notice that there was a sudden drop of the measured SSR at 315 min, possibly due to an accidental move of the optical

Table 5.4: Experimental conditions for the validation experiments

Name	Seeds mass [g]	Initial concentration [g solute/kg solvent]	1st cooling [°C/min]	T_{plat} [°C]	S_{plat}	2nd cooling [°C/min]
Run 4	0	370	0.5	43.2	1.3	<u>0.5</u>
Run 5	<u>0.03</u>	370	0.5	48.0	1.16	0.25
Run 6	0	<u>405</u>	0.5	50.0	1.2	0.4
Run 7	0	370	0.5	43.2	1.3	<u>0.1</u>

Underlined values indicate the major difference between the validation experiments and the experiments for parameter estimation.

fiber of ATR-FTIR. It happened after the second cooling stage and had not affect to any previous SSR measurements. Our model correctly predicts the SSR profile, as shown in Figure 5.13(a). The final CSD shown in Figure 5.14(a) is consistent with sieving results for large size (greater than 200 μm). The peak of CSD is predicted at 115 μm, whereas the sieving result suggests a flat-top. This difference could be associated with the incapability of sieving in measuring the number density.

We also tested the model for a seeded crystallization process in Run 5. Because crystals are initially present, secondary nucleation is expected to be more significant than primary nucleation. Before 0.03 g of seedes between 75 to 106 μm were introduced, the solution was cooled to the designated plateau temperature. The average number density is roughly around 10/mum/mL. Figure 5.13(b) shows significant discrepancies between the SSR measurements and predictions. One reason could be that the initial CSD of seeds provided to the simulation was inaccurate. The actual seeds could contain fines adhering to their surfaces, known as initial breeding [29]. The seeds might also acquire some surface features in seeds preparation [1], such as washing, drying, and milling, which could affect the secondary nucleation and growth rates. This unmodeled effect made the predicted SSR decrease more slowly on the temperature plateau and increase to higher values in the secondary cooling stage, compared to the experimental observation in Figure 5.13(b). In Figure 5.14(b) for final CSD comparison, the predicted number density at 178 μm is lower than sieve
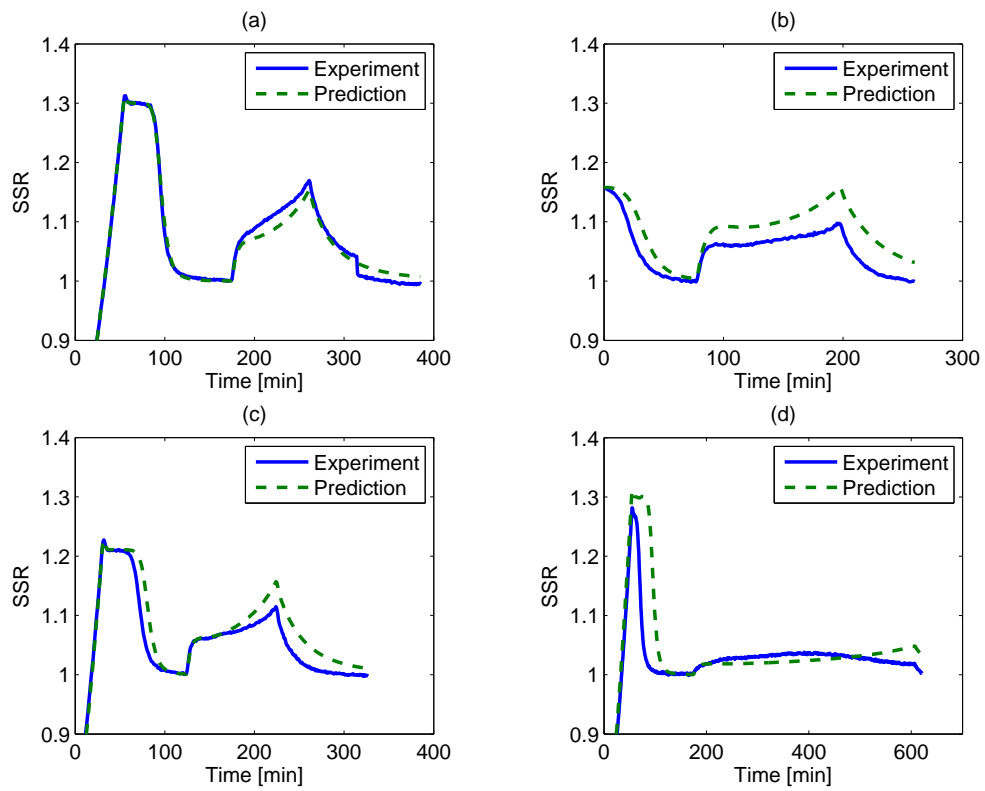
Figure 5.13: SSR profiles of validation runs: (a) Run 4; (b) Run 5; (c) Run 6; (d) Run 7

analysis, which may be caused by the unconsidered factors of the seeds and their effects on kinetics.

Some factors and kinetics that are neglected in the model can be important when
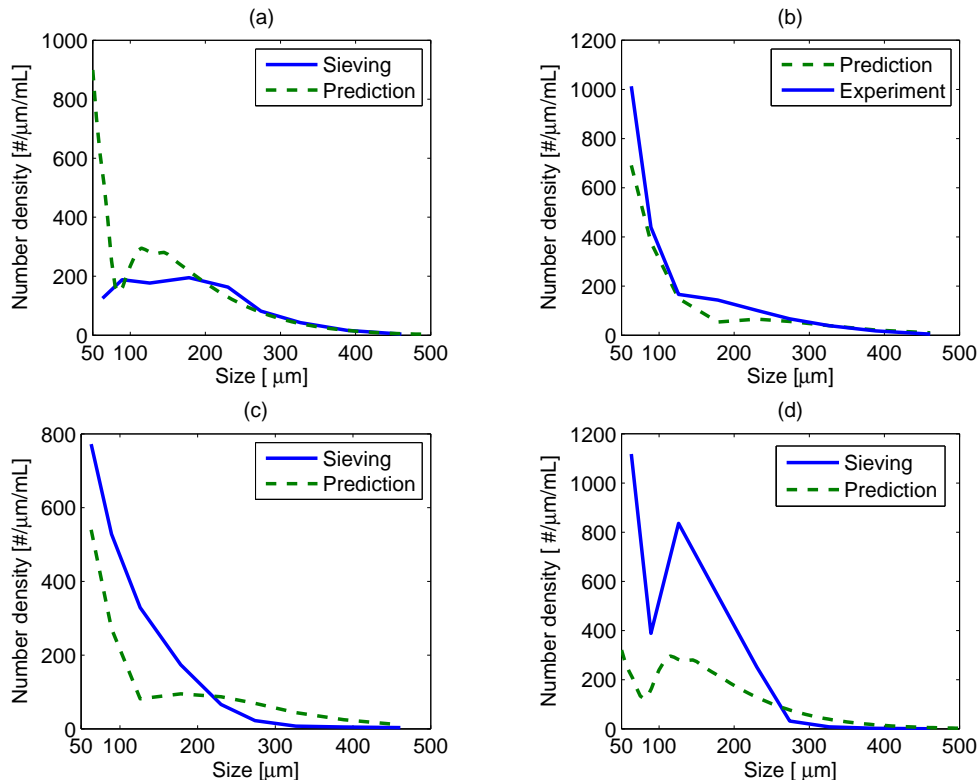
Figure 5.14: Predicted final CSD in comparison with sieving results: (a) Run 4; (b) Run 5; (c) Run 6; (d) Run 7

the experimental conditions are changed significantly, as demonstrated by Runs 6 and 7. Run 6 started with an initial concentration that is 10% higher than used in Runs 1–3. The solution was cooled to 50 °C to achieve $S_{\text{plat}} = 1.2$. The SSR profiles agrees, as shown in Figure 5.13, except there is some deviation in the second cooling stage. The CSD comparison in Figure 5.14(c) shows that the prediction is on the similar order of magnitude of the sieving results, but more small crystals (up to 200 μm) and less large crystals (200 μm above) were obtained from the experiment, which may be caused by some neglected kinetics in the model, such as growth rate dispersion, size-dependent growth, or by the change of the interfacial tension at this concentration

and temperature.

In Run 7, a much lower second cooling rate was used, which prolonged the second cooling stage. Figure 5.13(d) shows the SSR profile, in which the second cooling stage started at 180 min and finished at 600 min. The measured SSR increased at the beginning of the second cooling plateau and started to drop in the middle of the stage. However, the model predicted a monotonic increase of SSR. Figure 5.14(d) indicates that more small crystals and less large crystals were obtained in the experiment, compared to the model prediction. The mismatches in both SSR and CSD might be caused by additional mechanisms. For example, attrition was apparently the reason for more crystals below 200 μm. Attritions is the abrasion exerted to crystals that lead to rounded vertices and edges of the crystals. The fragments stripped off the mother crystals can act as newly-formed crystals. The SSRs during second cooling stage of Run 7 are around 1.05, only 1/4 to 1/2 as in other runs (1.1–1.2), according to both experimental and simulation results. Our speculation is that attrition became more dominant to the process, when growth rate was low at low SSR. It created many small crystals at the expense of large ones, which made the final CSD different from the model prediction.

5.3.5 Analysis of crystallization kinetics

5.3.5.1 Nucleation

Given the good performance of the model within the experimental conditions of the training set, the model can provide a mechanistic interpretation of the crystallization process. Figure 5.15 compares the total number of nuclei and the number of nuclei generated by primary nucleation. The difference between the two quantities is the number of nuclei generated by secondary mechanism. Both coordinates are in logarithmic scale to show the wide variations of the values. In the experiment, it is not possible to separately measure the rates of primary and secondary nucleation, but

101

the model provides this information.

As can be seen from Figure 5.15(a)–(c), more and more primary nuclei are generated during cooling, but there is no secondary nucleation. When there are enough amount of crystals present in the solution, secondary nucleation starts and creates a significant number of nuclei, which lead to the outburst of nucleation, as observed on the temperature plateau. Then the total number of nuclei levels off until 200 min, when second cooling is started. During this cooling stage, the total number of nuclei increases but the the number of primary nuclei remains constant, as seen in Figure 5.15, indicating no primary nucleation and significant secondary nucleation.

The simulation results indicate that the role of primary nucleation, under the
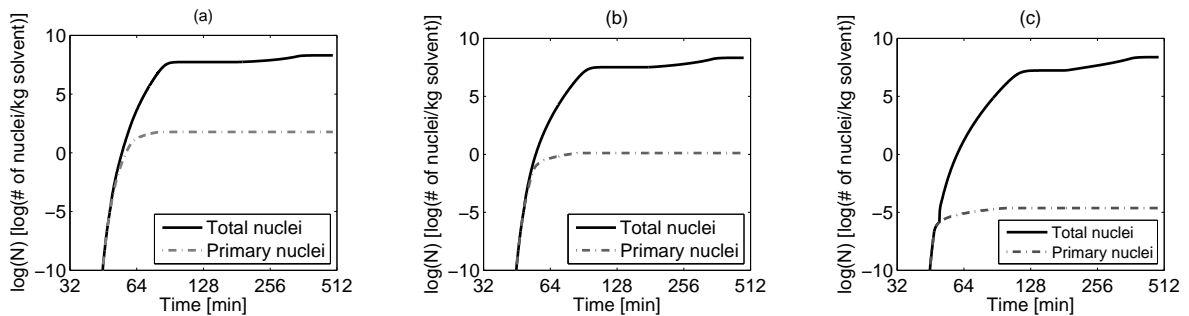
Figure 5.15: Predicted primary and secondary nucleation rates: (a) Run 1 ($S_{plat} = 1.4$); (b) Run 2 ($S_{plat} = 1.3$); (c) Run 3 ($S_{plat} = 1.2$). The time and nucleation rates are shown in logarithmic scales

given supersaturation ratios, is to generate a few nuclei. The primary nucleation event triggers secondary nucleation, which creates almost the entire crystal population. This phenomenon is analogous to an autocatalytic reaction, with dissolved molecules as the reactant and crystalline solid as the product. Crystals catalyze further production by the secondary nucleation mechanism, leading to exponential growth in the number of crystals. As the crystals grow in size, the solute in solution is consumed, and this causes both nucleation and growth to slow down.

5.3.5.2   Growth

With low S_{plat}, significant crystal growth occurs during second cooling, according to the simulated CSDs shown in Figure 5.16. At the end of the temperature plateau, the CSDs has the similar peak sizes at around 50 μm, but their heights are different, as shown in Figure 5.16(a). The heights of the CSDs are proportional to S_{plat}. In the subsequent cooling stage, the CSDs lead to different growth and nucleation rates. As a result, Run 1, with the most crystal mass and surface area, has the least crystal growth and the peak of the CSD moves around 50 μm, as shown in Figure 5.16(b). The growth rates are compared in Figure 5.16(c), using Equation (5.7). At the beginning of the temperature plateau, growth rate is at maximum, which dropped fast once crystallization starts. In the second cooling stage started around 170 min (see the inset figure), Run 3 has the strongest crystal growth, so the peak shifts from 50 μm to 175 μm. Notice that the final CSD of Runs 1–3 are all bimodal, as shown in Figure 5.16(b), while the significance of the small-sized mode vary with S_{plat}. As indicated by the simulated final CSD, Run 3 has a lot more crystals than Runs 1 and 2, which may caused the inaccurate CSD estimates in Run 3.
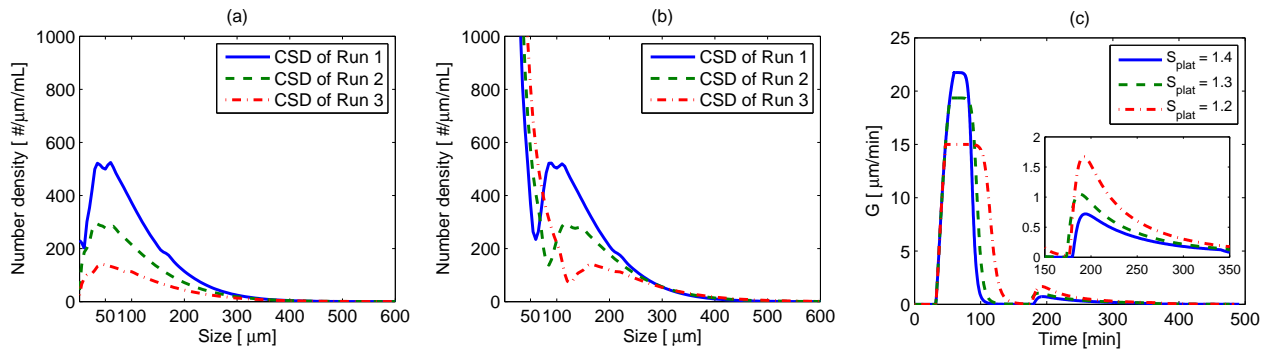
Figure 5.16: (a) the CSD at the end of temperature plateau; (b) the CSD of end product; (c) growth rates during experiments
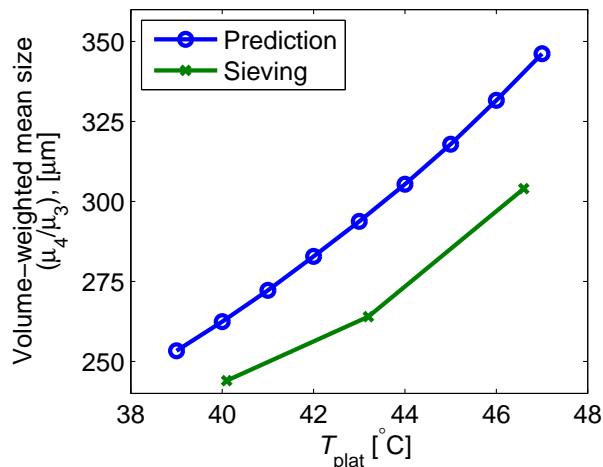
Figure 5.17: The effect of T_{plat} on the volume-weighted mean size

5.3.5.3 Final product from different T_{plat}

The mean size of the volume-weighted final CSD is shown to be decreasing with T_{plat}, as shown in Figure 5.17. Nine two-stage unseeded crystallization runs are simulated with different T_{plat}. The curve obtained from simulation indicates an increase of mean size with T_{plat}, which is consistent with our observation from Runs 1–3. The mean size of CSD from sieving is determined about 30 μm lower than the predicted curve, but the trend is similar to the simulation results. These results imply a potential of the two-stage cooling strategy to achieve a desirable mean size of the final product, by selecting a proper plateau temperature for the initial crystallization in an unseeded process.

5.4 Discussion

Our empirical FBRM model transforms CLD measurements into a partial observer of the CSD, to estimate number of crystals only between 53–500 μm. These partial *in situ* CSD measurements, when combined with other measurements and a proper simulation method, can be used to provide *in situ* information and estimate kinetic parameters. The limitation of the FBRM model is also identified: it gives inaccurate

104

estimates when too many crystals out of the 53–500 μm range. This is the reason for excluding FBRM data of Run 3, and the limitation should also call for attention in future use of the model.

The mechanistic interpretation from the kinetic parameters suggests that the primary nucleation rate is much lower than the secondary nucleation rate. This statement is may be in conflict with the consensus in the crystallization community that primary nucleation is the dominant mechanism for generating crystals. However, a similar observation was reported recently by Kadam *et al.* [53, 54], in which one or very few large crystals appeared in an unseeded stirred volume, prior to the massive nucleation event. It is also consistent with the chiral symmetry breaking observed in the unseeded crystallization of sodium chlorate [61]. The secondary nucleation parameters were estimated by Worlitschek and Mazzotti[140] in their seeded study of paracetamol-ethanol crystallization, but the equation was in a different form. Using their parameters and expressions, the average secondary nucleation rate is around 10^7 /min/(kg solvent), while the nucleation rate is 10^5–10^7 /min/(kg solvent) in our work. The consistency supports the accuracy of our estimation.

Our results also provide a mechanistic interpretation of the induction time seen in experiments. The simulation results in Figure 5.15 explain the delay between the time of supersaturation and the observable crystallization. The secondary nucleation requires a certain time to induce enough nuclei that can decrease the supersaturation. In the induction period, the number of nuclei and their size developed slow until they surpass a threshold that can decrease the supersaturation.

Using a temperature plateau to induce nucleation could be a candidate for internal seeding strategies. Internal seeding is usually achieved by continuous cooling, with linearly or certain cooling strategies, until nuclei are detected. The solution may be cooled to an undesired supersaturation which results in too many fine crystals, so

105

further operations are required to dissolve or remove the fines. If the two-step cooling is implemented with a proper plateau temperature, CSD created by the initial nucleation is controllable, and the consistency is greatly improved, as shown by Run 2 and its repetition in Figure 5.10.

5.5   Conclusion

The experimental and numerical approaches are presented for estimating crystallization kinetics in unseeded processes, using *in situ* and *ex situ* process measurements and population balance modeling. Unique approaches have been demonstrated in our case study, including (i) the use of CSD obtained from FBRM; (ii) simultaneous estimation of primary nucleation, secondary nucleation, and crystal growth by unseeded cooling processes; (iii) proper choice of PBE solver that can perform process simulation and error minimization.

CSD and S from unseeded two-stage cooling experiments are used to decouple primary nucleation, secondary nucleation, and growth. This cooling profile has its advantages over the linear cooling profile. The crystallization process can be divided into two stages. Initial crystallization on the temperature plateau involves all three kinetics. Primary nucleation and crystal growth determine the induction time and the desupersaturation curve. Secondary nucleation may participate as well, while our results show its importance in the initial crystallization. The second cooling stage, starting with the crystal population created on the temperature plateau, can be viewed as a seeded run, which excludes primary nucleation. The reproducibility of the CSD is enhanced by initiating nucleation at a controlled supersaturation, and the influence of the random nature of primary nucleation is diminished. Predictivity and the limitation of the model were shown by verification runs.

FBRM provides critical process information, which helps in resolving the kinetic parameters. The FBRM model was an established empirical mapping between CLD

and CSD from our earlier studies. It was applied to the first two experimental runs, while the third one is not as good, since its CSD strongly violates our assumption for the FBRM model. The *in situ* CSD information makes the optimal solution to the parameter estimation problem easier to locate. It also narrows the confidence intervals of the estimated values.

Interpretation of the kinetics suggests that crystal growth and nucleation are competing mechanisms. More solute is consumed by crystal growth at low SSR, which leads to a flatter CSD with greater mean size, compared with the case at high SSR. The interpretation also shows that, in paracetamol crystallization at the investigated SSR, primary nucleation generate far less crystals than secondary nucleation, even during the initial crystallization event at temperature plateau.

CHAPTER VI

CONCLUSIONS AND RECOMMENDATIONS

6.1 Conclusions

The thesis presents an empirical FBRM model that estimates crystal population density from chord length distribution and its application to determine crystallization kinetics parameters.

The use of a linear, data-driven model provides a simple but effective approach to correlate CSDs with CLDs, compared to the complicated Monte Carlo simulation associated with first-principle models. The empirical model treats the size of the crystal as the only factor that determines the CLD and neglects other factors. Paracetamol crystals were sieved into different size fractions, and the characteristic CLDs (fingerprints) from each size fraction were determined in the nonsolvent toluene. Additivity and linearity of the empirical model were verified experimentally. The fingerprints confirm some qualitative uses of the FBRM, such as the correlation between the mean size of crystals and mean chord length. However, it also reveals that a large crystal generates more chords than a small crystal, which indicates that the mapping between CSDs and CLDs is ill-conditioned.

For the ill-conditioned model, two inversion techniques have been developed for estimation of CSDs from CLDs, using regularized least squares minimization and principle component regression, respectively. It has been found that both of the methods are able to estimate CSD accurately when the CSD is unimodal, while there are some inaccuracy for a bimodal CSD, due to the ill-conditioning.

The empirical model for a practical crystallization system was then established with paracetamol crystals and its saturated ethanolic solution. The fingerprint CLDs

suggested a similar trend as obtained from paracetamol-toluene system, and the regularized least squares methods was adopted to estimate the CSD. In addition to the information from the FBRM, the infrared spectra of the solution from ATR-FTIR were calibrated at different temperatures and concentrations, and a polynomial calibration model was constructed. The CSD estimated from FBRM was corrected by the liquid information to ensure mass balance. In other words, the CLD provides the shape of the CSD, and the mass balance of paracetamol determines the total mass of the crystals. A framework has been established to extract both CSD and solute concentration from the *in situ* CLD and IR measurements. Notice that the CSD estimates are between 53–500 μm.

Two unseeded runs have been successfully examined by the framework. The CSD estimates show the advantages of the empirical model over the use of the total chord count and mean length from the CLD. The case study shows that the total chord count used as an indicator for nucleation may be misleading, since chord count also increases when the crystals become larger. It is also shown that the mean size of CSD estimates are more responsive to process operations (for instance, cooling) than mean chord length. The CSD estimates of the final product are verified with sieve analysis.

With the framework for monitoring CSD and concentration, crystallization kinetics parameters (primary nucleation, secondary nucleation, and crystal growth) were estimated based on three unseeded two-step cooling runs. The two-step cooling profile is advantageous over the linear cooling profile: initial crystallization is fixed at a predetermined supersaturation regardless of the length of the induction period. For the initial nucleation on the temperature plateau, primary nucleation and crystal growth determine the desupersaturation curve and the CSD; secondary nucleation may participate as well, when there is a sufficient amount of crystals present. The second cooling stage, starting with the crystal population created on the temperature plateau, can be viewed as a seeded run without primary nucleation.

With initial crystallization induced at different supersaturation, the influence of supersaturation was distinctly reflected in the CSD and supersaturation measurements. CSD estimates from FBRM, supersaturation, and sieving results were included for the parameter estimation and they were fitted with the solution of the PBE. The differences in experimental data were successfully fitted and explained with our kinetic models and their parameters.

FBRM and the empirical model provide critical process information, which help in resolving the kinetic parameters. The FBRM model was applied to two of three experimental runs, while the third one is not as useful because of its bimodal CSD. The *in situ* CSD information makes the optimal solution of the parameter estimation problem easier to locate. It also narrows the confidence intervals of the estimated values.

Interpretation of the kinetics suggests that crystal growth and nucleation are competing mechanisms. More solute is consumed by crystal growth with low S_{plat}, which leads to a flatter CSD with greater mean size. The interpretation also shows that, in paracetamol crystallization at the investigated conditions, primary nucleation generates far fewer crystals than secondary nucleation, even during the initial crystallization event on the temperature plateau.

Meanwhile, some drawbacks of the FBRM model and the crystallization kinetics are also identified. The first drawback is that the FBRM model largely relies on the sieving. If crystals are in some shapes that are difficult for sieve analysis, such as plates or needles, the efficiency of sieving may limit the applicability of the empirical model.

Another drawback is that the FBRM model gives inaccurate estimates when the CSD is bimodal in the size range of 53–500 μm or too many crystals are outside that range. The experimental results have shown several unsuccessful cases and the reason for the disagreement are explained.

The third defect is the simplification of crystallization kinetics, which only includes primary nucleation, secondary nucleation, and crystal growth. The mathematical expressions are descriptive to some extent, but they are still empirical or lack of necessary detail. As a result, the kinetics in the model are able to describe the observations in the training experiments. However, in a much broader experimental range, it was found that these expressions were inadequate to predict the outcome of the crystallization process.

In summary, the thesis has thoroughly discussed the quantification of FBRM data for CSD estimates. The empirical model of FBRM has been shown to be effective for both a nonsolvent system and a practical crystallization case. The CSD estimated from FBRM has been found to provide rich information throughout the process and can be of great help in estimation of kinetic parameters.

6.2 Recommendations

6.2.1 New approach of determining the empirical model

As stated above, when the crystals are in plate-like or needle-like shapes, sieving is unable to separate the crystal efficiently, and therefore, re-dispersing the crystals obtained from sieving is impractical for the determination of the fingerprints. One alternative is using other sizing techniques to calibrate the FBRM and build the fingerprint model.

Suppose CSD samples $\mathbf{x}_i$, $i = 1, ..., n$ are available, and $\mathbf{x}_i$ are determined by off-line methods (e.g., laser diffraction). Meanwhile, the corresponding CLD $\mathbf{b}_i$ are also known from FBRM measurements. There exists a mapping between $\mathbf{x}_i$ and $\mathbf{b}_i$. The mapping can be implicitly used. For example, a new CLD $\mathbf{b}^{\text{new}}$ is measured for unknown sample $\mathbf{x}^{\text{new}}$. Assuming $\mathbf{b}^{\text{new}}$ is a linear combination of $\mathbf{b}_i$ (suppose n is sufficiently large), i.e. $\mathbf{b}^{\text{new}} = \sum_i k_i \mathbf{b}_i$. Meanwhile, CSD should follow the exact linear combination, which is $\mathbf{x}^{\text{new}} = \sum_i k_i \mathbf{x}_i$. An alternative method is using some

advanced methods to explicitly correlate $\mathbf{x}_i$ and $\mathbf{b}_i$, such as regression methods or neural network. Then $\mathbf{x}^{\text{new}}$ can be estimated from $\mathbf{b}^{\text{new}}$ with the explicit model.

Another advantage of the new approach is that it requires no experiments of re-dispersing the crystals to saturated solutions. The data can be provided by crystallization runs. These runs are performed with distinct operating conditions in order to produce different CSDs. The final CSDs are measured with some off-line methods and correlated to the CLDs. Once enough $\mathbf{x}_i$ and $\mathbf{b}_i$ are collected, CLDs can be directly used to analyze the crystallization runs for further evaluation. This method consumes less time and can broaden the size limit, instead of the 53–500 μm range of sieving.

6.2.2 Primary and secondary nucleation

From the interpretation of the crystallization kinetics, it is found that primary nucleation generates much fewer nuclei than secondary nucleation in unseeded processes, which may disagrees with the consensus in the crystallization community. The hypothesis is that only a few nuclei are generated from primary nucleation, and they are used as templates for secondary nucleation to generate the rest of the crystals. More experiments can be carried out to examine the hypothesis.

- Cool an unsaturated solution to a designated plateau temperature, measure the induction time and the CSD after the initial crystallization. Secondary nucleation should affect the induction time and the CSD, if it generates the majority of the crystals. To prove this, different stirring speeds can be used in order to change the secondary nucleation rate. However, growth rate also depends on mixing. Therefore, two sequences that manipulating the stirring speed are design in Figure 6.1. Sequence A switches the stirring speed from nominal value
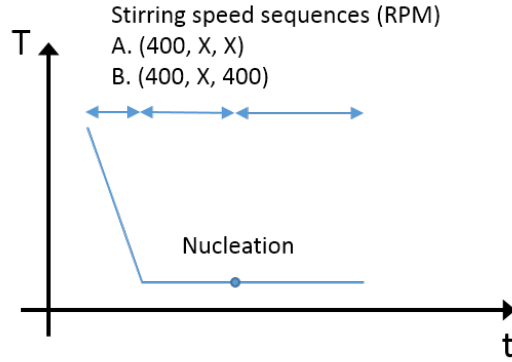
Figure 6.1: Illustration of unseeded cooling crystallization with varying stirring speeds

400 RPM to X RPM, when plateau temperature is achieved. As a control experiment to compensate the effect of mixing to growth rate, the stirring speed in Sequence B is set back to 400 RPM once the nucleation is observed. By comparison of the results at different stirring speeds, the importance of secondary nucleation to induction time and the CSD can be evaluated, which confirm or disapprove the hypothesis.

- Use a continuous process to determine secondary nucleation rate. In a continuous crystallizer, the CSD at steady state is [118]

$$\ln(n) = -\frac{L}{G\tau} + \ln(n_0) \tag{6.1}$$

and

$$n_0 = B_2/G \tag{6.2}$$

in which $\tau = V/Q$ is the residence time, n_0 is the number density of crystals at size 0. If n and τ are known for the continuous crystallizer, linear fitting of $\ln n$ against L estimates G and n_0. B_2 can be calculated by Gn_0. The values of B_2 and G can be compared with the kinetic models to verify the parameters obtained in Chapter 5.

113

6.2.3 Potential use of the two-step cooling strategy

Another interesting aspect revealed in this thesis is the two-step cooling strategy for unseeded processes. This operation can be viewed as an internal seeding policy, in which the seed population is internally created on the temperature plateau. As shown in Chapter 5, the CSD was controlled by the supersaturation plateau, and the secondary nucleation was effectively suppressed at $S_{\text{plat}} = 1.4$. Such results indicate the potential of the two-step cooling policy in the optimization of the final CSD. Unlike the traditional internal seeding policy, the control of T_{plat} avoids the excessive generation of nuclei, and thus, requires no dissolution steps.

The proposed two-step cooling strategy, which generates seed crystals internally, may avoid many drawbacks in external seeding operations. External seeding requires an optimal seed distribution to effectively suppress the secondary nucleation. The optimal seeding needs proper treatments, such as milling or washing, to achieve certain surface roughness and eliminate fines. Moreover, the storage and the addition of seeds increase the cost of operation as well.

The two-step cooling strategy was shown to be effective for crystallization of paracetamol in ethanol. The mean size of the crystals depends on the choice of plateau temperature. The utility of this strategy should be further verified against other strategies in more applications.

APPENDIX A

NOMENCLATURE

Abbreviations

ATR-FTIR	attenuated-total-reflectance-Fourier-transform infrared
API	active pharmaceutical ingredient
CE/SE	conservation element/solution element
CLD	chord length distribution
CLH	chord length histogram
CNT	classical nucleation theory
CSD	crystal size distribution
CSH	crystal size histogram
DSC	differential scanning calorimetry
FBRM	focused beam reflectance measurement
HPLC	high performance liquid chromatography
ODE	ordinary differential equation
PBE	population balance equation
PDE	partial differential equation
PC	principal component inversion
PVM	Particle vision and measurement
REG	regularized least square inversion
SSR	supersaturation ratio
TGA	thermal gravimetric analysis
XRD	X-ray diffraction

Greek letters

Ω	confidence region
Φ	fitting error
α	exponent of supersaturation in secondary nucleation
β	exponent of mass in secondary nucleation
γ	exponent in growth equation
ϵ	threshold of concentration for observation of nucleation
η	size-dependent growth factor
λ	tuning parameter in CLD-CSD transformation
μ_i	i^{th} moment of crystal population
ν	molecular volume
ρ_s	density of crystals
$\boldsymbol{\theta}$	parameter set
σ	crystal-solution interfacial tension
ω	weight of error term

English letters

A	transformation matrix, $\mathbf{n}$ to $\mathbf{q}$
B	nucleation rate
B_1	primary nucleation rate
B_2	secondary nucleation rate
B^j	sensitivity of simulation to parameters

D	death rate of crystals
E_a	activation energy of crystal growth
G	growth rate
L	crystal size
$\bar{L}_{1,0}$	number-averaged size of crystal
$\bar{L}_{4,3}$	volume-averaged size of crystal
N	number of experiments, sample points, measurements
N_1	number of nuclei generated by primary nucleation
N_2	number of nuclei generated by secondary nucleation
R	gas constant
S	supersaturation, c/c_s
T	temperature
U	transformation matrix, $\mathbf{x}$ to $\mathbf{b}$
$\tilde{U}$	$U^T U$
V	covariance matrix of measurements
V_θ	covariance matrix of parameters
$\mathbf{b}$	CLH vector
$\tilde{\mathbf{b}}$	$U^T \mathbf{b}$
$\mathbf{c}$	principal component (PC)
c	concentration
Δc	$c - c_s$
c_s	solubility
$\mathbf{e_k}$	natural basis on k^th dimension
e	fitting error
h	small perturbation for finite difference
k	Boltzmann constant
k_{b1}	coefficient of primary nucleation
k_{b2}	coefficient of secondary nucleation
k_g	coefficient of crystal growth
k_v	shape factor
l	geometric mean of a size range
m_s	mass of crystals
n	CSD number density
n_{vol}	CSD volume density
$\mathbf{n}$	CSD number density vector
q	CLD function (continuous)
q_p	Single crystal CLD
$\mathbf{q}$	CLD vector
r_c	critical radius of nuclei
s	chord length
Δs	bin width of CLH
t	time
t_{ind}	induction time
$\mathbf{v_i}$	internal coordinate
$\mathbf{x}$	CSH vector
x	size of crystals
Δx	discretization of size domain in CE/SE scheme
y	calculated volume density

Subscripts

0	initial condition
F	CSD estimates from FBRM
S	SSR

d	sample points
m	measured variables
$plat$	temperature plateau
r	experimental runs
sv	sieving
v	volume density

APPENDIX B

NUMERICAL SOLUTION OF POPULATION BALANCE EQUATION

B.1 Introduction

To describe the population balance (PBE) , the most simple partial differential equation is

$$\frac{\partial u}{\partial t} + \frac{\partial f(u)}{\partial x} = 0 \tag{B.1}$$

Usually, the function form of flux f is in the following form:

$$f(u) = au - \mu \partial u / \partial x \tag{B.2}$$

In crystallization modeling, it can often be assumed that there is only one crystal coordinate, which is the size (denoted as x) in the crystal size distribution u, and $f = Gu$, where G is the growth rate. Two examples to numerically solve the problem are finite difference method (FDM) and finite volume method (FVM), according to the treatments of x direction:

1) If the x-derivative $\partial u / \partial x$ is approximate by the difference between two neighboring points $(u_{i+1} - u_i)/(x_{i+1} - x_i)$ (or other more accurate finite difference schemes that involve more neighboring points), the PBE turns into an ODE system at grid points $u_i(t)$. However, the issue of the FDM is its poor approximation of $\partial u / \partial x$, which introduces a great deal of numerical instability for points with very steep gradients. For systems like PBE, since the CSD sometimes changes over several order of magnitudes, the FDM has to use very fine partition of x domain to maintain its accuracy. Too many grid points in x is a huge computational burden, and thus it is often not suitable to use the FDM to solve PBE.

2) If Equation (B.1) is integrated in a small size interval $[x_i, x_{i+1}]$, we have

$$\frac{\partial \int_{x_i}^{x_{i+1}} u\,dx}{\partial t} + \int_{x_i}^{x_{i+1}} \frac{\partial f}{\partial x}\,dx = 0 \tag{B.3}$$

Define $U_i = \int_{x_i}^{x_{i+1}} u\,dx$, which means U_i is the total number of crystals in the cell $[x_i, x_{i+1}]$. At the boundaries of cell i, the flux-in $F_{i-1/2} = f(u(x_{i-1/2}))$ and the flux-out is $F_i = f(u(x_{i+1/2}))$. An ODE system is obtained,

$$\frac{dU_i}{dt} = F_{i-1/2} - F_{i+1/2}, i = 1, 2, 3, ..., N - 1 \tag{B.4}$$

The structure of the partition is shown in Figure B.1, where equal spacing of cell is assumed. As we can see, the flux out of the left cell flows into the right one, so that the net flux of the entire system is $F_{in} - F_{out}$. Here, F_{in} and F_{out} should be calculated according to boundary conditions.
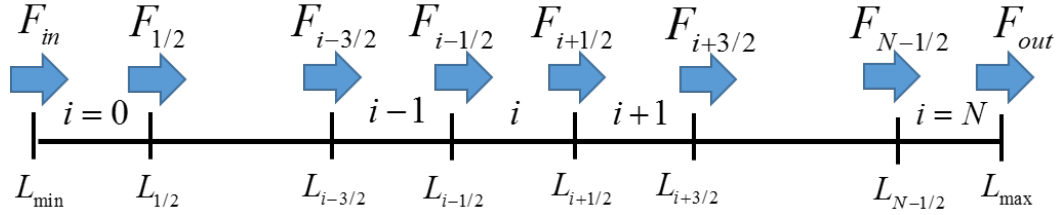
Figure B.1: Schematic of finite volume method

However, flux $F_{i+1/2}$ is not explicit from the FVM, because it depends on the $u_{i+1/2}$, instead of U_i or U_{i+1}. The average value in cell i is

$$\bar{u}_i = U_i/\Delta x \tag{B.5}$$

where $\Delta x = x_{i+1} - x_i$ is the width of the cell. Different ways of approximating the flux at cell boundary have been developed [69]. One approximation method is the upwind scheme

$$F_{i+1/2} = f(\bar{u}_i + \frac{1+\kappa}{4}(\bar{u}_{i+1} - \bar{u}_i) + \frac{1-\kappa}{4}(\bar{u}_i - \bar{u}_{i-1})), \kappa = [-1, 1] \tag{B.6}$$

119

This equation, assuming the flux flows towards positive-x direction, is a mixture of the central method ($\kappa = 1$) and one-side upwind method ($\kappa = -1$) [112, 132]. Rewrite Equation (B.6) in a universal upwind form

$$F_{i+1/2} = f(\bar{u}_i + \frac{1}{2}(\frac{1+\kappa}{2}r + \frac{1-\kappa}{2})(\bar{u}_i - \bar{u}_{i-1})) \tag{B.7}$$

$$r = \frac{\bar{u}_{i+1} - \bar{u}_i + \epsilon}{\bar{u}_i - \bar{u}_{i-1} + \epsilon} \tag{B.8}$$

where ϵ is a very small quantity (less than 10^{-10}) to avoid dividing-by-zero error. The ratio r of two consecutive increments in $\bar{u}_i$ is the parameter that determines the weight of $(\bar{u}_i - \bar{u}_{i-1})$. If there exists a shock wave or sharp changes in the solution, the value of r could result in wiggles near the shock front. Therefore, this weight is replaced by $\Phi(r)$ to limit the flux, and κ is set at $1/3$ [62]:

$$\Phi(r) = \max(0, \min(2r, \min(1/3 + 2r/3, 2))) \tag{B.9}$$

Then the weight is $1/3 + 2r/3$ when $0.5 < r < 2.5$, or $2r$ when $r < 0.5$, 2 when $r > 2.5$. This high-resolution method with flux limiter can give less numerical diffusion and suppress wiggles. More details can be found in Qamar *et al.* [112].

In this work, another method, which has been shown to be more accurate and efficient, was used as the reference solution. The method is called conservation-element/solution-element (CE/SE) scheme, invented by Chang [13] for aerodynamics. This method provides a fresh view in the discretization of the space-time domain and implementation of the PBE.

B.2   Methodology of CE/SE scheme

B.2.1   Conservation elements and solution elements

Suppose $\mathbf{h} = (f, u)$, Equation (B.1) becomes

$$\nabla \cdot \mathbf{h} = 0 \tag{B.10}$$

Therefore, for any small area dA, the integration of Equation (B.10) is zero

$$\iint\limits_A \nabla \cdot \mathbf{h}\, dA = 0 \tag{B.11}$$

where $dA = dx dt$ and $\nabla = (\partial/\partial x, \partial/\partial t)$. By the divergence theorem,

$$\oint\limits_C \mathbf{h} \cdot d\mathbf{C} = 0 \tag{B.12}$$

where $\mathbf{C}$ is a closed curve and $d\mathbf{C}$ is a line segment perpendicular to $d\mathbf{r} = (dx, dt)$. Hence, $d\mathbf{C} = (-dt, dx)$, which means

$$\oint\limits_C (f)dt + (-u)dx = 0 \tag{B.13}$$

Because $\mathbf{C}$ can be any arbitrary closed curve in the domain of (x, t) and the integral is zero, it means that there is a scalar function ϕ that has the derivative $\nabla \phi = (-u, f)$.

If the time-space domain is discretized in the following staggered pattern as shown in Figure B.2, then each unit in this domain is made of a $\Delta t/2 \times \Delta x/2$ square. The black dots, chosen in a staggered arrangement, are the points where the solution (u, f) is approximated, which are called solution points. The diamond area enclosed by dashed lines around point (j, n) is called solution element (j, n). Any arbitrary point within the solution element (j, n) can be calculated by the first order approximation,

$$u(x, t) = u(x_j, t^n) + u_x(x - x_j) + u_t(t - t^n) \tag{B.14}$$

$$f(x, t) = f(x_j, t^n) + f_x(x - x_j) + f_t(t - t^n) \tag{B.15}$$

From Equation (B.1) we also have

$$u_t = -f_x \tag{B.16}$$

Inside the solution element (j,n) centered at (x_j, t^n), we have $\nabla \phi = (-u, f)$. This ϕ can be second-order approximated by u, u_x, u_t, f, f_x and f_t.

$$\frac{\partial \phi}{\partial x} = -u \tag{B.17}$$
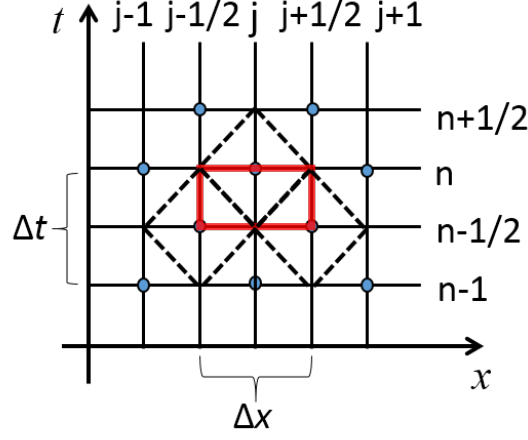
Figure B.2: Scheme of conservation elements (red rectangle) and solution elements (dashed diamond)

$$\frac{\partial \phi}{\partial t} = f \tag{B.18}$$

$$\frac{\partial^2 \phi}{\partial t^2} = f_t \tag{B.19}$$

$$\frac{\partial^2 \phi}{\partial x^2} = -u_x \tag{B.20}$$

$$\frac{\partial^2 \phi}{\partial x \partial t} = f_x \tag{B.21}$$

Then

$$\phi = f(t - t^n) - u(x - x_j) + (\frac{1}{2})f_t(t - t^n)^2 - (\frac{1}{2})u_x(x - x_j)^2 + f_x(x - x_j)(t - t^n) + constant \tag{B.22}$$

The other part of the method is the conservation elements, which enforce conservation law on neighboring solution elements. As shown in Figure B.2, solution elements, $(j - 1/2, n - 1/2)$, $(j + 1/2, n - 1/2)$, and (j, n), are adjacent. The conservation element is the red rectangle, which can be considered as three segments from three solution elements, as shown in Figure B.3. The integral along the conservation element is zero according to Equation (B.13), and, as the equation indicates, this line integration can be separated into three parts: $\phi_1 - \phi_2$, $\phi_3 - \phi_4$, and $\phi_5 - \phi_6$. In Equation (B.22), if we substitute ϕ with u, f, f_t, and f_x, the point at the next time
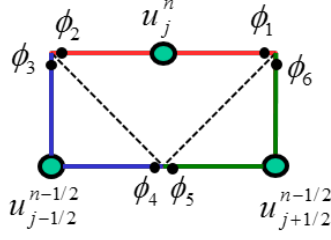
Figure B.3: Application of conservation law to neighboring solution elements

level can be written as

$$u_j^n = \frac{1}{2}\left(u_{j-1/2}^{n-1/2} + u_{j+1/2}^{n-1/2} + s_{j-1/2}^{n-1/2} - s_{j-1/2}^{n-1/2}\right) \tag{B.23}$$

where

$$s_j^n = \frac{\Delta x}{4}(u_x)_j^n + \frac{\Delta t}{\Delta x}f_j^n + \frac{(\Delta t)^2}{4\Delta x}(f_t)_j^n \tag{B.24}$$

If $(u_x)_j^n$, f_j^n, and $(f_t)_j^n$ can be explicitly determined by u_j^n, iteration can be started from the very first row and progress to the end of the time domain by marching this scheme on the temporal domain. The stability condition is given as the Courant-Friedrichs-Lewy (CFL) number $\nu^2 < 1$, where $\nu = a\Delta t/\Delta x$.

Assuming u_j^n is known, f is a function of u, so f_j^n can be calculated. From Equations (B.23), (B.24), $f_t = f_u u_t$, $u_t = -f_x$, and $f_t = -f_u f_x$, u_x remains the only unknown variable and should be evaluated with all known information.

B.2.2 Approximation of u_x

As described in the last section, marching from the time level $n - 1/2$ to n gives u_j^n, but u_x must be approximated properly. This remains a critical problem for the stability and accuracy of CE/SE scheme. Taking Figure B.4 as an example, u and u_x at $(j - 1/2, n - 1/2)$ and $(j + 1/2, n - 1/2)$ are assumed to be known, and thus u_t at these points are also known by the relationship $u_t = -f_x = -f_u u_x$.

One intuitive method is the central-difference approximation,

$$(u_x^c)_j^n = ((u')_{j+1/2}^n - (u')_{j-1/2}^n)/\Delta x \tag{B.25}$$
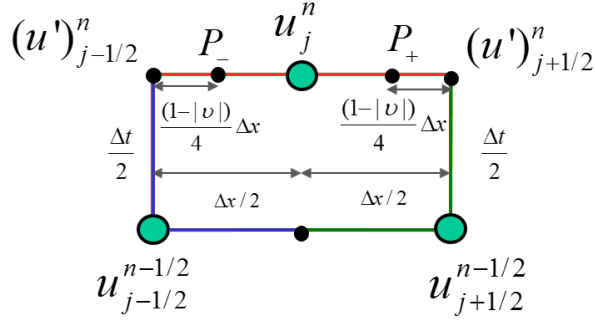
Figure B.4: Illustration for calculating u_x

in which $(u')^n_{j\pm1/2} = u^{n-1/2}_{j\pm1/2} + (u_t)^{n-1/2}_{j\pm1/2}\Delta t/2$, and c indicates the central difference. The values at the two ends of the SE (j, n) are estimated by SEs at the previous time level, without using any information about (j, n). However, if there is a discontinuity within the SE (j, n), the central-difference approximation would smooth it, which results in a great deal of numerical dissipation.

One correction term that can be made is

$$(du_x)^n_j = \frac{1}{2}[(u_x)^{n-1/2}_{j+1/2} - (u_x)^{n-1/2}_{j-1/2}] - (u^{n-1/2}_{j+1/2} - u^{n-1/2}_{j-1/2})/\Delta x \tag{B.26}$$

, which estimates the difference between the central difference and the known value u_x at time level $n - 1/2$.

Another method is using a weighted average of finite-difference from each side in solution element (j, n). On the right side, $(u_{x+})^n_j = ((u')^n_{j+1/2} - u^n_j)/(\Delta x/2)$ and the left side is $(u_{x-})^n_j = (u^n_j - (u')^n_{j-1/2})/(\Delta x/2)$. The weight averaging function is

$$W_o(x_-, x_+; \alpha) = \frac{|x_+|^\alpha x_- + |x_-|^\alpha x_+}{|x_+|^\alpha + |x_-|^\alpha} \tag{B.27}$$

To avoid dividing by zero, in practice a small positive number such as 10^{-60} is added to the denominator.

Modify the central-difference approximation of u_x with the two correction terms,

$$(u_x)^n_j = (u^c_x)^n_j + (2\epsilon - 1)(du_x)^n_j + \beta(W_o((u_{x-})^n_j, (u_{x+})^n_j, ; \alpha) - (u^c_x)^n_j) \tag{B.28}$$

There are three parameters, ϵ, α, and β, in Equation (B.28). It is shown that with certain parameter combination, the scheme is able to suppress wiggles as well as to

reduce numerical dissipation. For example, $\epsilon = 0.5, \alpha = 1, \beta = 1$ results in decent CE/SE solutions if the absolute value of ν is not too small. If $\nu \to 0$, the parameters should be adapted to the local CFL number.

Another scheme, insensitive to CFL number and independent of additional parameters, was developed [14]. As shown in Figure B.4, two points P_+ and P_- are approximated by the information of $(j + 1/2, n - 1/2)$ and $(j - 1/2, n - 1/2)$, respectively.

$$u'(P_+) = u_{j+1/2}^{n-1/2} + \frac{\Delta t}{2}(u_t)_{j+1/2}^{n-1/2} - \frac{(1 - |\nu|)\Delta x}{4}(u_x)_{j+1/2}^{n-1/2} \tag{B.29}$$

$$u'(P_-) = u_{j-1/2}^{n-1/2} + \frac{\Delta t}{2}(u_t)_{j-1/2}^{n-1/2} + \frac{(1 - |\nu|)\Delta x}{4}(u_x)_{j-1/2}^{n-1/2} \tag{B.30}$$

Thus, u_x can be estimated from both sides.

$$(\hat{u}_{x+}^+)_j^n = \frac{\Delta x}{4}\left(\frac{u'(P_+) - u_j^n}{(1 + |\nu|)\Delta x/4}\right) \tag{B.31}$$

$$(\hat{u}_{x-}^+)_j^n = \frac{\Delta x}{4}\left(\frac{u_j^n - u'(P_-)}{(1 + |\nu|)\Delta x/4}\right) \tag{B.32}$$

Here, the $(\hat{u}_{x\pm}^+)_j^n$ is normalized by $\Delta x/4$. To proceed, let

$$(s_\pm)_j^n = \frac{|(\hat{u}_{x\pm}^+)_j^n|}{\min(|(\hat{u}_{x+}^+)_j^n|, |(\hat{u}_{x-}^+)_j^n|)} \tag{B.33}$$

This $(s_\pm)_j^n$ are used to estimate $(u_x)_j^n$,

$$(u_x)_j^n = \frac{4}{\Delta x}\frac{[1 + f(|\nu|)(s_-)_j^n](\hat{u}_{x+}^+)_j^n + [1 + f(|\nu|)(s_+)_j^n](\hat{u}_{x-}^+)_j^n}{2 + f(|\nu|)[(s_-)_j^n + (s_+)_j^n]} \tag{B.34}$$

where,

$$f(|\nu|) = 0.5/|\nu| \tag{B.35}$$

B.3   Simulation of crystallization

The population balance takes the notation and form,

$$\frac{\partial n}{\partial t} + G\frac{\partial n}{\partial L} = 0 \tag{B.36}$$

125

where n is the number density of crystal population, $L \in [0\, L_{\max}]$ is the spatial dimension, G the is growth rate. Growth rate is assumed to be independent of L. Two factors are considered when simulating the PBE for crystallization: (i) how to associate the CE/SE scheme with the boundary conditions; (ii) how to descritize spatial and time domains so that the CFL number $\nu = G\Delta t/\Delta x$ is maintained less than one.

The boundary conditions for crystallization are

$$n(t, L = 0) = B/G \tag{B.37}$$

$$\frac{\partial n}{\partial L}(t, L = L_{\max}) = 0 \tag{B.38}$$

The CE/SE scheme shown in previous section is designed for an infinite spatial domain, not specified for any boundary conditions. However, the idea in CE/SE can still be applied.

Take the illustration of Figure B.5 as an example, the spatial domain is partitioned into eight units of $\Delta x/2$. To simplify the notation, the vertical lines are named $x_i, i = 1...9$ and horizontal rows are $t_j, j = 1, 2, 3$. Two types of rows differ by the numbers of their solution points. Odd-indexed rows have odd number of solution points, two of which are on the boundary. Even-indexed rows have even number of solution points, which entirely stay inside of spatial domain. Suppose n and n_L in Row 1 are known, it is simple to obtain n and n_L in Row 2 by applying CE/SE scheme.

When marching from Row 2 to Row 3, there are five n and n_L in Row 3 but only four n and n_L in Row 2, which leaves two degrees of freedom. According to CE/SE scheme, $n(x_i, t_3), \forall i = 3, 5, 7$, can be computed by marching forward from Row 2. Boundary conditions Equation (B.37) suggests $n(x_1, t_3) = B(t_3)/G(t_3)$ and Equation (B.38) suggests $n_L(x_9, t_3) = 0$. Two half conservation elements at the boundary are outlined by the red squares in Figure B.5, to which similar conservation method is applied as in CE/SE scheme.
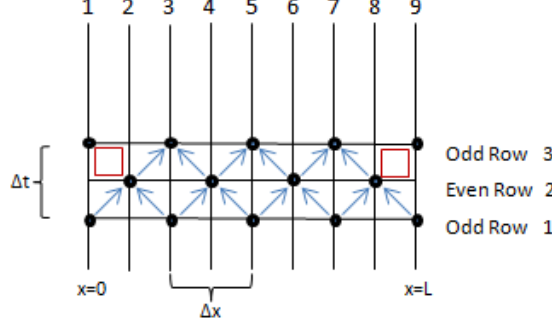
Figure B.5: March scheme of CE/SE method

Using the potential function shown in Equation (B.22), line integration along those two half conservation elements leads to the following equations,

$$n_L(x_1, t_3) = \frac{\frac{4}{\Delta x} [n(x_1, t_3)(\nu(t_3) - 1) + n(x_2, t_2)(\nu^2(t_2) - 1)] + n_L(x_2, t_2)}{1 - \nu^2(t_3)} \tag{B.39}$$

$$n(x_9, t_3) = \frac{(1 + \nu(t_2))n(x_8, t_2) + \frac{(1 - \nu^2(t_2))\Delta x}{4} n_L(x_8, t_2)}{1 + \nu(t_3)} \tag{B.40}$$

It can be seen in Equations (B.37) and (B.38) that, $n_L(x_1, t_3)$ and $n(x_9, t_3)$ require the information on the same time level ($\nu(t3)$), which makes the problem an implicit method. The CFL number is determined by G, which depends on the supersaturation and the mass of crystals at time t_3. However, the crystals near 0 μm may only take negligible mass. If $L_{\max}$ is sufficiently large, number density of crystals at $L_{\max}$ is nearly zero. Therefore, ν can be well approximated, even if the mass at two boundary points are ignored. When marching from an even-indexed row to next odd-indexed row, it is reasonable to calculate the interior points and find out B, G, and ν first, and then apply boundary conditions (Equations B.39 and B.40) to obtain full solutions on the odd-indexed row.

Another aspect is to maintain the stability condition $\nu = \dfrac{G\Delta t}{\Delta x} < 1$. In the practice of modeling crystallization, Δx is fixed throughout the simulation, and the growth rate G varies at difference stages of the process. When the supersaturation is high, G is large so that a Δt should be relatively small. When the solution is

only slightly supersaturated, such as at the end of the cooling process, G is small. Large Δt can be selected to reduce number of marching in the temporal direction. Therefore, at each time step, a new Δt is calculated to meet the CFL condition.

Using Figure B.5 as an example again. Suppose that the program marches to time level t_1 and the solution points at t_1 are known. G can be calculated from the mass balance and kinetic equations. A threshold ν_{th} is set less than 1 and Δt is calculated by

$$\Delta t = \nu_{th}\Delta x/G \tag{B.41}$$

The new Δt is calculated when marching is performed twice. As developed in the algorithm, the known initial condition starts at Row 0 with even number of solution points. This type of rows are called "even rows", since they are indexed with even numbers and have an even number of solution points, similar to t_2 level in Figure B.5. Even rows are defined not to include boundary points. A very small Δt is determined by CFL condition and time is marched forward by $\Delta t/2$ in order to solve for Row 1, with the help of boundary conditions. Row 1 has an odd number of solution points, one point more than Row 0. This type of rows are called "odd rows", in comparison with "even rows". With the solution on Row 1, same $\Delta t/2$ is used when solving for Row 2. Up to now the marching has been performed twice and a new Δt is used for solving for Row 3. The flow chart is shown in Figure B.6.
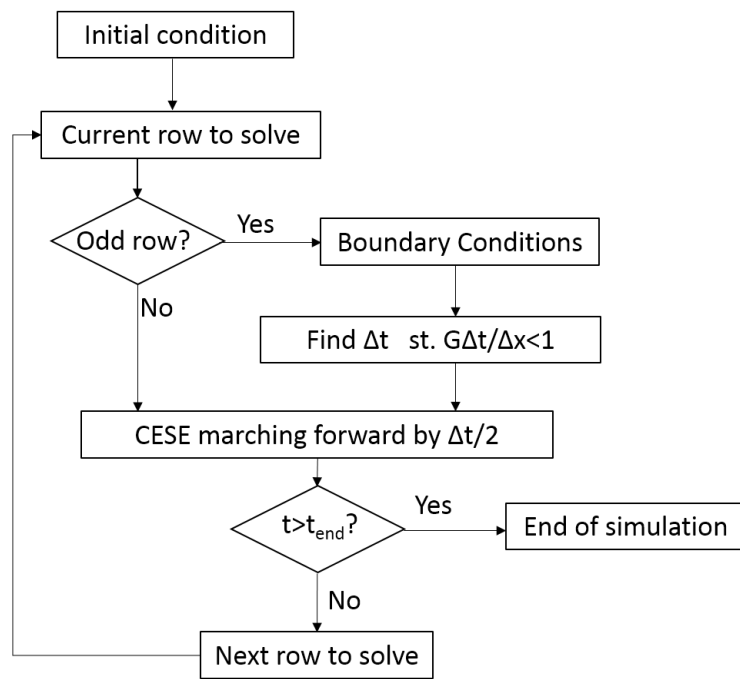
Figure B.6: Flow chart of the CE/SE algorithm

APPENDIX C

ADDITIONAL RESULTS OF PARAMETER ESTIMATION

C.1 Different combinations of training set for parameter estimation

According to the selection of FBRM results, three combinations of data can be provided to parameter estimation, as shown in Table C.1.

Table C.1: Combinations of training set

Runs	Combination 1			Combination 2			Combination 3		
	SSR	Sieving	*In situ* CSD	SSR	Sieving	*In situ* CSD	SSR	Sieving	*In situ* CSD
1	✓	✓	✓	✓	✓		✓	✓	
2	✓	✓	✓	✓	✓	✓	✓	✓	
3	✓	✓		✓	✓		✓	✓	

The differences between the combinations are the selections of *in situ* CSD estimates. Different parameters values were estimated from the combinations.

As we can see from Table C.2 to C.4, the estimated values are close except

Table C.2: Estimated kinetic parameters from Combination 1

k_{b1} No./s/kg solvent	σ mJ/m^2	k_{b2} No./s/kg solvent	α	β	k_g (m/s)(g/g)$^\gamma$	E_a kJ/mol	γ
53.9	4.61	7.44×10^4	1.92	0.71	40.5	40.8	1.28
95% confidence interval obtained by 1% perturbation							
15.8–183	4.25–4.91	(6.64–8.34)×10^4	±0.08	±0.02	±1.4	±0.13	±0.01

Table C.3: Estimated kinetic parameters from Combination 2

k_{b1} No./s/kg solvent	σ mJ/m^2	k_{b2} No./s/kg solvent	α	β	k_g (m/s)(g/g)$^\gamma$	E_a kJ/mol	γ
0.175	4.06	1.04×10^5	2.15	0.730	43.1	41.0	1.24
95% confidence interval obtained by 1% perturbation							
0.03–0.91	3.64–4.41	(0.92–1.18)×10^5	±0.11	±0.02	±1.6	±0.2	±0.02

Table C.4: Estimated kinetic parameters from Combination 3

k_{b1} No./s/kg solvent	σ mJ/m²	k_{b2} No./s/kg solvent	α	β	k_g (m/s)(g/g)$^\gamma$	E_a kJ/mol	γ
0.192	4.25	1.00×10^5	2.08	0.713	45.5	41.3	1.24
95% confidence interval obtained by 1% perturbation							
10^{-9}–10^7	3.59–4.76	$(0.74$–$1.36)\times10^5$	±0.21	±0.05	±1.7	±0.2	±0.03

the coefficient of primary nucleation. Another observation is that the widths of the confidence intervals are reduced if more *in situ* CSD estimates are used.

The optimization is a high-dimension nonlinear problem, dependent on eight parameters. To show the relation of between parameters, certain pairs of parameters were selected, varied, and plotted as variables versus objective value, including k_{b1} and k_{b2}, k_{b2} and k_g, k_g and γ, α and β. The objective functions using Combination 2 and Combination 3 are compared. When the values in the parameter pair are being changed, other parameters are constant as estimated in Table C.6 to C.4.

As shown in Table C.5, Combinations 4 and 5 have no sieving data. These combinations both lead to wrong parameters in Table C.7 and C.8.

Table C.5: Another combinations of training set

Runs	Combination 4			Combination 5		
	SSR	Sieving	*In situ* CSD	SSR	Sieving	*In situ* CSD
1	✓		✓	✓		
2	✓		✓	✓		
3	✓			✓		

Figure C.1 shows the advantage of using *in situ* CSD estimates and explains

Table C.6: Estimated kinetic parameters from Combination 1

k_{b1} No./s/kg solvent	σ mJ/m²	k_{b2} No./s/kg solvent	α	β	k_g (m/s)(g/g)$^\gamma$	E_a kJ/mol	γ
53.9	4.61	7.44×10^4	1.92	0.71	40.5	40.8	1.28
95% confidence interval obtained by 1% perturbation							
15.8–183	4.25–4.91	$(6.64$–$8.34)\times10^4$	±0.08	±0.02	±1.4	±0.13	±0.01

why the confidence interval of k_{b1} is wider than other parameters. In (a), two trenches

Table C.7: Estimated kinetic parameters from Combination 4

k_{b1} No./s/kg solvent	σ mJ/m^2	k_{b2} No./s/kg solvent	α	β	k_g (m/s)(g/g)$^\gamma$	E_a kJ/mol	γ
3.74×10^6	51.3	1.12×10^4	0.700	0.627	37.8	41.5	1.22

Table C.8: Estimated kinetic parameters from Combination 5

k_{b1} No./s/kg solvent	σ mJ/m^2	k_{b2} No./s/kg solvent	α	β	k_g (m/s)(g/g)$^\gamma$	E_a kJ/mol	γ
3.36	6.70	1.81×10^4	1.16	1.16	28.0	39.3	1.45

are shown so that it is very easy to obtain a local optimum when no *in situ* CSD estimates are unused. The trench at $\log k_{b1} = 7$ disappears in (b) due to the inclusion of *in situ* CSD estimates. However, the trench in (b) still covers $\log k_{b1} = 0$ 7, indicating the objective is insensitive to k_{b1}.
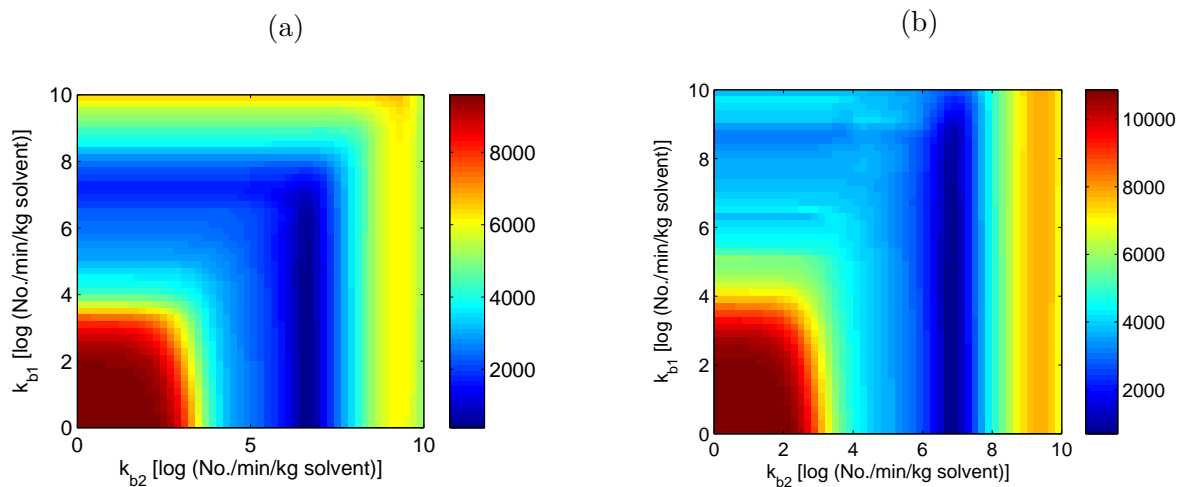
Figure C.1: The objective values against k_{b1} and k_{b2}: (a) using Combination 3; (b) using Combination 2

For the other pairs, there is no essential differences between using *in situ* CSD estimates and not using them.
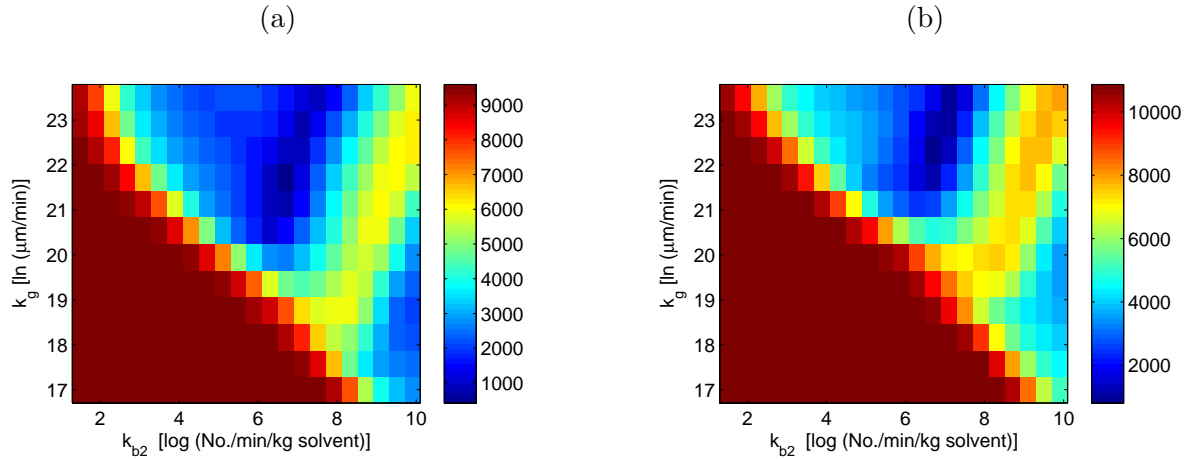
Figure C.2: The objective values against k_g and k_{b2}: (a) using Combination 3; (b) using Combination 2

(a)

(b)
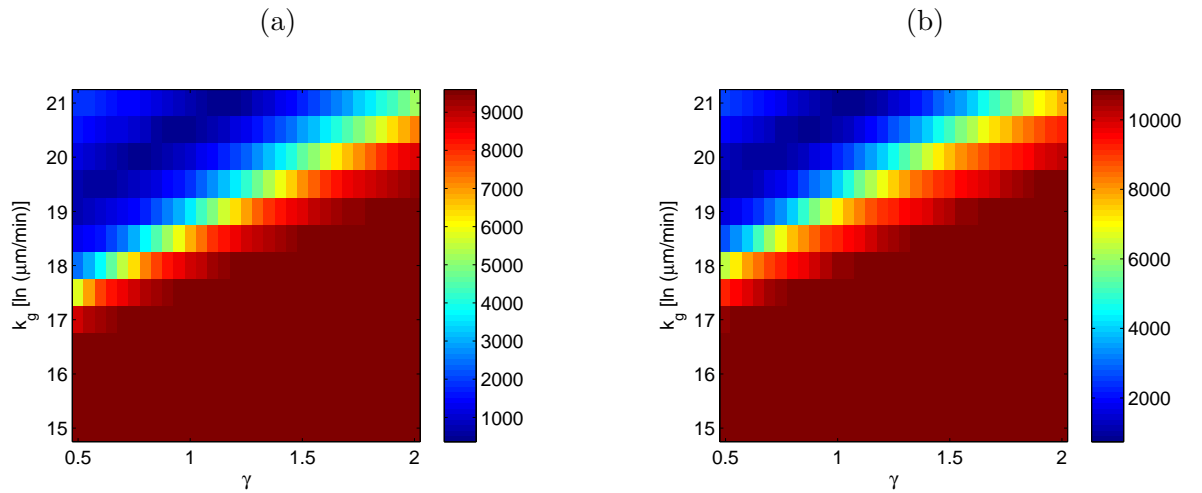
Figure C.3: The objective values against k_g and γ: (a) using Combination 3; (b) using Combination 2

C.2   Alternative kinetic models

In this section, multiple kinetic form are tried in order to show

133
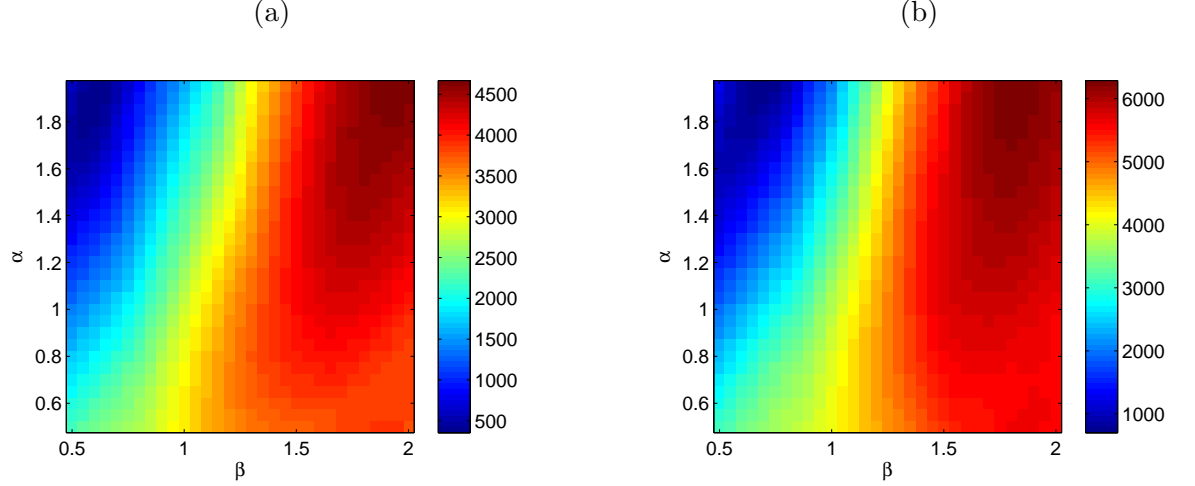
Figure C.4: The objective values against α and β: (a) using Combination 3; (b) using Combination 2

C.2.1 Another primary nucleation model

This estimation of interficial tension is generalized from experimental data of inorganic salt dissolved in water [88].

$$\sigma = 0.414kT(\rho_s N_A/M)(\ln \frac{c^S}{c^L}) \tag{C.1}$$

where c^S and c^L are the solute densities in solid and liquid phases. The unit of c^S is kg solute/m^3 solid, which is the density of paracetamol crystal, and the unit of c^L is kg solute/m^3 of solution. According to the unit of concentration used in this study, solute concentration is reported in g solute/kg solvent. Assuming solution density is equal to the density of ethanol, $\frac{c^S}{c^L} = 1000(\rho^S/\rho^{EtOH})/c = 1578/c$, where c is solute concentration in g solute/kg solvent as used in our model.

When $c = 370$ g solute/kg solvent at 44 °C, Equation C.1 estimates $\sigma = 7.6$ mJ/m^2, which is close to 4.06 mJ/m^2 in this study.

If this equation is plugged into Equation 5.5, the primary nucleation rate turns into

$$B_1 = k_{b1} \exp\left(-1.19k'\frac{(\ln 1578/c)^3}{(\ln S)^2}\right) \tag{C.2}$$

134

in which k,T,ν are all cancelled out, and k' is used to correct the error from the interficial tension approximation. As we can see, Equation C.2 suggests increase of concentration lead to higher primary nucleation rate.

C.2.2 Growth rate used in secondary nucleation

Secondary nucleation is induced by forces applied on the crystals as described in the mechanism. The number of nuclei created by the force may also rely on the feature of surface. If supersaturation is high, the crystal surface might be rough due to fast crystal growth and more nuclei are possible to detach from mother crystals. Therefore, the secondary nucleation rate could be rewritten as

$$B_2 = k_{b2}G^\alpha m_s^\beta \tag{C.3}$$

With Combination 1, the parameters estimated for the new secondary model are

Table C.9: Estimated kinetic parameters using Equation C.3 (Combination 1)

k_{b1} No./s/kg solvent	σ mJ/m^2	k_{b2} No./s/kg solvent	α	β	k_g (m/s)(g/g)$^\gamma$	E_a kJ/mol	γ
61.5	4.40	15.42	1.98	0.830	48.0	40.6	1.30

As we can see, these parameter is close to Table 5.2, except for k_b2, since the difference between $S-1$ and growth rate G. The fittings are acceptable.

C.2.3 Set $\alpha = \beta = 1$

Additional adjustment is constraining α and β both at 1, which is usually used as nominal exponent in secondary nucleation. Therefore, secondary nucleation model is

$$B_2 = k_{b2}Gm_s \tag{C.4}$$

The estimated parameters are shown in Table C.10. Although the SSR profiles are fitted well as shown in Figure C.6 (a) to (c), the calculated final CSDs of the three
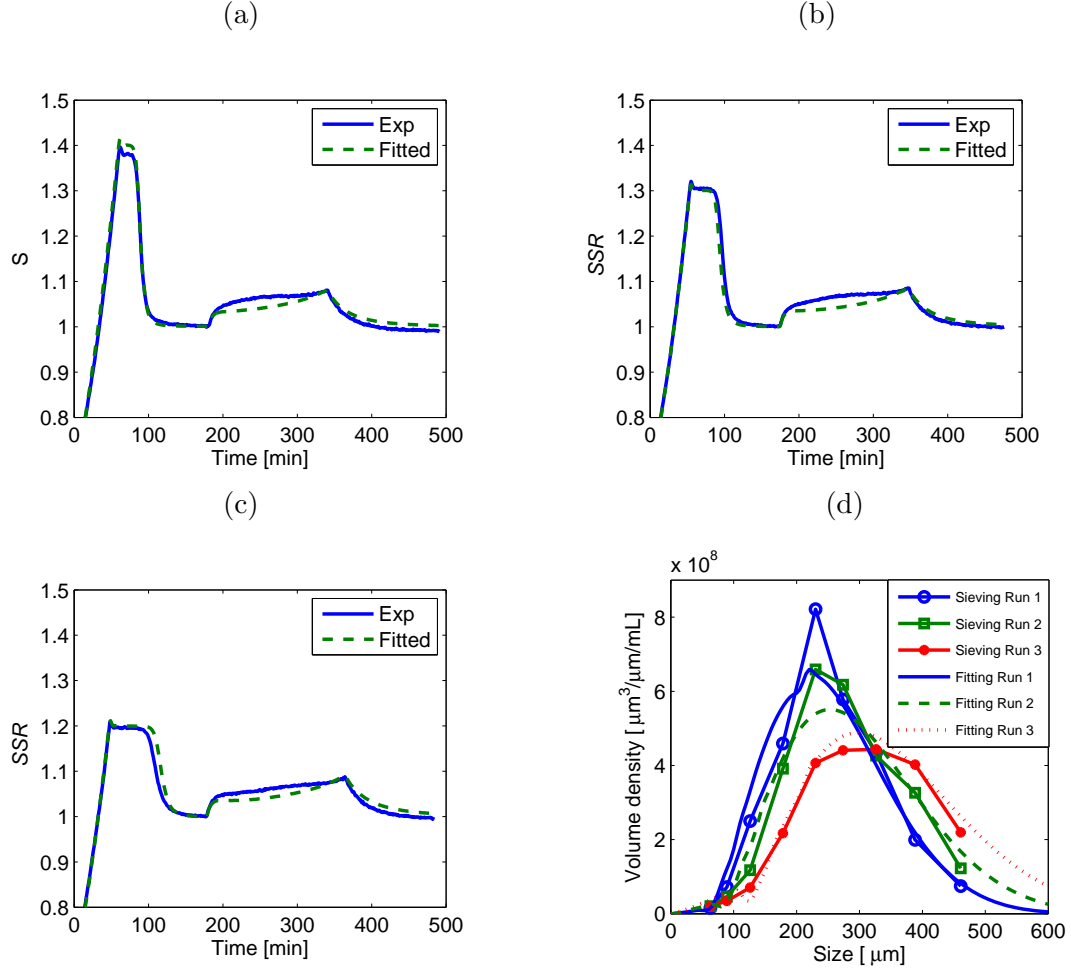
Figure C.5: Fitting with the secondary nucleation that has growth rate G (a) SSR of Run 1; (b) SSR of Run 1; (c) SSR of Run 1; (d) Final CSD

runs are completely overlap. Therefore, the fitting indicates that constraints of the exponent make the model unable to describe the CSD. It also implies that it is risky to estimate kinetic parameters only relying on concentration measurements, since there were multiple parameter combinations that can fit.

Table C.10: Estimated kinetic parameters using Equation C.4 (Combination 1)

k_{b1} No./s/kg solvent	σ mJ/m^2	k_{b2} No./s/kg solvent	α	β	k_g (m/s)(g/g)$^\gamma$	E_a kJ/mol	γ
7.89	2.85	118	1.00	1.00	67.1	40.9	1.35

However, the fitting to final CSDs has serious error.
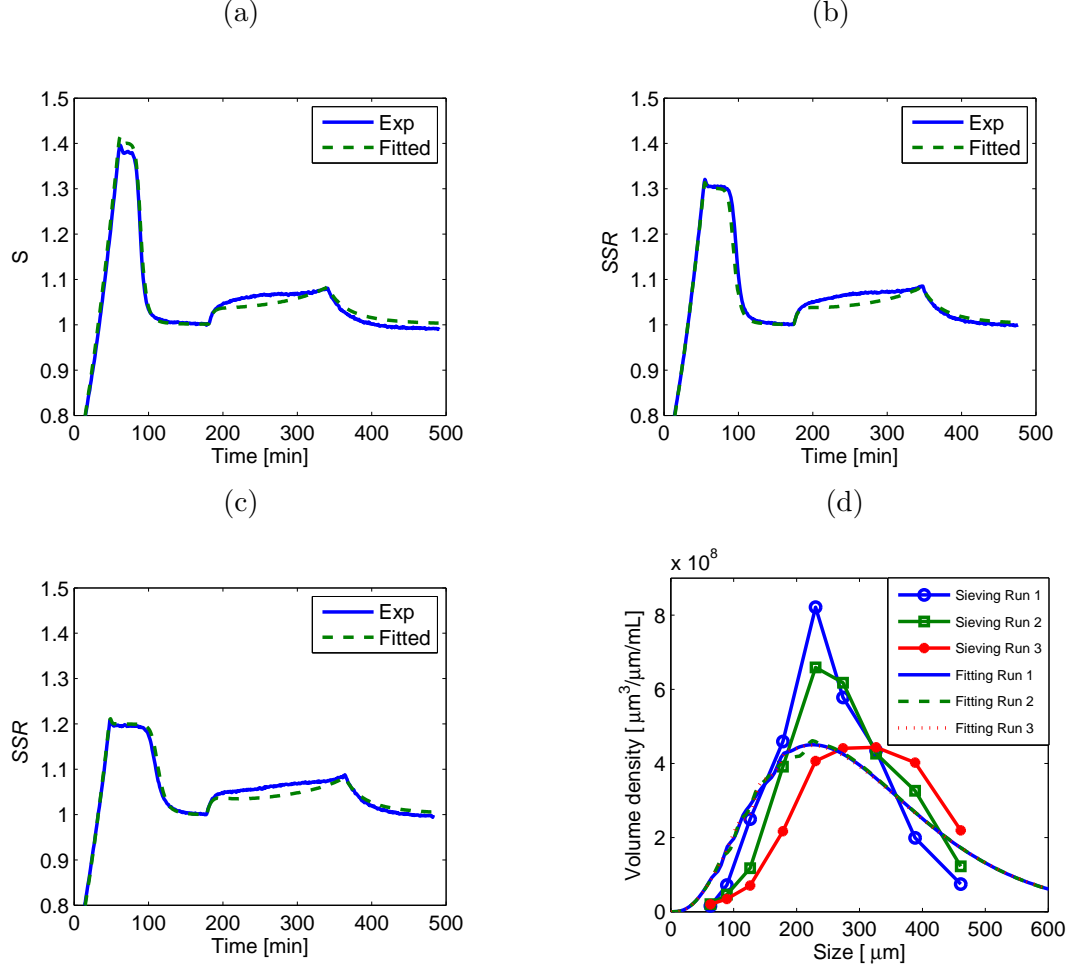
Figure C.6: Fitting with the secondary nucleation that has growth rate G and constraints for $\alpha = \beta = 1$ (a) SSR of Run 1; (b) SSR of Run 1; (c) SSR of Run 1; (d) Final CSD

C.2.4 Secondary nucleation neglected

Some empirical models were used for nucleation and growth in unseeded nucleation. The exponential equations are the most simple forms.

$$B_1 = k_{b1}(S-1)^{\alpha} \tag{C.5}$$

$$G = k_g \exp(-\frac{E_a}{RT})(S-1)^{\gamma} \tag{C.6}$$

We found that it is very difficult to fitting the SSR profiles with these two kinetic equations. As we can see from Figure C.7 which shows the best fit that we obtained, the model is unable to explain the induction time with the kinetic model. Nucleation

always occurred earlier than experimental results, and the predicted final CSDs have steep fronts on their right sides.

(a)

(b)

(c)

(d)
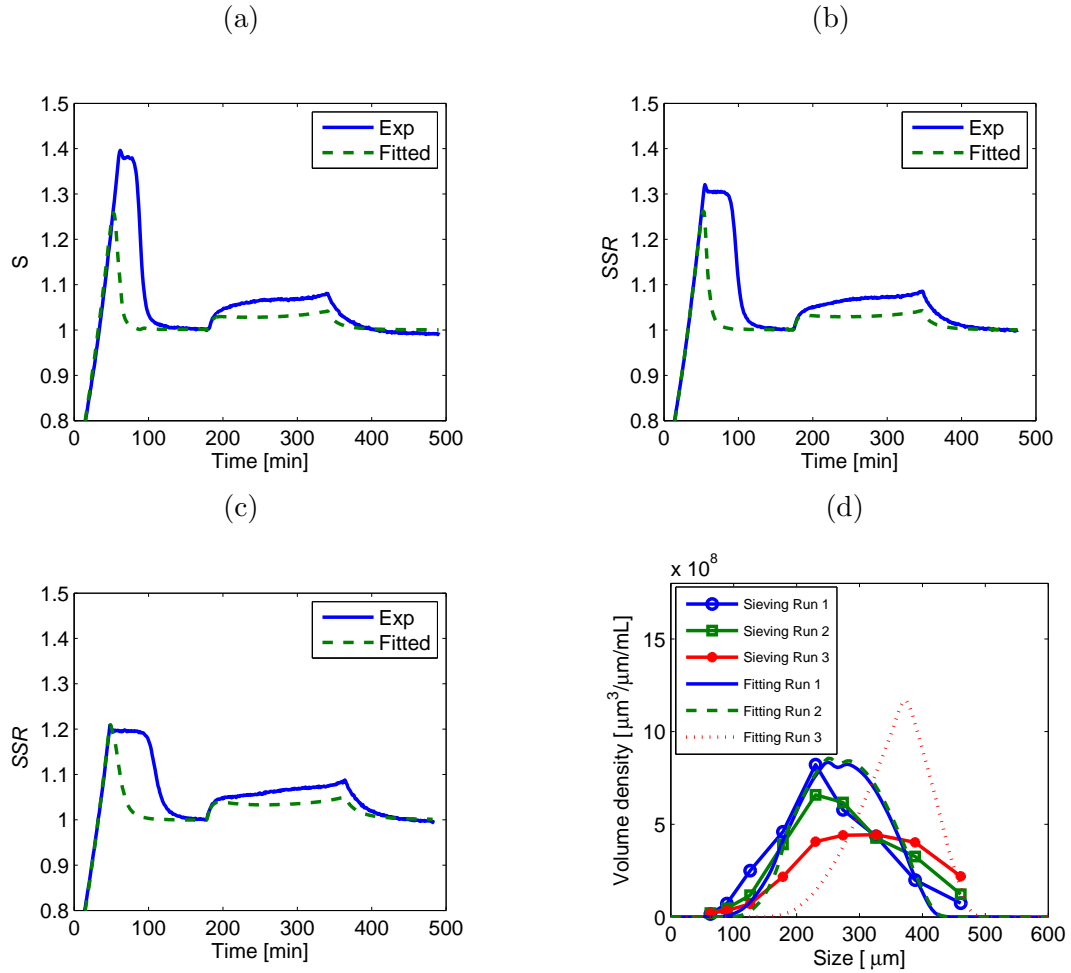
Figure C.7: Fitting with the secondary nucleation that has growth rate G and constraints for $\alpha = \beta = 1$ (a) SSR of Run 1; (b) SSR of Run 1; (c) SSR of Run 1; (d) Final CSD. Note that three fitting results completely overlap in (d).

Table C.11: Estimated kinetic parameters using Equation C.5 and C.6 (Combination 1)

k_{b1} No./s/kg solvent	σ mJ/m^2	k_{b2} No./s/kg solvent	α	β	k_g (m/s)(g/g)$^\gamma$	E_a kJ/mol	γ
3.66×10^7	–	–	4.84	–	7.55	39.6	1.36
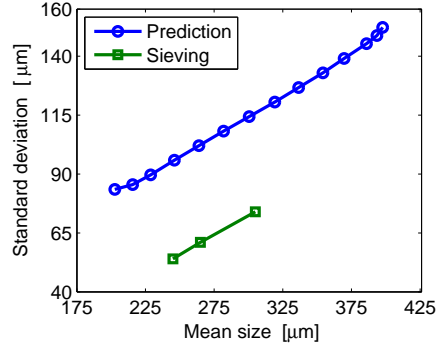
Figure C.8: Linear relationship between mean size and standard deviation

C.3 Linear relationship between mean size and standard variation

In addition to the study of the effect of T_{plat} on mean size, the relation between mean size $\mu_4/\_mu_3$ and the standard deviation is plotted in Figure C.8. As shown in Chapter 6, the mean size of the final product can be adjusted by using different T_{plat}. Figure C.8 shows a linear correlation between mean size and standard deviation, which indicates that a large mean size and a small standard deviation cannot be achieved at the same time.

REFERENCES

[1] Aamir, E., Nagy, Z. K., and Rielly, C. D., "Evaluation of the Effect of Seed Preparation Method on the Product Crystal Size Distribution for Batch Cooling Crystallization Processes," *Crystal Growth & Design*, vol. 10, no. 11, pp. 4728–4740, 2010.

[2] Aamir, E., Nagy, Z. K., Rielly, C. D., Kleinert, T., and Judat, B., "Combined Quadrature Method of Moments and Method of Characteristics Approach for Efficient Solution of Population Balance Models for Dynamic Modeling and Crystal Size Distribution Control of Crystallization Processes," *Industrial & Engineering Chemistry Research*, vol. 48, no. 18, pp. 8575–8584, 2009.

[3] Abu Bakar, M. R., Nagy, Z. K., and Rielly, C. D., "Investigation of the Effect of Temperature Cycling on Surface Features of Sulfathiazole Crystals during Seeded Batch Cooling Crystallization," *Crystal Growth & Design*, vol. 10, no. 9, pp. 3892–3900, 2010.

[4] Barrett, P. and Glennon, B., "In-line FBRM monitoring of particle size in dilute agitated suspensions," *Particle & Particle Systems Characterization*, vol. 16, no. 5, pp. 207–211, 1999.

[5] Barthe, S. and Rousseau, R. W., "Utilization of focused beam reflectance measurement in the control of crystal size distribution in a batch cooled crystallizer," *Chemical Engineering & Technology*, vol. 29, no. 2, pp. 206–211, 2006.

[6] Becker, R. and Döring, W., "Kinetische behandlung der keimbildung in übersättigten dämpfen," *Annalen der Physik*, vol. 416, no. 8, pp. 719–752, 1935.

[7] Bennett, M. and Rohani, S., "Solution of population balance equations with a new combined lax-wendroff/crank-nicholson method," *chemical engineering science*, vol. 56, no. 23, pp. 6623–6633, 2001.

[8] Beyer, T., Day, G. M., and Price, S. L., "The prediction, morphology, and mechanical properties of the polymorphs of paracetamol," *Journal of the American Chemical Society*, vol. 123, no. 21, pp. 5086–5094, 2001.

[9] Borissova, A., Khan, S., Mahmud, T., Roberts, K. J., Andrews, J., Dallin, P., Chen, Z.-P., and Morris, J., "In situ measurement of solution concentration during the batch cooling crystallization of l-glutamic acid using atr-ftir spectroscopy coupled with chemometrics," *Crystal Growth and Design*, vol. 9, no. 2, pp. 692–706, 2008.

[10] CALDERON DE ANDA, J., WANG, X., and ROBERTS, K., "Multi-scale segmentation image analysis for the in-process monitoring of particle shape with batch crystallisers," *Chemical Engineering Science*, vol. 60, no. 4, pp. 1053–1065, 2005.

[11] CANNING, T. and RANDOLPH, A., "Some aspects of crystallization theory: systems that violate mccabe's delta l law," *AIChE Journal*, vol. 13, no. 1, pp. 5–10, 1967.

[12] CHAI, X., HOU, Q., and VERRILL, C., "Rapid determination of total dissolved solids in black liquors by atr-uv/vis spectroscopy," *Journal of pulp and paper science*, vol. 31, no. 2, pp. 81–84, 2005.

[13] CHANG, S. C., "THE METHOD OF SPACE-TIME CONSERVATION ELEMENT AND SOLUTION ELEMENT - A NEW APPROACH FOR SOLVING THE NAVIER-STOKES AND EULER EQUATIONS," *Journal of Computational Physics*, vol. 119, no. 2, pp. 295–324, 1995.

[14] CHANG, S.-C., "Courant number insensitive ce/se schemes," *AIAA paper*, vol. 3890, p. 2002, 2002.

[15] CORNEL, J., LINDENBERG, C., and MAZZOTTI, M., "Quantitative application of in situ ATR-FTIR and Raman spectroscopy in crystallization processes," *Industrial & Engineering Chemistry Research*, vol. 47, no. 14, pp. 4870–4882, 2008.

[16] CZAPLA, F., KAIL, N., ONCUL, A., LORENZ, H., BRIESEN, H., and SEIDEL-MORGENSTERN, A., "Application of a recent FBRM-probe model to quantify preferential crystallization of DL-threonine," *Chemical Engineering Research & Design*, vol. 88, no. 11A, pp. 1494–1504, 2010.

[17] DI PROFIO, G., TUCCI, S., CURCIO, E., and DRIOLI, E., "Controlling polymorphism with membrane-based crystallizers: Application to form I and II of paracetamol," *Chemistry of Materials*, vol. 19, no. 10, pp. 2386–2388, 2007.

[18] DIAO, Y., MYERSON, A. S., HATTON, T. A., and TROUT, B. L., "Surface design for controlled crystallization: The role of surface chemistry and nanoscale pores in heterogeneous nucleation," *Langmuir*, vol. 27, no. 9, pp. 5324–5334, 2011.

[19] DIEMER, R. and OLSON, J., "A moment methodology for coagulation and breakage problems: Part 2moment models and distribution reconstruction," *Chemical Engineering Science*, vol. 57, no. 12, pp. 2211–2228, 2002.

[20] FENG, L. and BERGLUND, K. A., "Atr-ftir for determining optimal cooling curves for batch crystallization of succinic acid," *Crystal growth & design*, vol. 2, no. 5, pp. 449–452, 2002.

[21] FLORENCE, A. J. and JOHNSTON, A., "Applications of atr uv/vis spectroscopy in physical form characterisation of pharmaceuticals," *Spectrosc. Eur*, vol. 16, pp. 24–27, 2004.

[22] FRAWLEY, P. J., MITCHELL, N. A., O'CIARDHA, C. T., and HUTTON, K. W., "The effects of supersaturation, temperature, agitation and seed surface area on the secondary nucleation of paracetamol in ethanol solutions," *Chemical Engineering Science*, vol. 75, pp. 183–197, 2012.

[23] FUJIWARA, M., CHOW, P. S., MA, D. L., and BRAATZ, R. D., "Paracetamol crystallization using laser backscattering and ATR-FTIR spectroscopy: Metastability, agglomeration, and control," *Crystal Growth & Design*, vol. 2, no. 5, pp. 363–370, 2002.

[24] FUJIWARA, M., NAGY, Z. K., CHEW, J. W., and BRAATZ, R. D., "First-principles and direct design approaches for the control of pharmaceutical crystallization," *Journal of Process Control*, vol. 15, no. 5, pp. 493–504, 2005.

[25] GALKIN, O., CHEN, K., NAGEL, R. L., HIRSCH, R. E., and VEKILOV, P. G., "Liquid–liquid separation in solutions of normal and sickle cell hemoglobin," *Proceedings of the National Academy of Sciences*, vol. 99, no. 13, pp. 8479–8483, 2002.

[26] GELADI, P. and KOWALSKI, B. R., "Partial least-squares regression: a tutorial," *Analytica chimica acta*, vol. 185, pp. 1–17, 1986.

[27] GHERRAS, N. and FEVOTTE, G., "On the use of process analytical technologies and population balance equations for the estimation of crystallization kinetics. a case study," *AIChE Journal*, vol. 58, no. 9, pp. 2650–2664, 2012.

[28] GIBBS, J. W., "The collected works of j. willard gibbs: vol. 1: thermodynamics," tech. rep., Yale University Press, 1948.

[29] GIROLAMI, M. W. and ROUSSEAU, R. W., "Initial breeding in seeded batch crystallizers," *Industrial & Engineering Chemistry Process Design and Development*, vol. 25, no. 1, pp. 66–70, 1986.

[30] GOMEZ-MORALES, J., TORRENT-BURGUES, J., and RODRIGUEZ-CLEMENTE, R., "Nucleation of calcium carbonate at different initial ph conditions," *Journal of crystal growth*, vol. 169, no. 2, pp. 331–338, 1996.

[31] GRANBERG, R. A., BLOCH, D. G., and RASMUSON, A. C., "Crystallization of paracetamol in acetone-water mixtures," *Journal of Crystal Growth*, vol. 198, pp. 1287–1293, 1999.

[32] GRIFFIN, D. J., GROVER, M. A., KAWAJIRI, Y., and ROUSSEAU, R. W., "Robust multicomponent ir-to-concentration model regression," *Chemical Engineering Science*, vol. 116, pp. 77–90, 2014.

[33] GRIFFIN, D. J., KAWAJIRI, Y., GROVER, M. A., and ROUSSEAU, R. W., "Feedback control of multicomponent salt crystallization," *Crystal Growth & Design*, 2014.

[34] GRÖN, H., BORISSOVA, A., and ROBERTS, K. J., "In-process atr-ftir spectroscopy for closed-loop supersaturation control of a batch crystallizer producing monosodium glutamate crystals of defined size," *Industrial & engineering chemistry research*, vol. 42, no. 1, pp. 198–206, 2003.

[35] GROVER, M. A., BARTHE, S. C., and ROUSSEAU, R. W., "Principal Component Analysis for Estimating Population Density from Chord-Length Density," *Aiche Journal*, vol. 55, no. 9, pp. 2260–2270, 2009.

[36] GRZESIAK, A. L., LANG, M., KIM, K., and MATZGER, A. J., "Comparison of the four anhydrous polymorphs of carbamazepine and the crystal structure of form i," *Journal of pharmaceutical sciences*, vol. 92, no. 11, pp. 2260–2271, 2003.

[37] GUO, Z., JONES, A., LI, N., and GERMANA, S., "High-speed observation of the effects of ultrasound on liquid mixing and agglomerated crystal breakage processes," *Powder technology*, vol. 171, no. 3, pp. 146–153, 2007.

[38] GUO, Z., ZHANG, M., LI, H., WANG, J., and KOUGOULOS, E., "Effect of ultrasound on anti-solvent crystallization process," *Journal of Crystal Growth*, vol. 273, no. 3, pp. 555–563, 2005.

[39] HA, J.-M., WOLF, J. H., HILLMYER, M. A., and WARD, M. D., "Polymorph selectivity under nanoscopic confinement," *Journal of the American Chemical Society*, vol. 126, no. 11, pp. 3382–3383, 2004.

[40] HAHNENKAMP, I., GRAUBNER, G., and GMEHLING, J., "Measurement and prediction of solubilities of active pharmaceutical ingredients," *International Journal of Pharmaceutics*, vol. 388, no. 1-2, pp. 73–81, 2010.

[41] HAO, H., SU, W., BARRETT, M., CARON, V., HEALY, A.-M., and GLENNON, B., "A calibration-free application of raman spectroscopy to the monitoring of mannitol crystallization and its polymorphic transformation," *Organic Process Research & Development*, vol. 14, no. 5, pp. 1209–1214, 2010.

[42] HEATH, A. R., FAWELL, P. D., BAHRI, P. A., and SWIFT, J. D., "Estimating average particle size by focused beam reflectance measurement (FBRM)," *Particle & Particle Systems Characterization*, vol. 19, no. 2, pp. 84–95, 2002.

[43] HERMANTO, M. W., BRAATZ, R. D., and CHIU, M. S., "High-Order Simulation of Polymorphic Crystallization Using Weighted Essentially Nonoscillatory Methods," *Aiche Journal*, vol. 55, no. 1, pp. 122–131, 2009.

[44] HERMANTO, M. W., CHOW, P. S., and TAN, R. B. H., "Implementation of Focused Beam Reflectance Measurement (FBRM) in Antisolvent Crystallization to Achieve Consistent Product Quality," *Crystal Growth & Design*, vol. 10, no. 8, pp. 3668–3674, 2010.

[45] HERMANTO, M. W., KEE, N. C., TAN, R. B. H., CHIU, M. S., and BRAATZ, R. D., "Robust Bayesian Estimation of Kinetics for the Polymorphic Transformation of L-Glutamic Acid Crystals," *Aiche Journal*, vol. 54, no. 12, pp. 3248–3259, 2008.

[46] HOU, J., WU, S., LI, R., DONG, W., and GONG, J., "The induction time, interfacial energy and growth mechanism of maltitol in batch cooling crystallization," *Crystal Research and Technology*, vol. 47, no. 8, pp. 888–895, 2012.

[47] HOUNSLOW, M. and REYNOLDS, G., "Product engineering for crystal size distribution," *AIChE journal*, vol. 52, no. 7, pp. 2507–2517, 2006.

[48] HU, Q., ROHANI, S., and JUTAN, A., "Modelling and optimization of seeded batch crystallizers," *Computers & chemical engineering*, vol. 29, no. 4, pp. 911–918, 2005.

[49] HUKKANEN, E. J. and BRAATZ, R. D., "Measurement of particle size distribution in suspension polymerization using in situ laser backscattering," *Sensors and Actuators B-Chemical*, vol. 96, no. 1-2, pp. 451–459, 2003.

[50] ISO, B., "13320: 2009," *Particle size analysis-laser diffraction methods*.

[51] JIANG, S. and TER HORST, J. H., "Crystal nucleation rates from probability distributions of induction times," *Crystal Growth & Design*, vol. 11, no. 1, pp. 256–261, 2010.

[52] JOHN, V., ANGELOV, I., ÖNCÜL, A., and THÉVENIN, D., "Techniques for the reconstruction of a distribution from a finite number of its moments," *Chemical Engineering Science*, vol. 62, no. 11, pp. 2890–2904, 2007.

[53] KADAM, S. S., KRAMER, H. J. M., and TER HORST, J. H., "Combination of a Single Primary Nucleation Event and Secondary Nucleation in Crystallization Processes," *Crystal Growth & Design*, vol. 11, pp. 1271–1277, Apr. 2011.

[54] KADAM, S. S., KULKARNI, S. A., COLOMA RIBERA, R., STANKIEWICZ, A. I., TER HORST, J. H., and KRAMER, H. J., "A new view on the metastable zone width during cooling crystallization," *Chemical Engineering Science*, vol. 72, pp. 10–19, Apr. 2012.

[55] KAIL, N., BRIESEN, H., and MARQUARDT, W., "Advanced geometrical modeling of focused beam reflectance measurements (FBRM)," *Particle & Particle Systems Characterization*, vol. 24, no. 3, pp. 184–192, 2007.

[56] KAIL, N., BRIESEN, H., and MARQUARDT, W., "Analysis of FBRM measurements by means of a 3D optical model," *Powder Technology*, vol. 185, no. 3, pp. 211–222, 2008.

[57] KAIL, N., MARQUARDT, W., and BRIESEN, H., "Process Analysis by Means of Focused Beam Reflectance Measurements," *Industrial & Engineering Chemistry Research*, vol. 48, no. 6, pp. 2936–2946, 2009.

[58] KASHCHIEV, D., VERDOES, D., and VAN ROSMALEN, G., "Induction time and metastability limit in new phase formation," *Journal of crystal growth*, vol. 110, no. 3, pp. 373–380, 1991.

[59] KASHCHIEV, D., VEKILOV, P. G., and KOLOMEISKY, A. B., "Kinetics of two-step nucleation of crystals," *The Journal of chemical physics*, vol. 122, no. 24, p. 244706, 2005.

[60] KEE, N. C., ARENDT, P. D., GOH, L. M., TAN, R. B., and BRAATZ, R. D., "Nucleation and growth kinetics estimation for l-phenylalanine hydrate and anhydrate crystallization," *CrystEngComm*, vol. 13, no. 4, pp. 1197–1209, 2011.

[61] KONDEPUDI, D. K., LAUDADIO, J., and ASAKURA, K., "Chiral symmetry breaking in stirred crystallization of 1, 1'-binaphthyl melt," *Journal of the American Chemical Society*, vol. 121, no. 7, pp. 1448–1451, 1999.

[62] KOREN, B., *A robust upwind discretization method for advection, diffusion and source terms.* Centrum voor Wiskunde en Informatica Amsterdam, 1993.

[63] KULKARNI, S. A., KADAM, S. S., MEEKES, H., STANKIEWICZ, A. I., and TER HORST, J. H., "Crystal Nucleation Kinetics from Induction Times and Metastable Zone Widths," *Crystal Growth & Design*, vol. 13, pp. 2435–2440, June 2013.

[64] KUMAR, S. and RAMKRISHNA, D., "On the solution of population balance equations by discretization .1. A fixed pivot technique," *Chemical Engineering Science*, vol. 51, no. 8, pp. 1311–1332, 1996.

[65] KUMAR, S. and RAMKRISHNA, D., "On the solution of population balance equations by discretization .2. A moving pivot technique," *Chemical Engineering Science*, vol. 51, no. 8, pp. 1333–1342, 1996.

[66] KUMAR, S. and RAMKRISHNA, D., "On the solution of population balance equations by discretization - III. Nucleation, growth and aggregation of particles," *Chemical Engineering Science*, vol. 52, no. 24, pp. 4659–4679, 1997.

[67] LARSEN, P. A., RAWLINGS, J. B., and FERRIER, N. J., "An algorithm for analyzing noisy, in situ images of high-aspect-ratio crystals to monitor particle size distribution," *Chemical Engineering Science*, vol. 61, no. 16, pp. 5236–5248, 2006.

[68] Leba, H., Cameirao, A., Herri, J. M., Darbouret, M., Peytavy, J. L., and Glenat, P., "Chord length distributions measurements during crystallisation and agglomeration of gas hydrate in a water-in-oil emulsion: Simulation and experimentation (vol 65, pg 1185, 2010)," *Chemical Engineering Science*, vol. 65, no. 18, p. 5294, 2010.

[69] LeVeque, R. J., *Finite volume methods for hyperbolic problems*, vol. 31. Cambridge university press, 2002.

[70] Lewiner, F., Klein, J., Puel, F., and Fevotte, G., "On-line atr ftir measurement of supersaturation during solution crystallization processes. calibration and applications on three solute/solvent systems," *Chemical Engineering Science*, vol. 56, no. 6, pp. 2069–2084, 2001.

[71] Li, H., Grover, M. A., Kawajiri, Y., and Rousseau, R. W., "Development of an empirical method relating crystal size distributions and FBRM measurements," *Chemical Engineering Science*, vol. 89, pp. 142–151, 2013.

[72] Li, H., Kawajiri, Y., Grover, M. A., and Rousseau, R. W., "Application of an Empirical FBRM Model to Estimate Crystal Size Distributions in Batch Crystallization," *Crystal Growth & Design*, vol. 14, pp. 607–616, Jan. 2014.

[73] Li, M., Wilkinson, D., and Patchigolla, K., "Comparison of particle size distributions measured using different techniques," *Particulate Science and Technology*, vol. 23, no. 3, pp. 265–284, 2005.

[74] Li, M. Z. and Wilkinson, D., "Determination of non-spherical particle size distribution from chord length measurements. Part 1: Theoretical analysis," *Chemical Engineering Science*, vol. 60, no. 12, pp. 3251–3265, 2005.

[75] Lim, Y. I., Chang, S. C., and Jorgensen, S. B., "A novel partial differential algebraic equation (PDAE) solver: iterative space-time conservation element/solution element (CE/SE) method," *Computers & Chemical Engineering*, vol. 28, no. 8, pp. 1309–1324, 2004.

[76] Lim, Y. I. and Jorgensen, S. B., "A fast and accurate numerical method for solving simulated moving bed (SMB) chromatographic separation problems," *Chemical Engineering Science*, vol. 59, no. 10, pp. 1931–1947, 2004.

[77] Lindenberg, C., Krattli, M., Cornel, J., Mazzotti, M., and Brozio, J., "Design and Optimization of a Combined Cooling/Antisolvent Crystallization Process," *Crystal Growth & Design*, vol. 9, no. 2, pp. 1124–1136, 2009.

[78] Liotta, V. and Sabesan, V., "Monitoring and feedback control of supersaturation using atr-ftir to produce an active pharmaceutical ingredient of a desired crystal size," *Organic process research & development*, vol. 8, no. 3, pp. 488–494, 2004.

[79] LIU, J. and RASMUSON, Å. C., "Influence of agitation and fluid shear on primary nucleation in solution," *Crystal Growth & Design*, vol. 13, no. 10, pp. 4385–4394, 2013.

[80] LONG, D. A. and LONG, D., *Raman spectroscopy*, vol. 206. McGraw-Hill New York, 1977.

[81] LUQUE DE CASTRO, M. and PRIEGO-CAPOTE, F., "Ultrasound-assisted crystallization (sonocrystallization)," *Ultrasonics sonochemistry*, vol. 14, no. 6, pp. 717–724, 2007.

[82] LYCZKO, N., ESPITALIER, F., LOUISNARD, O., and SCHWARTZENTRUBER, J., "Effect of ultrasound on the induction time and the metastable zone widths of potassium sulphate," *Chemical Engineering Journal*, vol. 86, no. 3, pp. 233–241, 2002.

[83] MAHAJAN, A. J. and KIRWAN, D. J., "Nucleation and growth kinetics of biochemicals measured at high supersaturations," *Journal of crystal growth*, vol. 144, no. 3, pp. 281–290, 1994.

[84] MANGOLD, M., "Use of a Kalman filter to reconstruct particle size distributions from FBRM measurements," *Chemical Engineering Science*, vol. 70, pp. 99–108, 2012.

[85] MARCHISIO, D. L., SOOS, M., SEFCIK, J., and MORBIDELLI, M., "Role of turbulent shear rate distribution in aggregation and breakage processes," *AIChE journal*, vol. 52, no. 1, pp. 158–173, 2006.

[86] MARCHISIO, D. L., VIGIL, R. D., and FOX, R. O., "Quadrature method of moments for aggregation–breakage processes," *Journal of colloid and interface science*, vol. 258, no. 2, pp. 322–334, 2003.

[87] MCGRAW, R., "Description of aerosol dynamics by the quadrature method of moments," *Aerosol Science and Technology*, vol. 27, no. 2, pp. 255–265, 1997.

[88] MERSMANN, A., "Calculation of interfacial-tensions," *Journal of Crystal Growth*, vol. 102, no. 4, pp. 841–847, 1990.

[89] MESBAH, A., KRAMER, H. J. M., HUESMAN, A. E. M., and VAN DEN HOF, P. M. J., "A control oriented study on the numerical solution of the population balance equation for crystallization processes," *Chemical Engineering Science*, vol. 64, no. 20, pp. 4262–4277, 2009.

[90] MILLER, S. M. and RAWLINGS, J. B., "Model identification and control strategies for batch cooling crystallizers," *Aiche Journal*, vol. 40, no. 8, pp. 1312–1327, 1994.

[91] MITCHELL, N. A., FRAWLEY, P. J., and O'CIARDHA, C. T., "Nucleation kinetics of paracetamol-ethanol solutions from induction time experiments using Lasentec FBRM (R)," *Journal of Crystal Growth*, vol. 321, no. 1, pp. 91–99, 2011.

[92] MITCHELL, N. A., O'CIARDHA, C. T., and FRAWLEY, P. J., "Estimation of the growth kinetics for the cooling crystallisation of paracetamol and ethanol solutions," *Journal of Crystal Growth*, vol. 328, no. 1, pp. 39–49, 2011.

[93] MOJET, B. L., EBBESEN, S. D., and LEFFERTS, L., "Light at the interface: the potential of attenuated total reflection infrared spectroscopy for understanding heterogeneous catalysis in water," *Chemical Society Reviews*, vol. 39, no. 12, pp. 4643–4655, 2010.

[94] MONNIER, O., FEVOTTE, G., HOFF, C., and KLEIN, J., "Model identification of batch cooling crystallizations through calorimetry and image analysis," *chemical engineering science*, vol. 52, no. 7, pp. 1125–1139, 1997.

[95] MOTZ, S., MITROVIC, A., and GILLES, E. D., "Comparison of numerical methods for the simulation of dispersed phase systems," *Chemical Engineering Science*, vol. 57, no. 20, pp. 4329–4344, 2002.

[96] MUHR, H., DAVID, R., VILLERMAUX, J., and JEZEQUEL, P., "Crystallization and precipitation engineering-vi. solving population balance in the case of the precipitation of silver bromide crystals with high primary nucleation rates by using the first order upwind differentiation," *Chemical Engineering Science*, vol. 51, no. 2, pp. 309–319, 1996.

[97] MULLIN, J. W., *Crystallization*. Butterworth-Heinemann, 2001.

[98] MULLIN, J. and NỲVLT, J., "Programmed cooling of batch crystallizers," *Chemical Engineering Science*, vol. 26, no. 3, pp. 369–377, 1971.

[99] NAGY, Z. K. and BRAATZ, R. D., "Open-loop and closed-loop robust optimal control of batch processes using distributional and worst-case analysis," *Journal of Process Control*, vol. 14, no. 4, pp. 411–422, 2004.

[100] NAGY, Z. K., FUJIWARA, M., WOO, X. Y., and BRAATZ, R. D., "Determination of the kinetic parameters for the crystallization of paracetamol from water using metastable zone width experiments," *Industrial & Engineering Chemistry Research*, vol. 47, no. 4, pp. 1245–1252, 2008.

[101] NELDER, J. A. and MEAD, R., "A simplex method for function minimization," *The computer journal*, vol. 7, no. 4, pp. 308–313, 1965.

[102] NERE, N. K., RAMKRISHNA, D., PARKER, B. E., BELL, W. V., and MOHAN, P., "Transformation of the chord-length distributions to size distributions for nonspherical particles with orientation bias," *Industrial & Engineering Chemistry Research*, vol. 46, no. 10, pp. 3041–3047, 2007.

[103] NIELSEN, M. H., ALONI, S., and DE YOREO, J. J., "In situ tem imaging of caco3 nucleation reveals coexistence of direct and indirect pathways," *Science*, vol. 345, no. 6201, pp. 1158–1162, 2014.

[104] OCHSENBEIN, D. R., SCHORSCH, S., VETTER, T., MAZZOTTI, M., and MORARI, M., "Growth rate estimation of β l-glutamic acid from online measurements of multidimensional particle size distributions and concentration," *Industrial & Engineering Chemistry Research*, 2013.

[105] O'CIARDHA, C. T., HUTTON, K. W., MITCHELL, N. A., and FRAWLEY, P. J., "Simultaneous Parameter Estimation and Optimization of a Seeded Antisolvent Crystallization," *Crystal Growth & Design*, vol. 12, no. 11, pp. 5247–5261, 2012.

[106] ONO, T., KRAMER, H., TER HORST, J., and JANSENS, P., "Process modeling of the polymorphic transformation of l-glutamic acid," *Crystal growth & design*, vol. 4, no. 6, pp. 1161–1167, 2004.

[107] O'SULLIVAN, B. and GLENNON, B., "Application of in situ fbrm and atr-ftir to the monitoring of the polymorphic transformation of d-mannitol," *Organic process research & development*, vol. 9, no. 6, pp. 884–889, 2005.

[108] PATAKI, H., CSONTOS, I., NAGY, Z. K., VAJNA, B., MOLNAR, M., KATONA, L., and MAROSI, G., "Implementation of raman signal feedback to perform controlled crystallization of carvedilol," *Organic Process Research & Development*, vol. 17, no. 3, pp. 493–499, 2012.

[109] PAXTON, T. E., SAMBANIS, A., and ROUSSEAU, R. W., "Influence of vessel surfaces on the nucleation of protein crystals," *Langmuir*, vol. 17, no. 10, pp. 3076–3079, 2001.

[110] POUND, G. M. and MER, V. K. L., "Kinetics of crystalline nucleus formation in supercooled liquid tin1, 2," *Journal of the American Chemical Society*, vol. 74, no. 9, pp. 2323–2332, 1952.

[111] QAMAR, S., ASHFAQ, A., WARNECKE, G., ANGELOV, I., ELSNER, M. P., and SEIDEL-MORGENSTERN, A., "Adaptive high-resolution schemes for multidimensional population balances in crystallization processes," *Computers & Chemical Engineering*, vol. 31, no. 10, pp. 1296–1311, 2007.

[112] QAMAR, S., ELSNER, M. P., ANGELOV, I. A., WARNECKE, G., and SEIDEL-MORGENSTERN, A., "A comparative study of high resolution schemes for solving population balances in crystallization," *Computers & Chemical Engineering*, vol. 30, no. 6-7, pp. 1119–1131, 2006.

[113] QAMAR, S., WARNECKE, G., and ELSNER, M. P., "On the solution of population balances for nucleation, growth, aggregation and breakage processes," *Chemical Engineering Science*, vol. 64, no. 9, pp. 2088–2095, 2009.

[114] QAMAR, S., WARNECKE, G., ELSNER, M. P., and SEIDEL-MORGENSTERN, A., "A laplace transformation based technique for reconstructing crystal size distributions regarding size independent growth," *Chemical Engineering Science*, vol. 63, no. 8, pp. 2233–2240, 2008.

[115] QU, H., ALATALO, H., HATAKKA, H., KOHONEN, J., LOUHI-KULTANEN, M., REINIKAINEN, S.-P., and KALLAS, J., "Raman and atr ftir spectroscopy in reactive crystallization: Simultaneous monitoring of solute concentration and polymorphic state of the crystals," *Journal of Crystal Growth*, vol. 311, no. 13, pp. 3466–3475, 2009.

[116] QU, H., LOUHI-KULTANEN, M., and KALLAS, J., "In-line image analysis on the effects of additives in batch cooling crystallization," *Journal of Crystal Growth*, vol. 289, no. 1, pp. 286–294, 2006.

[117] RANDOLPH, A. D. and LARSON, M. A., *Theory of Particulate Processes: Analysis and Techniques of Continuous Crystallization*. London: Academic Press, 1988.

[118] RANDOLPH LARSON, MAURICE A, A. D., *Theory of particulate processes : analysis and techniques of continuous crystallization*. San Diego : Academic Press, 1988, 2nd ed. ed., 1988.

[119] RAWLINGS, J. B., MILLER, S. M., and WITKOWSKI, W. R., "MODEL IDENTIFICATION AND CONTROL OF SOLUTION CRYSTALLIZATION PROCESSES - A REVIEW," *Industrial & Engineering Chemistry Research*, vol. 32, no. 7, pp. 1275–1296, 1993.

[120] RUF, A., WORLITSCHEK, J., and MAZZOTTI, M., "Modeling and experimental analysis of PSD measurements through FBRM," *Particle & Particle Systems Characterization*, vol. 17, no. 4, pp. 167–179, 2000.

[121] SALEEMI, A. N., RIELLY, C. D., and NAGY, Z. K., "Comparative investigation of supersaturation and automated direct nucleation control of crystal size distributions using atr-uv/vis spectroscopy and fbrm," *Crystal Growth & Design*, vol. 12, no. 4, pp. 1792–1807, 2012.

[122] SCHÖLL, J., VICUM, L., MÜLLER, M., and MAZZOTTI, M., "Precipitation of l-glutamic acid: Determination of nucleation kinetics," *Chemical engineering & technology*, vol. 29, no. 2, pp. 257–264, 2006.

[123] SEAR, R. P., "Estimation of the scaling of the nucleation time with volume when the nucleation rate does not exist," *Crystal Growth & Design*, vol. 13, no. 3, pp. 1329–1333, 2013.

[124] SIMMONS, M. J. H., LANGSTON, P. A., and BURBIDGE, A. S., "Particle and droplet size analysis from chord distributions," *Powder Technology*, vol. 102, no. 1, pp. 75–83, 1999.

[125] SÖHNEL, O. and MULLIN, J. W., "Interpretation of crystallization induction periods," *Journal of colloid and interface science*, vol. 123, no. 1, pp. 43–50, 1988.

[126] SOHNEL, O., MULLIN, J. W., and JONES, A. G., "Crystallization and agglomeration kinetics in the batch precipitation of strontium molybdate," *Industrial & engineering chemistry research*, vol. 27, no. 9, pp. 1721–1728, 1988.

[127] SWEBY, P. K., "High resolution schemes using flux limiters for hyperbolic conservation laws," *SIAM journal on numerical analysis*, vol. 21, no. 5, pp. 995–1011, 1984.

[128] TADAYON, A., ROHANI, S., and BENNETT, M. K., "Estimation of nucleation and growth kinetics of ammonium sulfate from transients of a cooling batch seeded crystallizer," *Industrial & engineering chemistry research*, vol. 41, no. 24, pp. 6181–6193, 2002.

[129] TADAYYON, A. and ROHANI, S., "Determination of particle size distribution by Par-Tec (R) 100: Modeling and experimental results," *Particle & Particle Systems Characterization*, vol. 15, no. 3, pp. 127–135, 1998.

[130] TOGKALIDOU, T., FUJIWARA, M., PATEL, S., and BRAATZ, R. D., "Solute concentration prediction using chemometrics and ATR-FTIR spectroscopy," *Journal of Crystal Growth*, vol. 231, no. 4, pp. 534–543, 2001.

[131] TOGKALIDOU, T., TUNG, H. H., SUN, Y., ANDREWS, A. T., and BRAATZ, R. D., "Parameter estimation and optimization of a loosely bound aggregating pharmaceutical crystallization using in situ infrared and laser backscattering measurements," *Industrial & Engineering Chemistry Research*, vol. 43, no. 19, pp. 6168–6181, 2004.

[132] VAN LEER, B., "Upwind-difference methods for aerodynamic problems governed by the euler equations," in *Large-scale computations in fluid mechanics*, vol. 1, pp. 327–336, 1985.

[133] VEKILOV, P. G., "Dense liquid precursor for the nucleation of ordered solid phases from solution," *Crystal growth & design*, vol. 4, no. 4, pp. 671–685, 2004.

[134] VERMA, R. and RAJAMANI, R., "Effect of milling environment on the breakage rates in dry and wet grinding," 1992.

[135] VOLMER, M., "Kinetik der phasenbildung," 1939.

[136] WAN, J., MA, C. Y., and WANG, X. Z., "A method for analyzing on-line video images of crystallization at high-solid concentrations," *Particuology*, vol. 6, no. 1, pp. 9–15, 2008.

[137] WANG, F., WACHTER, J. A., ANTOSZ, F. J., and BERGLUND, K. A., "An investigation of solvent-mediated polymorphic transformation of progesterone using in situ raman spectroscopy," *Organic Process Research & Development*, vol. 4, no. 5, pp. 391–395, 2000.

[138] WESTIN, K.-J. and RASMUSON, Å. C., "Nucleation of calcium carbonate in presence of citric acid, dtpa, edta and pyromellitic acid," *Journal of colloid and interface science*, vol. 282, no. 2, pp. 370–379, 2005.

[139] WORLITSCHEK, J., HOCKER, T., and MAZZOTTI, M., "Restoration of PSD from chord length distribution data using the method of projections onto convex sets," *Particle & Particle Systems Characterization*, vol. 22, no. 2, pp. 81–98, 2005.

[140] WORLITSCHEK, J. and MAZZOTTI, M., "Model-based optimization of particle size distribution in batch-cooling crystallization of paracetamol," *Crystal Growth & Design*, vol. 4, no. 5, pp. 891–903, 2004.

[141] WORLITSCHEK, J., *Monitoring, modeling and optimization of batch cooling crystallization.* PhD thesis, Swiss Federal Institute of Technology Zurich, Switzerland, ETH Diss Nr. 15189, 2004.

[142] WULKOW, M., GERSTLAUER, A., and NIEKEN, U., "Modeling and simulation of crystallization processes using parsival," *Chemical Engineering Science*, vol. 56, no. 7, pp. 2575–2588, 2001.

[143] WULKOW, M., "The simulation of molecular weight distributions in polyreaction kinetics by discrete galerkin methods," *Macromolecular theory and simulations*, vol. 5, no. 3, pp. 393–416, 1996.

[144] WYNN, E. J. W., "Relationship between particle-size and chord-length distributions in focused beam reflectance measurement: stability of direct inversion and weighting," *Powder Technology*, vol. 133, no. 1-3, pp. 125–133, 2003.

[145] YANG, H. and RASMUSON, Å. C., "Nucleation of butyl paraben in different solvents," *Crystal Growth & Design*, vol. 13, no. 10, pp. 4226–4238, 2013.

[146] YU, Z. Q., CHOW, P. S., and TAN, R. B. H., "Interpretation of focused beam reflectance measurement (FBRM) data via simulated crystallization," *Organic Process Research & Development*, vol. 12, no. 4, pp. 646–654, 2008.

[147] YUAN, C. and FOX, R. O., "Conditional quadrature method of moments for kinetic equations," *Journal of Computational Physics*, vol. 230, no. 22, pp. 8216–8246, 2011.

[148] ZHANG, G. P. and ROHANI, S., "On-line optimal control of a seeded batch cooling crystallizer," *Chemical Engineering Science*, vol. 58, no. 9, pp. 1887–1896, 2003.

[149] ZHOU, Y., SRINIVASAN, R., and LAKSHMINARAYANAN, S., "Critical evaluation of image processing approaches for real-time crystal size measurements," *Computers & Chemical Engineering*, vol. 33, no. 5, pp. 1022–1035, 2009.

[150] ZUMSTEIN, R. C. and ROUSSEAU, R. W., "Agglomeration of copper sulfate pentahydrate crystals within well-mixed crystallizers," *Chemical Engineering Science*, vol. 44, no. 10, pp. 2149–2155, 1989.